DEVELOPMENT OF A POST-FORM STRENGTH PREDICTION MODEL FOR A 6XXX ALUMINIUM ALLOY IN A NOVEL FORMING PROCESS

By

Qunli ZHANG

A thesis submitted to Imperial College London for the degree of Doctor of Philosophy

Department of Mechanical Engineering
South Kensington Campus
Imperial College London
London SW7 2AZ
U.K.

2019

Declaration of originality

This thesis hereby presented is based on research by the author at the Department of Mechanical Engineering of Imperial College London. I declare the work contained in this thesis is the result of my independent research under the supervision of Dr Liliang Wang. Not any part of the present work has been submitted for any other degree or qualification elsewhere.

Qunli ZHANG

May 2019

Copyright Declaration

Abstract

Accurate prediction of the post-form strength of structural components made from 6xxx series aluminium alloys has been a challenge, especially when the alloy undergoes complex thermo-mechanical processes such as the Fast light Alloys Stamping Technology (FAST). This process involves ultra-fast heating, high temperature plastic deformation, rapid quenching and is followed by multi-stage artificial ageing heat treatment.

The strength of the material evolves with the formation of second phase precipitates during the entire process. The widely accepted precipitation sequence is SSSS → clusters → β'' → β' → β. However, due to the complexity of deformations and thermal profile during the process, the classic theory is not applicable. Therefore, in this research, precipitation behaviour during ultra-fast heating, viscoplastic behaviour, effect of residual dislocations generated during high temperature deformation, quenching sensitivity and multi-stage artificial ageing response have been comprehensively studied. A set of experiments, including ultra-fast heating tests, uniaxial tensile tests, pre-straining uniaxial tensile tests, quenching tests, artificial ageing tests and TEM observations were conducted to provide a thorough understanding of the novel forming technology.

The underlying mechanisms for the FAST process were investigated through the in-depth analysis of experimental results.

- Under ultra-fast heating conditions, most of the precipitates are dissolved and the spherical pre-β'' precipitates are formed and finely dispersed in the aluminium matrix, which are beneficial to accelerate the subsequent precipitation process.
- The residual dislocations, generated during plastic deformation, strengthen the material and act as nucleation sites for precipitates. The peak strength is reduced owing to the uneven accumulation of precipitates around dislocations.
- The coarse β' and β precipitates induced due to the insufficient quenching are detrimental to precipitation response. These quench-induced precipitates consume both solute atoms and vacancies, which are unable to be reversely transferred to the preferred needle-shaped β'' precipitates.

Based on the scientific achievements, a mechanism-based unified post-form strength (PFS) prediction model was developed ab-initio to predict the strength evolution of the material during the entire complex FAST process with highly efficient computation. Constitutive equations were proposed to model the viscoplastic behaviour at elevated temperature. Important microstructural parameters, including dislocation density, volume fraction, radius of precipitates and solute concentration were correlated to predict the material strength. The particle size distribution (PSD) sub-model was further established to accurately interpret the detailed microstructural changes during the complex thermo-mechanical processes.

Furthermore, the model has been programmed into an advanced functional module 'Tailor' and implemented into a cloud based FEA platform. The predictive capability of the module was verified by conducting forming tests of a U-shaped component in a dedicated pilot production line. It was found that the 'Tailor' module was able to precisely predict the post-form strength in agreement with experiments, with a deviation of less than 7% compared to experimental results.

Acknowledgements

I would like to express my sincerest gratitude to my supervisor, Dr. Liliang Wang, for the continuous support along my Ph.D. journey, offering me invaluable advices and encouraging me to grow as a qualified researcher. He introduced me to metal forming and material modelling field and shared me with his prophetic vision into the future of this industry, which attracted me immediately and made me decide to devote myself to the Ph.D. research. His patience, motivation and immense knowledge guided me in all the time of research and I could not have imagined having a better supervisor during my Ph.D. study. I would like to thank Prof. Jianguo Lin, my co-supervisor, for providing support whenever I needed it.

I am incredibly grateful for the President's scholarship that was provided by the Department of Mechanical Engineering of Imperial College London, whom gave me the golden opportunity to do the wonderful project with the most talent people in the world.

I would especially like to thank Dr Jun Liu and Dr Denis J. Politis who provided unlimited support throughout my studies. Thank you for offering me insightful comments and encouragement to widen my research from various perspectives. I also thank all the members in our research group: Dr Omer El Fakir, Dr Haoxiang Gao, Dr Kang Ji, Dr Ailing Wang, Dr Yiran Hu, Xi Luan, Yang Zheng, Yuhao Sun, Xiaochuan Liu, Zhaoheng Cai, Mateusz Kopec, Saksham Dhawan and Xiao Yang. Without their support, my research would not have been achievable.

Finally but most importantly, I would like to acknowledge the people who mean the whole world to me, my family: my mother Qin Zhang, my father Chunning Zhang and my fiancée Lijia Zhang. I cannot imagine a life without their love and blessings.

Table of contents

List of figures

List of tables

List of publications

Journal articles:

Zhang, Q., Luan, X., Dhawan, S., Politis, D.J., Du, Q., Fu, M.W., Wang, K., Gharbi, M.M., Wang, L., 2019. Development of the post-form strength prediction model for a high-strength 6xxx aluminium alloy with pre-existing precipitates and residual dislocations. Int. J. Plast. 119, 230–248.

Zhang, Q., Ji, K., El Fakir, O., Liu, X., Wang, L., 2016. Determination of Processing Windows for the Hot Stamping of AA7075, Key Eng. Mater. 716, 402–412.

Yang, X., **Zhang, Q.,** Zheng, Y., Politis, D.J., Wang, L., Development of the interactive friction model for lubricant breakdown at elevated temperature utilising a SA-based optimisation scheme, Tribol. Int. Under review.

Wang, A., El Fakir, O., Liu, J., **Zhang, Q.,** Zheng, Y., Wang, L., 2019. Multi-objective finite element simulations of a sheet metal-forming process via a cloud-based platform. Int. J. Adv. Manuf. Technol. 100, 2753–2765.

Ji, K., Liu, X., El Fakir, O., Liu, J**., Zhang, Q.,** Wang, L., 2016. Determination of the Interfacial Heat Transfer Coefficient in the Hot Stamping of AA7075, Manuf. Rev. 3, 16–20.

Zhang, Q., Dhawan, S., Politis, D.J., Du, Q., Fu, M.W., Wang, L., Development of a unified modelling framework for Al-Mg-Si alloys undergoing an ultra-fast heating thermo-mechanical processing, Int. J. Plast. To be submitted.

Conference papers:

Zhang, Q., Dhawan, S., Luan, X., Du, Q., Liu, J., Wang, L., 2019. Investigation and Constitutive Modelling of High Strength 6xxx Series Aluminium Alloy: Precipitation Hardening Responses to FAST (Fast Light Alloys Stamping Technology) and Artificial Ageing. Mater. Sci. Forum. 941, 814–820.

Zhang, Q., Luan, X., Dhawan, S., Politis, D.J., Cai, Z., Wang, L., 2018. Investigating the quench sensitivity of high strength AA6082 aluminium alloy during the new FAST forming process. IOP Conf. Ser. Mater. Sci. Eng. 418, 12028.

Luan, X., **Zhang, Q.,** Fakir, O., Wang, L., Gharbi, M.M., 2016. Uni-Form : a pilot production line for hot/warm sheet metal forming integrated in a cloud based SMARTFORMING platform. Int. Conf. Adv. High Strength Steel Press Hardening 492–497.

El Fakir, O., Wang, A., **Zhang, Q.,** Liu, X., Liu, J., Wang, L., 2016. Multi-objective sheet metal forming simulations using a software agnostic platform, IOP Conf. Ser. Mater. Sci. Eng. 418, 12122.

Cai, Z., Batthyány, P., Dhawan, S., **Zhang, Q.,** Sun, Y., Luan, X., Wang, L., Gharbi, M.M., 2018. Study of Springback for High Strength Aluminium Alloys Under Hot Stamping. Int. Conf. Adv. High Strength Steel Press Hardening 117–121.

Gao, H., Politis, D.J., Luan, X., Ji, K., **Zhang, Q.,** Zheng, Y., Gharbi, M.M., Wang, L., 2017. Forming limit prediction for AA7075 alloys under hot stamping conditions, J. Phys. Conf. Ser. 896, 12089.

Patent:

Luan, X., Sun, Y., **Zhang, Q.,** El Fakir, O., Cai, Z., Wu, G., Wang, L., 2019, A unified production system for forming lightweight panel components. CN201910707785.9.

Dhawan, S., El Fakir, O., **Zhang, Q.,** Wang, A., Zheng, Y., Wu, G., Wang, L., 2019, An online database for hosting and executing numerical models. To be submitted.

Cai, Z., El Fakir, O., Sun, Y., **Zhang, Q.,** Dhawan, S., Luan, X., Wu, G., Wang, L., 2019, A data guided approach to manufacturing light-weight components. CN201910786108.0.

Nomenclature

English Variables

A	Solute concentration constant
A'	Energy barrier parameter
A_0	Temperature dependent material constant
A_{00}	Pre-exponential parameter of A_0
A_d	Dislocation hardening constant at room temperature
B	Dislocation hardening constant at elevated temperature
B_0	Pre-exponential parameter of B
B_1	Kinetic factor of dislocations for solute concentration
B_2	Kinetic factor of dislocations for mean precipitate radius
B_3	Kinetic factor of dislocations for nucleation rate
B_4	Kinetic factor of dislocations for diffusion
b	Burgers vector
C_0	Solute concentration at SSSS
C_1	Coarsening constant
C_2	Shearing strengthening constant
C_3	Bypassing strengthening constant
C_4	Solid solution strengthening constant
C_{ageing}	Static recovery constant
C_e	Equilibrium solute concentration
C_i	Initial solute concentration
C_{int}	Solute concentration in the precipitate/matrix interface
C_j	Concentration of a specific alloying element
C_p	Temperature dependent material constant
C_{p0}	Pre-exponential parameter of C_p
C_{pep}	Loss of concentration due to pre-existing precipitates
C_q	Loss of solute concentration during quenching
C_s	Maximum solute concentration
C_{sp}	Concentration of a specific element inside the precipitates

C_t	Transient solute concentration
$\dot{C}_t$	Transient solute concentration rate
C_{tp}	Transient solute concentration with dislocation effect
$\dot{C_{tp}}$	Transient solute concentration rate with dislocation effect
C_x	Solute concentration after first-stage ageing
D	Diffusion coefficient
D_0	Pre-exponential term of diffusion
D_{diff}	Diffusion coefficient for bulk diffusion
D_{dis}	Diffusion coefficient for dislocation core diffusion
E	Young's modulus
f_0	Pre-exponential factor of volume fraction
f_e	Equilibrium volume fraction of precipitates
f_{max}	Maximum volume fraction of precipitates
f_t	Transient volume fraction of precipitates
$\dot{f}_t$	Volume fraction rate of precipitation
f_x	Volume fraction of precipitates after first-stage ageing
G	Shear modulus
ΔG^*_{het}	Energy barrier for nucleation
j	Nucleation rate
j_0	Pre-exponential term of nucleation
j'_0	Temperature dependent nucleation constant
j'_{00}	Pre-exponential parameter of j'_0
K	Temperature dependent material constant
K_0	Pre-exponential parameter of K
k	Threshold stress
k_0	Pre-exponential parameter of k
k_1	Peak ageing time constant
k_j	Solid solution strengthening constant of a specific element
M	Taylor factor
N_i	Number of precipitates in a specific radius class
n_1	Temperature dependent material constant
n_{10}	Pre-exponential parameter of n_1

n_2	Material constant
R	Universal gas constant
r	Mean radius of precipitates
$\dot{r}$	Growth rate of precipitates
$\dot{r}_p$	Growth rate of precipitates with dislocation effect
r_0	Initial mean radius of precipitates
r_c	Critical radius
r_i	Mean radius of precipitates in a specific radius class
T	Temperature
T_s	Solvus temperature
t	Artificial ageing time
$t_{eq,c}$	Solute concentration equivalent time
$t_{eq,r}$	Radius equivalent time
t_p	Time to achieve peak strength
Q	Quenching factor
Q_0	Pre-exponential quenching factor
Q_A	Activation energy for volume diffusion of atoms
$Q_{A_{00}}$	Activation energy for A_0
Q_B	Activation energy for B
Q_{C_p}	Activation energy for C_p
Q_d	Activation energy of diffusion
Q_{diff}	Activation energy of bulk diffusion
Q_{dis}	Activation energy of dislocation core diffusion
Q_j	Activation energy for nucleation rate
Q_K	Activation energy for K
Q_k	Activation energy for k
Q_{n_1}	Activation energy for n_1
Q_q	Activation energy for diffusion controlled precipitation
Q_s	Solvus boundary enthalpy
V_m	Molar volume of the precipitates
v	Growth rate of the precipitates

Greek Variables

α	Material constant
γ	Precipitate-matrix interface energy
ε_p	Plastic strain
$\dot{\varepsilon_p}$	Plastic strain rate
ε_T	Total strain
ρ	Dislocation density
ρ_i	Initial dislocation density
ρ_m	Maximum dislocation density
$\overline{\rho}$	Normalised dislocation density
$\dot{\overline{\rho}}$	Normalised dislocation density rate
σ_{by}	Strength of bypassing precipitates
σ_{dis}	Dislocation hardening strength
σ_i	Intrinsic strength of aluminium matrix
σ_{ppt}	Strength of precipitates
σ_{sh}	Strength of shearable precipitates
σ_{ss}	Solid solution strength
σ_{total}	Flow stress
σ_y	Yield stress
τ	Solute decay constant

Chapter 1. Introduction

1.1 Background

With growing global concern of climate change caused by greenhouse gas emissions, governments around the world have achieved an important consensus and signed the Paris Agreement in 2016 to undertake bold actions in combating climate change and adapting to its effects (United Nations, 2016). Transportation is the largest source of greenhouse gas emissions, covering 27% in Europe, 29% in the US and 14% worldwide (Eurostat, 2019; Grelier, 2018; U.S. Energy Information Administration, 2017). Cars are responsible for around 12% of total CO_2 emissions in the EU. Therefore, a drive for tackling the issue of greenhouse gas emissions has led to strict legislations on the automotive industry, especially in Europe. The European commission set ambitious requirements for vehicle manufacturers to reduce the emissions to 130 g CO_2 per kilogram in 2015 and 95 g CO_2 per kilogram in 2021 (European commission, 2017). In addition, automotive manufacturers are required to pay a premium on any excess emissions when failing to meet these targets.

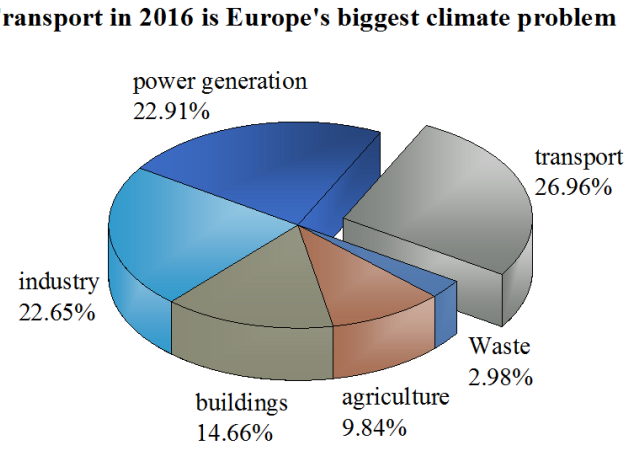

Figure 1.1: EU greenhouse gas emission per sector in 2016 (Grelier, 2018)

The automotive industry has utilised various strategies to tackle transport emissions:

(1). Reduction of vehicle weight;

(2). Optimisation of the powertrain system to improve fuel efficiency;

(3). Energy management and hybridisation;

(4). Development of an intelligent transport system to optimise the driver's decisions.

It is found that mass reduction of vehicles via replacing steel with lightweight alloys is an effective approach to realize the emission target. The light-weighting approach is used to reduce the vehicle weight significantly, thus improve the fuel efficiency as well as reduce the CO_2 emissions. According to the research, 10% weight reduction of the vehicle body would lead to 8% reduction in CO_2 emissions (Lutsey, 2010). The use of aluminium alloys, magnesium alloys, plastics and polymer composites has been growing during the past decades, with the material distribution of a 'super' light car shown in Figure 1.2. Age-hardenable 6xxx series aluminium alloys are promising candidates for panel structural components due to their excellent mechanical properties: high strength-to-weight ratio, high stiffness-to-density ratio, good corrosion resistance, recyclability and remarkable formability at elevated temperatures. If steel components in a car body structure are replaced by aluminium alloys, the weight of a vehicle can be saved by over 40%, and correspondingly, the CO_2 emissions would be reduced by more than 30%.

Figure 1.2: 'Super' light car material distribution (WorldAutoSteel, n.d.)

Although aluminium alloys have great potential for producing high strength components with reduced weight, they have limited formability at room temperature and require special processing techniques. Recently, a novel hot stamping technology – Fast light Alloys Stamping Technology (FAST) has been developed to manufacture high-strength panel components from sheet 6xxx series aluminium alloys, which involves ultra-fast heating, hot stamping and in-die quenching, followed by multi-stage paint bake cycles (L. Wang et al., 2017). This forming process eliminates solution heat treatment completely prior to stamping and reduces the required artificial ageing time to achieve a unique and unprecedented enhancement in the production rate as well as retain the full mechanical strength after multi-stage paint bake cycles.

The production process of aluminium alloys is highly customised and each formed part has a set of unique processing windows to be determined accordingly. Different shaped components, components assembled in different locations and similar components produced by different manufacturers may have completely different processing windows. It is extremely time-consuming and costly to conduct a large amount of trial and error tests to optimise processing windows for each component. Hence, modelling the post-form strength of heat-treatable AA6xxx series alloys is important, as it enables the optimisation of manufacturing processes and the wide application of these high strength aluminium alloys. However, it is fairly challenging to establish such models due to multi-parameter dependency on chemical composition, plastic deformation, quenching and post-form heat treatment.

The main focus of this research is the development of a unified post-form strength prediction (PFS) model for 6xxx aluminium alloys in a novel forming process, taking into account interdependencies between microstructural parameters, such as dislocation density, solute concentration, volume fraction and mean radius of precipitates. The unified PFS model, consisting of five sub-models: flow-stress, quenching, artificial ageing, multi-stage artificial ageing and particle size distribution (PSD), has been developed to predict the strength and microstructure evolutions during the whole process. The model was then programmed as an advanced functional module 'Tailor' and implemented into a cloud based FEA platform, to predict optimal post-form heat treatment parameters required to manufacture a component with the desired strength (Wang et al., 2019).

1.2 Aims and objectives

The aim of the present work was to obtain a comprehensive scientific understanding to the nature of the new forming technology (FAST) for 6xxx series Al-Mg-Si alloys. Precipitation behaviour during ultra-fast heating, viscoplastic behaviour at various strain rates, effect of residual dislocations generated by plastic deformation, quenching sensitivity as well as precipitation response during multi-stage post-form heat treatment were systematically investigated. An innovative post-form strength prediction (PFS) model was developed accordingly to precisely characterise the strength and microstructure evolutions during complex thermo-mechanical processes and efficiently optimise the processing parameters to

exploit age hardening to the maximum potential. The following objectives were completed to achieve this aim:

1. Conduct research on the state-of-art lightweight forming technologies for sheet aluminium alloys. Review precipitation hardening theories and existing models for the prediction of precipitation response of Al-Mg-Si alloys.

2. Achieve a thorough scientific understanding of the new forming technology (FAST). Perform a series of experiments to comprehensively investigate the viscoplastic behaviour, quenching sensitivity and precipitation response of 6xxx aluminium alloys.

3. Develop an innovative post-form strength prediction (PFS) model to accurately predict strength and microstructure evolutions of the material under complex thermo-mechanical loading conditions. Verify the capability of the novel PFS model utilising results of the forming trials performed on a pilot production line.

4. Build an advanced functional module 'Tailor' incorporating the PFS model and the automatic optimisation algorithm. Implement the functional module into a cloud based FEA platform.

1.3 Outline of the thesis

Chapter 2 introduces state-of-art forming technologies for sheet metals, such as a typical hot stamping technology (HFQ®) and a novel Fast light Alloys Stamping Technology (FAST). This chapter provides a comprehensive literature review on precipitation hardening theories of heat treatable Al-Mg-Si alloys and existing precipitation hardening models, including KWN microstructure model, Shercliff and Ashbys' strength model and various extended models for the material under different conditions.

Chapter 3 demonstrates the experimental methodology to investigate the viscoplastic behaviour, quenching sensitivity and precipitation response of 6xxx aluminium alloys. A series of systematic experiments including ultra-fast heating tests, uniaxial tensile tests, quenching tests, artificial ageing tests, EDXS tests, TEM observations and forming trials were conducted.

Chapter 4 analyses the changes in mechanical properties and microstructural evolutions during complex thermo-mechanical processes, which involves ultra-fast heating, high temperature plastic deformation, rapid/slow quenching and post-form multi-stage heat treatment. A good understanding to the nature of the novel stamping technology was achieved through the discussion of decoupled experimental results, which provides the foundation to develop the post-form strength prediction model.

Chapter 5 details the development and calibration of the innovative post-form strength prediction (PFS) model for Fast light Alloys Stamping Technology (FAST). It is comprised of five sub-models: flow stress model, quenching model, artificial ageing model, multi-stage artificial ageing model and particle size distribution (PSD) sub-model. First four sub-models aim to predict strength evolution of 6xxx aluminium alloys under various manufacturing conditions and the PSD sub-model offers an additional function of simulating size distribution of precipitates.

Chapter 6 illustrates the development of the functional module 'Tailor' that incorporates automatic optimisation algorithm and the implementation of 'Tailor' into a cloud based FEA platform. The constructed predictive module 'Tailor' is capable of automatically self-optimising the material parameters used in the PFS model within pre-defined boundaries as well as accurately predicting strength evolution of Al-Mg-Si alloys.

Chapter 7 summarises the findings and proposes suggestions for future works. In the future research, it is promising to study the effect of ultra-fast heating on the precipitation response and extend the model to the blank material with different tempers. The capability of the PFS model would be expanded significantly when applying to 7xxx aluminium alloys and other sheet forming technologies.

Chapter 2. Literature review

This chapter aims to provide an overview of the state-of-art sheet metal forming technologies and the required theoretical knowledge to develop the post-form strength prediction model of 6xxx series aluminium alloys.

Aluminium alloys can be broadly categorised into two principle groups: casting alloys and wrought alloys. Typically, the mechanical properties (e.g. tensile strength), surface finish and structural integrity of casting alloys are inferior to wrought alloys (Polmear, 1995). Therefore, wrought alloys are often used for complex-shaped structural components whereas casting alloys are used for cost-effective non-uniform thickness components such as engine cylinder heads and gearbox housing (Kaufman, 2000). Each wrought aluminium alloy is identified with a four-digit number provided by the International Alloy Designation System, where the first digit indicates the major alloying element as shown in Table 1.1.

Table 1.1: Wrought aluminium alloy designation system (Davis, 1993)

Alloys series	*Major alloying element(s)*
1xxx	Commercial aluminium with a minimum 99% purity
2xxx	Copper
3xxx	Manganese
4xxx	Silicon
5xxx	Magnesium
6xxx	Magnesium and Silicon
7xxx	Zinc
8xxx	Other elements such as Ni, Ti, etc.

With regard to heat sensitivity and hardening mechanism, the wrought alloys can be further divided into two types: heat-treatable and non-heat-treatable alloys (Davis, 1993). Non-heat-treatable aluminium alloys refer to 1xxx, 3xxx, 4xxx and 5xxx series alloys as these alloys consist of homogeneous solid solution and they are mainly strengthened by cold working while no obvious strengthening can be achieved by conducting heat treatment. 2xxx, 6xxx and 7xxx aluminium alloys are heat-treatable with an essential dependence on temperature that the equilibrium solid solubility of the alloying elements increases with increasing temperature. The

material exhibits remarkable strength enhancement when subjected to the heat treatment involving three basic steps: solution heat treatment, quenching and natural ageing/artificial ageing.

The focus of the present research has been placed on the heat treatable 6xxx series aluminium alloys that are alloyed with magnesium and silicon with good formability, weldability, machinability, corrosion resistance and high strength.

2.1 Sheet metal forming technologies for aluminium alloys

In order to realise mass reduction of vehicles and maintain the constant vehicle size and performance, the demand for aluminium sheet parts with different geometries and properties has increased drastically (Ramezani and Ripin, 2012). Existing advanced sheet metal forming technologies for aluminium alloys are reviewed.

2.1.1 Hot stamping

It remains a challenge to successfully form structural components from high strength aluminium alloys whilst maintaining high strength. The formability of aluminium alloys at room temperature is limited and past studies indicate that these alloys exhibit significantly increased formability at elevated temperatures (Bariani et al., 2013; Mohamed et al., 2012). The hot stamping process has been developed to manufacture high-strength parts with high dimensional complexity, which extends the application of aluminium alloys in the automotive industry. The schematic diagram in Figure 2.1 demonstrates the temperature profiles and microstructural evolutions of a hot stamping technology named HFQ® (Lin et al., 2008).

During the HFQ® technology, the blank is heated in the chamber furnace to the solution heat treatment temperature and soaked for approximately 30 minutes (6xxx series aluminium alloys), ensuring the second phase precipitates are dissolved in the matrix (Garrett et al., 2005). Longer periods of soaking are usually beneficial for the formability of the material, as they ensure that the precipitates are fully dissolved. However, overheating could lead to material melting and hence occurrence of undesired microstructures with inclusions (Garrett et al., 2005; Totten and MacKenzie, 2003a). The hot blank is then transferred to the press machine to be formed immediately with a high stamping speed. The workpiece is held in the dies with a pre-defined

die closing force, which allows the in-die quenching to be conducted effectively and, as desired, a microstructure of supersaturated solid solution (SSSS) is obtained. A quenching rate above the critical quenching rate of the workpiece material is essential to avoid the formation of coarse precipitates on the grain boundaries which diminishes the artificial ageing response of the workpiece. To restore the full strength of the material, artificial ageing taking up to 8 hours is subsequently utilised (Gupta et al., 2001).

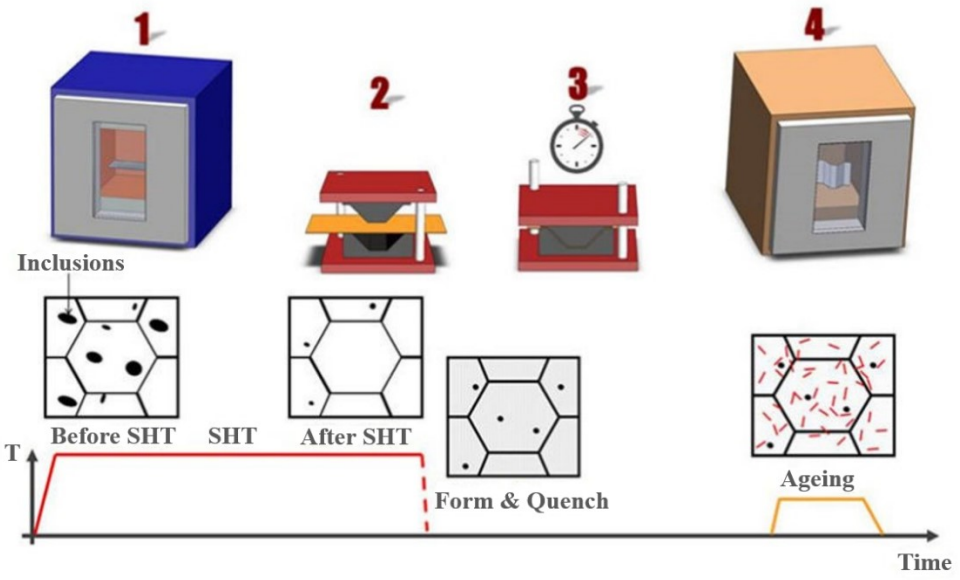

Figure 2.1: Processing route of Solution heat treatment, Forming, and in-die Quenching (HFQ®) (Imperial College London, 2017)

The HFQ ® process provides the opportunity to form complex shaped parts from high-strength sheet aluminium alloys with the desired microstructure. The combination of solution heat treatment, hot stamping and quenching reduces the intricate manufacturing processes. Detrimental post-form springback and distortion are minimised owing to the cold die quenching and holding. It is noticed that at a high temperature close to SHT temperature, melting of the precipitates and inclusions appears to cause severe grain boundary softening and deteriorates the formability of 2xxx and 7xxx aluminium alloys (Gao et al., 2017; Wang et al., 2011). The lengthy solution heat treatment and post-form artificial ageing limit the application of this technology in high volume production (Zheng et al., 2018).

2.1.2 Fast light Alloys Stamping Technology (FAST)

A novel Fast light Alloys Stamping technique has recently been developed for the mass production of complex-shaped high strength aluminium panel components (Wang et al. 2017; Luan et al., 2016).

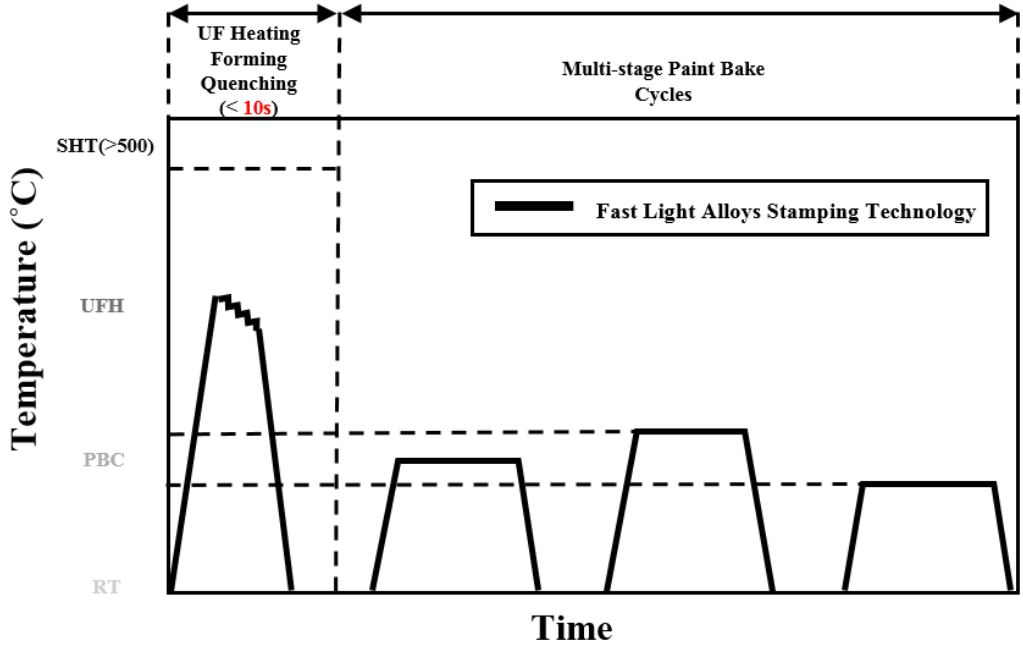

Figure 2.2: Schematic working principle for FAST

The working principle and corresponding microstructural evolution during FAST process are illustrated in Figure 2.2 (Zhang et al., 2019). During the FAST process, the 6xxx series aluminium alloy sheet blank is heated to an elevated forming temperature (lower than SHT temperature) at an ultra-fast heating rate (normally over 50°C/s) within several seconds to avoid the formation of unexpected precipitates. Then it is transferred to a press and formed immediately to avoid excessive heat loss so that the blank maintains its temperature and therefore, sufficient formability. Quenching is completed in cold dies to ensure the critical quenching rate can be achieved. The material is able to be stored at room temperature without the unfavourable natural ageing effect on the strength recovery. The required artificial ageing time is also reduced.

The FAST technology exhibits great advantages to boost mass production of high-strength structural panel components from sheet 6xxx series aluminium alloys with high production rate and low energy consumption. In the conventional hot stamping technology, the blank material is soaked at solution heat treatment (SHT) temperature for 30 minutes and cooled to the target

forming temperature afterwards. The lengthy SHT increases the energy consumption greatly and limits the industrial application in high volume production. The complicated temperature evolution also increases the risk of the degradation of precipitation response in the subsequent artificial ageing due to the formation of undesired precipitates during cooling from SHT temperature to forming temperature. Comparatively, the material is heated to the target forming temperature directly at an ultra-fast heating rate and formed immediately in the revolutionary FAST forming process. Therefore, it eliminates the lengthy solution heat treatment and the unnecessary cooling completely prior to stamping, offering flexible forming at different target temperatures and reducing the artificial ageing time after stamping to achieve a unique and unprecedented enhancement in the production rate. The manufacturing cycle time (except paint bake cycles) is reduced from more than 10 hours to less than 20 seconds, significantly improving the manufacturing efficiency (Luan et al., 2016). However, the requirements for the blank material are more stringent as the initial microstructures need to be customised in order to complete the forming process and recover the strength simultaneously.

2.2 Precipitation hardening Processes

Precipitation hardening is a heat treatment technique to enhance the mechanical properties of heat-treatable aluminium alloys, which usually involves solution heat treatment, quenching and artificial ageing (or natural ageing). The material is strengthened with the formation of the second phase nano-scale precipitates in the aluminium matrix, hindering the dislocation movements by forcing the dislocations to either cut through small precipitates or bypass large ones. Significant research has been conducted to investigate the underlying theories of precipitation hardening.

2.2.1 Solution heat treatment (SHT)

Solution heat treatment (SHT) is a thermal process in which the material is heated to a suitable temperature and held for a given time (Davis, 1993). The blank material is heated to a temperature between solvus and eutectic melting temperature, and maintained for a specified period of time to dissolve all the soluble hardening alloying elements into the aluminium matrix. The homogeneous supersaturated solid solution (SSSS) is produced on the basis of accurate control of the SHT temperature and time. The alloying elements cannot be absorbed into the matrix unless the soaking time is sufficiently long. Otherwise, the incomplete SHT would lead

to lower strength recovery after subsequent heat treatment. Usually, the treatment is required to avoid excessive soaking time or exposure to exceeding temperature. Overheating may result in the degradation of tensile strength, ductility and fracture toughness due to the melting of complex eutectics and surface oxidation (Totten and MacKenzie, 2003a). It is suggested that optimal SHT conditions for 6xxx series aluminium alloys are soaking for approximately 30 minutes at 535°C (Aluminium Federation, 2014).

2.2.2 Quenching

Quenching is a critical operation in the heat treatment sequence, during which the material is cooled rapidly from the SHT temperature to a lower temperature, usually close to room temperature. The objective of quenching is to preserve the SSSS state achieved from SHT and maintain a certain number of quenched-in vacancies in the matrix (Totten and MacKenzie, 2003b). The alloying elements kept in the solid solution as well as the retained quenched-in vacancies favour the formation of desired microstructures when the material is age hardened. If insufficient quenching is applied, undesirable second phase particles would precipitate around grain boundaries, small voids and dislocations (Cavazos and Colás, 2001). The existence of such precipitates adversely affects the precipitation response and fails to restore the peak strength in the subsequent artificial ageing processes (Cavazos and Colás, 2003). Therefore, in most instances, rapid quenching is employed to avoid the formation of these types of precipitates and the minimum required quenching rate is called the critical quenching rate. Most frequently, water quenching, oil quenching and cold die quenching are utilised to efficiently quench the parts.

The quenching sensitivity of 6xxx aluminium alloys has been frequently investigated by study the heat flow via differential scanning calorimetry (DSC) experiments and intensive microstructural analysis including transmission electron microscopy (TEM) observations (Milkereit et al., 2010, 2009; Osten et al., 2015). The precipitation response is determined through the analysis of the exothermic and endothermic peaks in the DSC curves and microstructural observations in TEM images. The continuous cooling precipitation (CCP) diagrams are derived accordingly to demonstrate the precipitation behaviour during quenching from solutionising temperature as a function of temperature and time. Apart from time and temperature, the CCP diagram is highly dependent on the chemical composition and initial temper of the raw material (Milkereit and Starink, 2015). Due to the strong dependency on

several parameters that are intermixed in different studies and limitations of existing experimental equipment, the detailed precipitation behaviour for a particular material remains unknown and corresponding literature are insufficient. Milkereit et al. have conducted a series of DSC, TEM, artificial ageing tests to explore the time and temperature dependent precipitation quenching behaviours and summarised the CCP diagrams for 6xxx series alloys (Milkereit et al., 2012). Figure 2.3 shows the CCP diagrams for AW-6082 alloys with different chemical compositions. AA6082 with higher mass fraction of Mg and Si usually exhibits higher strength and is more sensitive to the quenching rate.

(a)

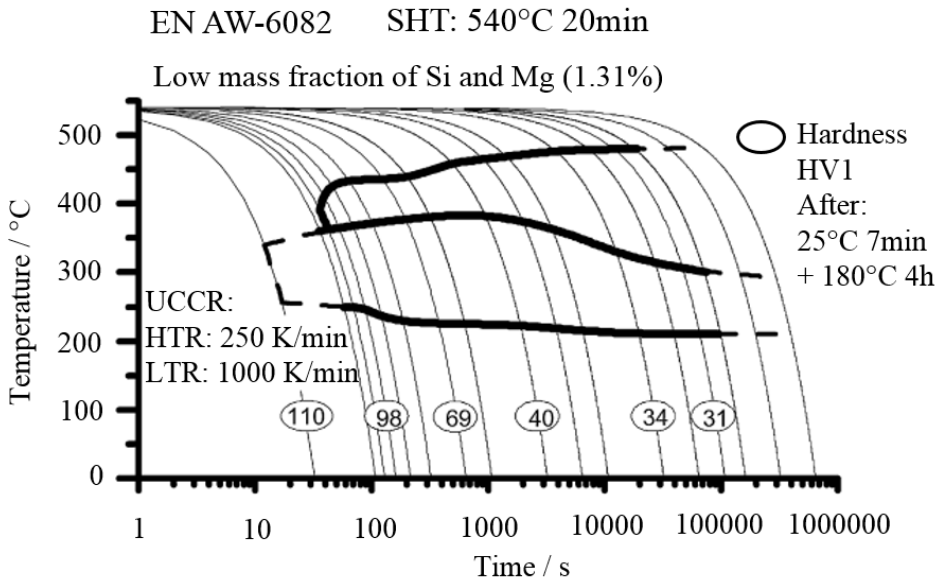

(b)

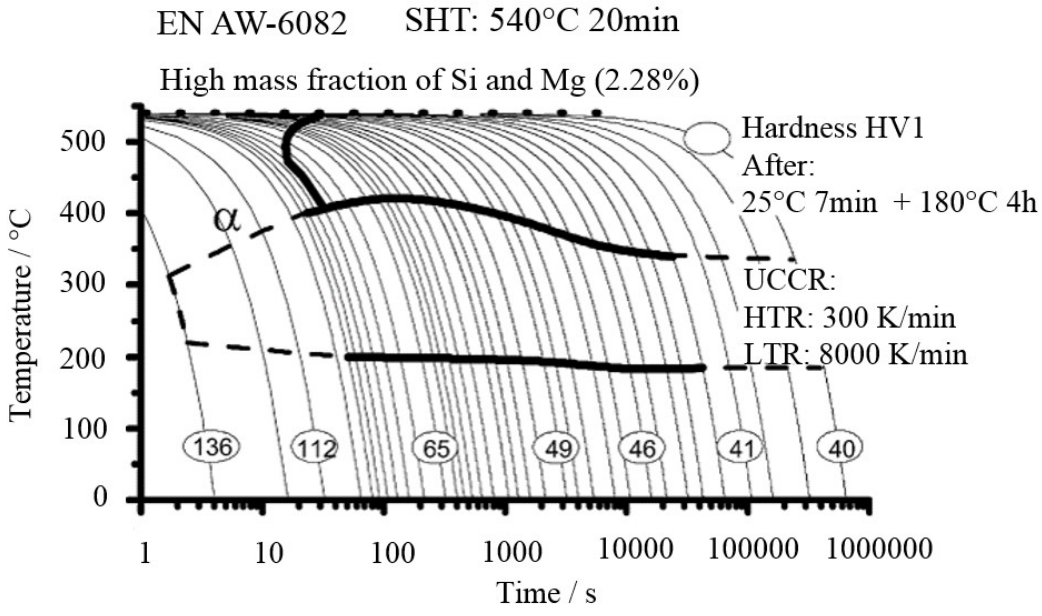

(c)

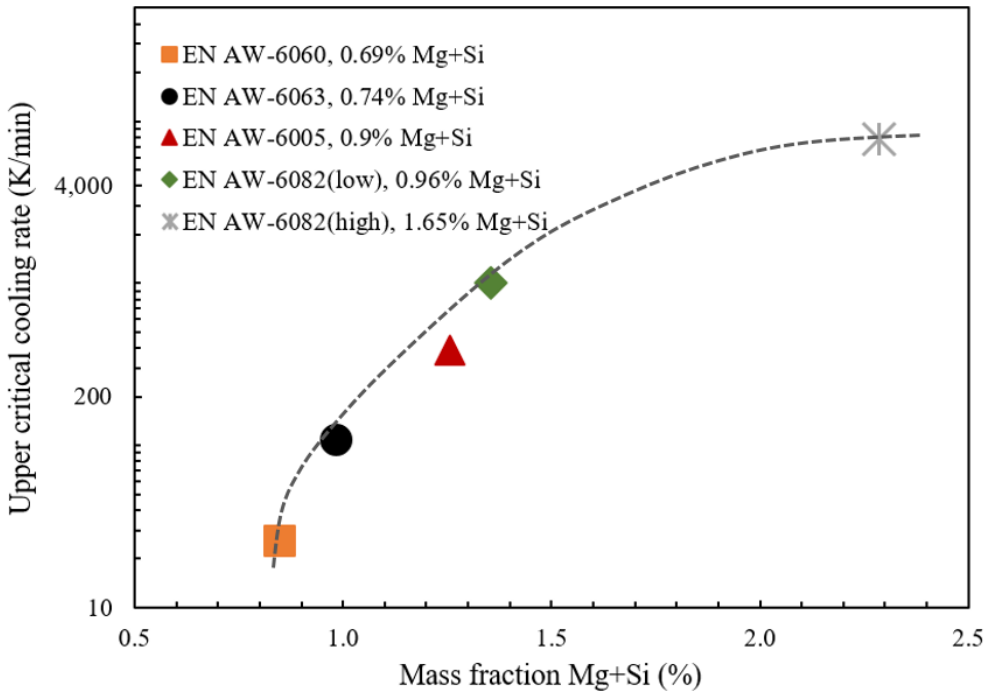

Figure 2.3: (a) Continuous Cooling Precipitation (CCP) diagram of AW-6082 with a low mass fraction of Mg + Si, (b) CCP diagram of AW-6082 with a high mass fraction of Mg + Si and (c) upper critical cooling rate of the investigated Al-Mg-Si alloys as a function of mass fraction of Mg + Si (Milkereit et al., 2012)

It was found that the high-temperature reaction is related to the formation of the equilibrium β phase (Mg_2Si) precipitates and low-temperature reaction corresponds to the precipitation of pre-cursors (β') of the major hardening phase when the quenching curves cross the CCP curves. The critical quenching rate is also sensitive to the mass fraction of alloying elements. Generally, the critical quenching rate increases with the increasing mass fraction of Mg and Si as shown in Figure 2.3. (c).

2.2.3 Natural ageing

In the as-quenched material, solute atoms tend to form co-clusters of Mg and Si via diffusion at room temperature, which is referred as natural ageing (Badini et al., 1991). The effect of natural ageing increases yield strength gradually and it stabilises after approximately 7 days (Cuniberti et al., 2010). Studies of Al-Mg-Si alloys with different natural ageing histories indicate that the presence of low-temperature clusters has a negative effect on the precipitation response as they survive in artificial ageing and cannot provide nucleation sites for the

formation of β'' precipitates (Esmaeili et al., 2003a, 2003c; Murayama and Hono, 1999). Hence, the obtained mechanical properties after appropriate artificial ageing degrade. Cuniberti et al. performed extensive experiments to investigate the influence of natural ageing on precipitation response and drew the conclusions: (i) natural ageing suppresses the artificial ageing response in the early stage; (ii) the coarser β'' precipitates lead to a suboptimal distribution pattern and lower precipitation volume fraction; (iii) there is a slight loss in the peak strength although the time to reach peak strength is not altered (Cuniberti et al., 2010). The comparison of hardness evolution between samples with/without natural ageing is displayed in Figure 2.4.

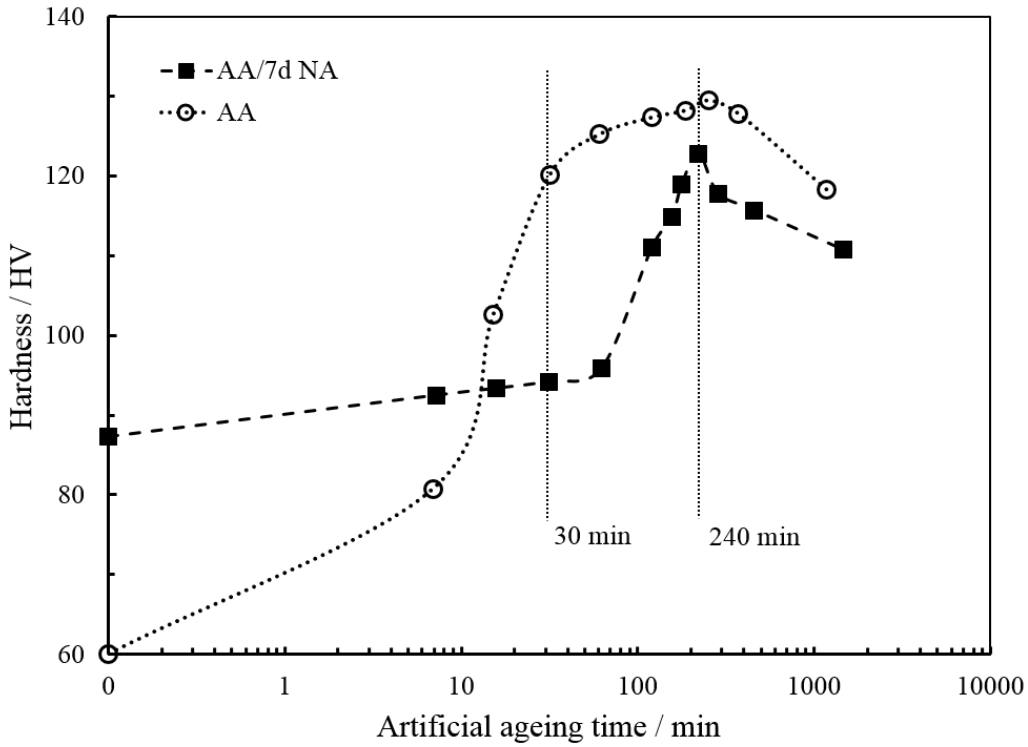

Figure 2.4: Hardness for samples aged at 180°C without previous natural ageing and with 7-days natural ageing (Cuniberti et al., 2010)

However, research has also indicated that the mass fraction of Mg and Si plays a decisive role in natural ageing. It is reported that natural ageing has a detrimental effect only when the alloy contains high solute content (Mg + Si > 1%) (Torsæter et al., 2010). Martinsen et al. claimed that the negative natural ageing effect of high solute Al-Mg-Si alloys is a transient phenomenon and can be reversed completely by sufficiently extending the room temperature storage time (Martinsen et al., 2012). On the other hand, the material with low solute content (Mg + Si < 1%) would reach an even higher peak strength compared with the material without room

temperature storage (Chang et al., 2009; Røyset et al., 2006). Therefore, the effect of natural ageing is still controversial and additional research is required to draw firm conclusions.

2.2.4 Artificial ageing

Normally, the SSSS material is strengthened by artificial ageing processes after SHT and effective quenching. The material is held at an elevated temperature (normally ranging from 150 to 250°C for Al-Mg-Si alloys) and soaked for a period of time to allow the formation of hardening second phase precipitates. Numerous studies have generally accepted the precipitation sequence for commercial Al-Mg-Si alloys in artificial ageing as shown in Figure 2.5 (Chrominski and Lewandowska, 2016; Du et al., 2017; Dutta and Allen, 1991; Esmaeili et al., 2003c; Gracio et al., 2004; Gupta et al., 2001; Perovic et al., 1999).

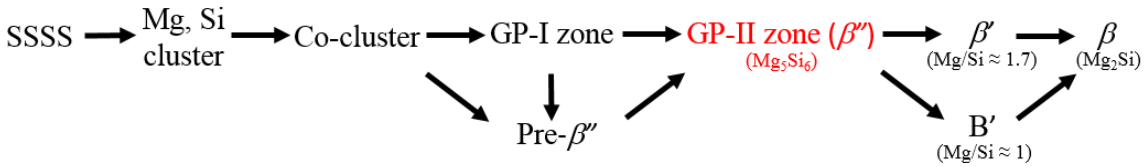

Figure 2.5: Precipitation sequence of Al-Mg-Si alloys

The starting point of the precipitation process is the supersaturated solid solution (SSSS) produced by SHT and quenching. An excess amount of solute elements are homogeneously dissolved through the matrix and yield local strain on the surrounding Al atoms (Wolverton, 2007). Massive quenched-in vacancies assist in the diffusion of the solute atoms and the supersaturation provides a large driving force to surpass the energy barrier for precipitation that initiates the formation of Si clusters and Mg clusters. The coherent co-clusters of Si and Mg appear through the dissolution of separate clusters of single element and absorption of Mg atoms in the solution (Edwards et al., 1998). These co-clusters are named GP-I zones/pre-β'' precipitates. As artificial ageing proceeds, needle-shaped GP-II zones / β'' (3-4 nm in diameter and 10-20 nm in length) begin to form around nucleation sites, which is associated with the peak strength of the material. Subsequently, the formation of semi-coherent rod-shaped precipitate β' will commence signalling an over-aged state. Eventually, equilibrium β phase precipitates are formed leading to a steep decrease in strength. The microstructural evolutions observed in different stages of artificial ageing are shown in Figure 2.6 (Poole et al., 2005):

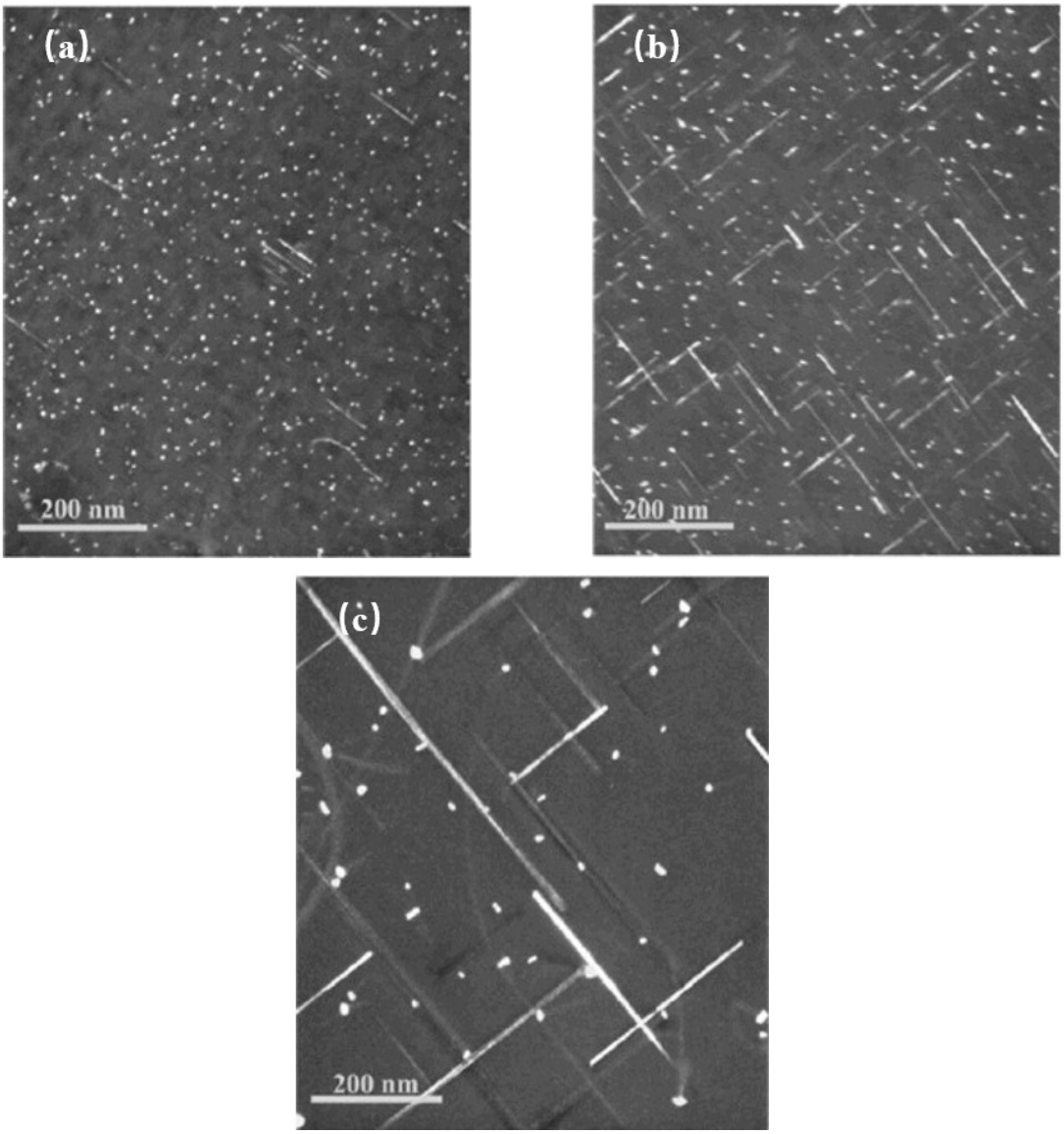

Figure 2.6: TEM images of precipitates along <100> axis of Al-Mg-Si alloys at different ageing conditions (a) under-aged, (b) peak-aged and (c) over-aged

The metastable Mg_5Si_6 *β''* precipitates nucleate along the <100> axis in the aluminium matrix. T6 temper of the material (peak strength) is believed to be acquired with a fine distribution of the mix of needle-shaped *β''* precipitates and minor rod-shaped *β'* precipitates in optimal size.

It is vital to control the artificial ageing conditions to attain the optimal alloy properties. The time required to reach peak strength and the attainable peak strength differ when the material is exposed to different artificial ageing temperatures. At high temperatures, the precipitation kinetics are accelerated as larger diffusion energy is provided, hence the time to reach T6 temper is reduced. However, the loss of peak strength appears with increasing ageing

temperature as the coarser distribution of precipitates weakens the capability of the second phase precipitates to hinder dislocation motions (Polat et al., 2015). It normally takes around 8 hours of artificial ageing to strengthen the as-quenched AA6082 workpiece to T6 temper (Gupta et al., 2001).

2.3 Modelling the precipitation hardening phenomena

Precipitation hardening involving SHT, quenching and artificial ageing, is the most effective approach to strengthen the heat-treatable aluminium alloys. The final mechanical properties are highly dependent on the thermo-mechanical histories and therefore it is crucial to impose reasonable heat treatment conditions on the workpiece. Significant progress has been made in the modelling of precipitation kinetics and strengthening response of Al-Mg-Si alloys during the artificial ageing through the past three decades. The multi-stage microstructural transformations such as nucleation, growth and coarsening are modelled through the complicated correlation of several critical microstructural variables including size of precipitates, volume fraction of precipitates and solute concentration.

2.3.1 Strengthening mechanism

The strengthening of heat treatable 6xxx series aluminium is considered as the aggregation of intrinsic strength of aluminium matrix (σ_i), solid solution strength (σ_{ss}) and precipitation strength (σ_{ppt}) as shown in Eq. (2-1) (Esmaeili et al., 2003b; Esmaeili and Lloyd, 2005). Figure 2.7 presents a schematic diagram illustrating the summative nature of each contribution effect on the overall strength (Shercliff and Ashby, 1990). It is obvious that the overall strength shares the similar evolution with the strength contribution of precipitates in the artificial ageing process, confirming that precipitation hardening profoundly affects the strength of the material.

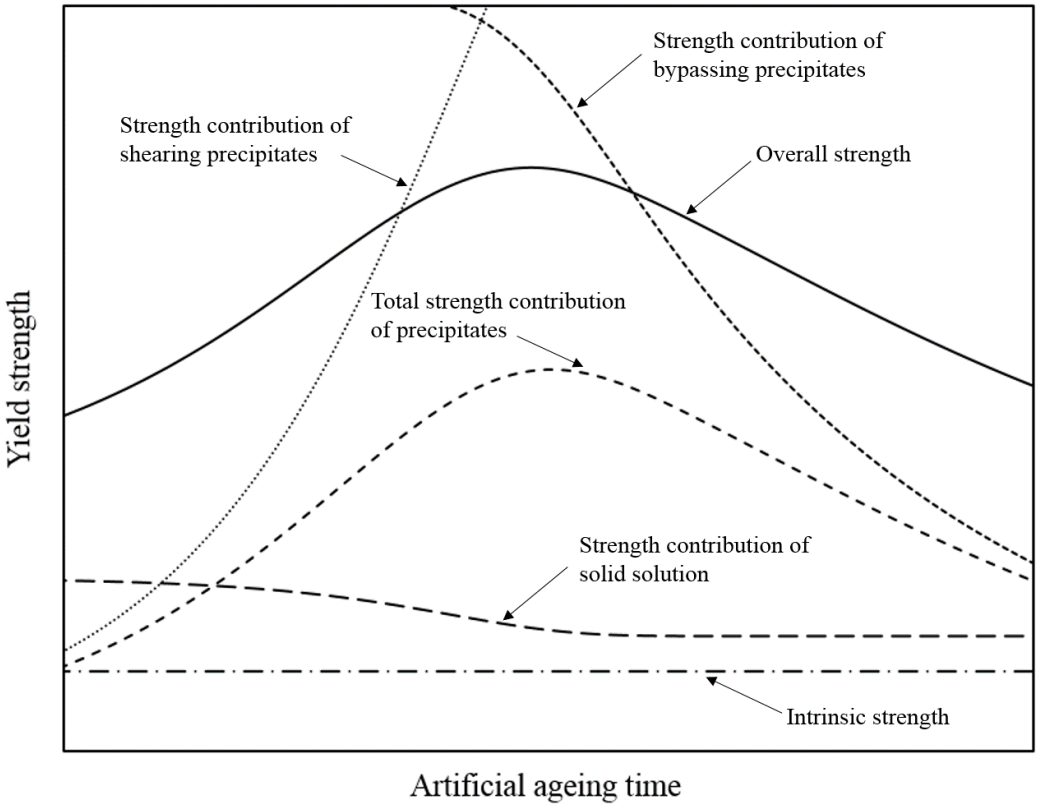

Figure 2.7: The schematic diagram of contributions of each strengthening term to overall strength of the material during artificial ageing (Shercliff and Ashby, 1990)

$$\sigma_y = \sigma_{ss} + \sigma_i + \sigma_{ppt} \tag{2-1}$$

In the early stage of artificial ageing, the size (usually represented by mean radius) of precipitates is relatively small and the coherency with the matrix is high, the dislocation lines are able to cut through the second phase particles directly. The dominant strengthening mechanism in this case is termed as shearing hardening. Continuing the artificial ageing at a constant temperature, the evolved precipitates are too large to be sheared by dislocations. The bowing theory proposed by Orowan is applied to explain the bypassing hardening mechanism in this circumstance (Orowan, 1948). These non-shearable precipitates act as pining points and lead to dislocations 'looping' around them, which results in the formation of dislocation rings (also called Orowan loops). The dominant hardening mechanism usually experiences a transition from shearing to bypassing during the artificial ageing as a function of the mean radius of precipitates (Poole et al., 2005). The overall precipitation hardening can be expressed by the harmonic mean of shearing contribution and bypassing contribution. Eq. (2-1) is then modified to Eq. (2-2). The schematic diagrams of shearing strengthening, bypassing

strengthening and the qualitative relationship between particle size and dominant strengthening mechanism are illustrated in Figure 2.8.

$$\sigma_y = \sigma_{ss} + \sigma_i + \frac{\sigma_{by} \cdot \sigma_{sh}}{\sigma_{by} + \sigma_{sh}} \quad (2\text{-}2)$$

(a)

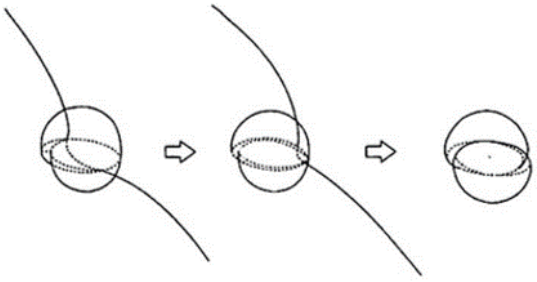

(b)

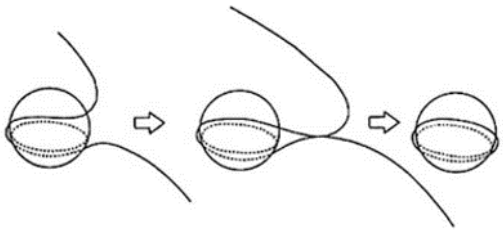

(c)

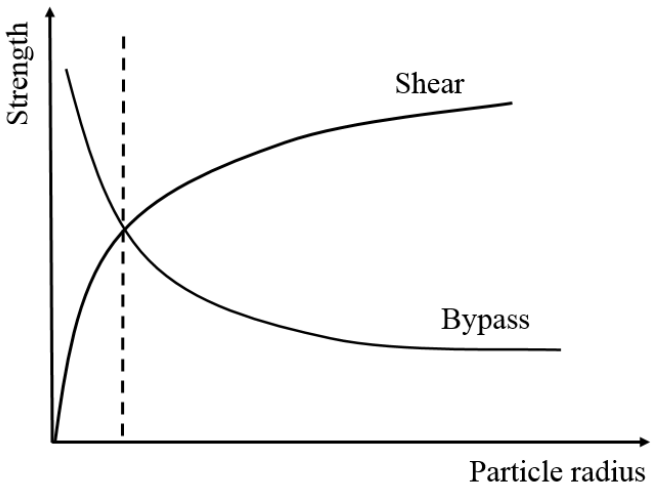

Figure 2.8: (a) Shearing mechanism, (b) bypassing mechanism and (c) qualitative relationship between precipitate radius and the dominant strengthening mechanism (Casari, 2014)

Precipitation hardening involves a complex series of physical transformations in the alloys at atomic and microstructural levels, which is mainly determined by size of precipitates and the distribution pattern. The overall strength is computed by the correlations of key microstructural variables such as mean radius of precipitates (r), volume fraction of precipitates (f_t) and solute concentrations (C_t).

$$\sigma_y = f(f_t, r, C_t) \tag{2-3}$$

Based on the microstructural phenomenon, the precipitation process is usually split into three elementary stages: nucleation, growth and coarsening (Lifshitz and Slyozov, 1961). In the very beginning, the supersaturation of the matrix provides a large driving force with the aid of the quenched-in vacancies and numerous tiny precipitates begin to nucleate around the nucleation sites. The volume fraction of the precipitates experiences a rapid increase and the solute concentration of alloying atoms decreases correspondingly. The nucleated precipitates will either grow as precipitation proceeds via absorbing the solute atoms from the solid solution, or dissolve in the matrix. This depends on whether the precipitate/matrix interface concentration exceeds the mean solute concentration of the matrix (Dunning, 1973; Marqusee and Ross, 1983). The shrinkage of smaller precipitates contributes to the growth of larger precipitates. The mean radius and the volume fraction of precipitates continues increasing until the latter reaches the equilibrium value at a certain ageing temperature. The equilibrium volume fraction of precipitates and solute concentration of the solid solution is the function of artificial ageing temperature and can be expressed by Shewmon's law (Shewmon, 1963). Subsequently, coarsening becomes the dominant mechanism with a sharp increase in the size of precipitates while the volume fraction and the solute concentration remain the same. As long as the ageing time is sufficiently long, all the precipitates in the matrix will coarsen to a single large remaining particle according to the monomer deposition theory (Madras and McCoy, 2005). The relevant evolutions of nucleation rate, number density of precipitates, mean radius and critical radius (determines growth or shrinkage) of precipitates during prolonged artificial ageing at 180°C are shown in Figure 2.9:

(a)

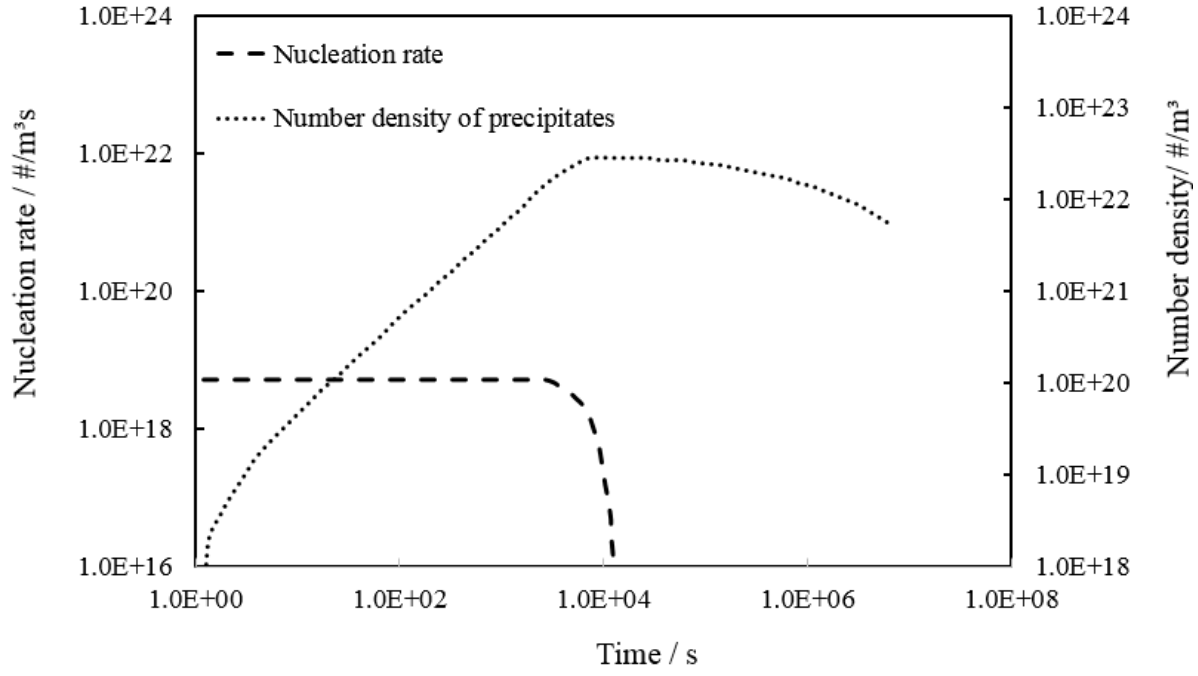

(b)

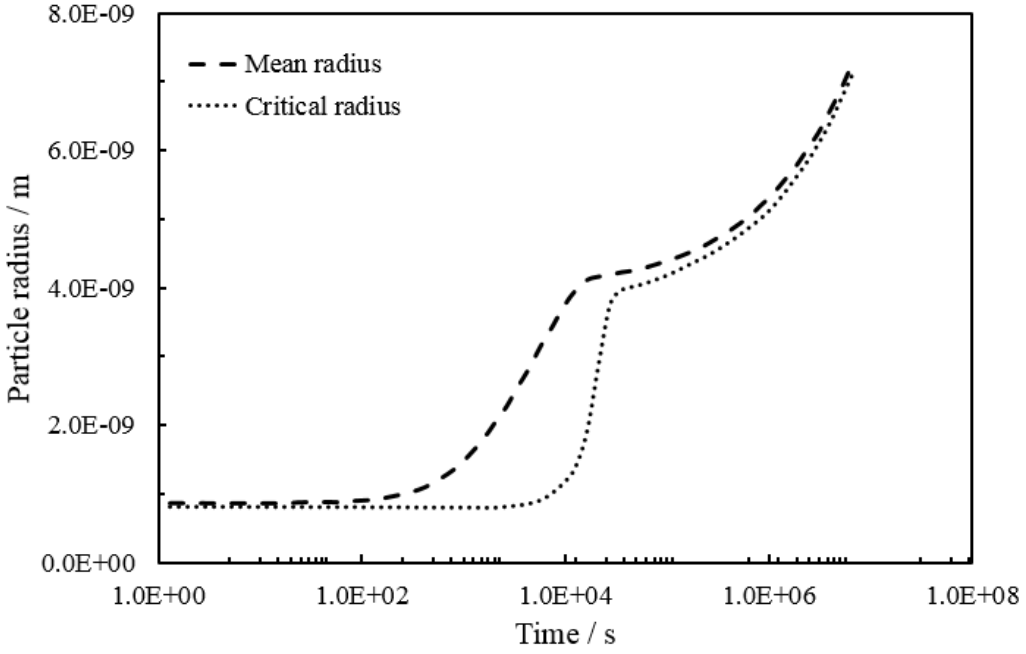

Figure 2.9: Evolutions of (a) nucleation rate and number density of precipitates and (b) mean radius and critical radius during prolonged artificial ageing at 180°C (Myhr and Grong, 2000)

2.3.2 Strength models

Various models have been developed to predict the strength evolution of 6xxx Al-Mg-Si alloys during artificial ageing. The models are established via the correlation of microstructural parameters during each stage of the precipitation process.

2.3.2.1 KWN microstructure model

Precipitation kinetics of static artificial ageing followed by SHT was accomplished first by Kampmann and Wagner (Kampmann et al., 1985). The numerical model was known as the KWN method. One of the important assumptions made in the model is that: nucleation, growth and coarsening are not independent processes in the entire precipitation process. The numerical approach is capable of capturing the precipitation nucleation-growth-coarsening phenomena and predicting the particle size distribution. The precipitates are divided into a series of discrete size class in the time domain. The nucleation rate j is expressed in Eq. (2-4)

$$j = j_0 \exp\left(-\frac{\Delta G^*_{het}}{RT}\right) \exp(-\frac{Q_d}{RT}) \tag{2-4}$$

where j_0 is the pre-exponential term of nucleation, ΔG^*_{het} is the energy barrier for nucleation and Q_d is the activation energy of diffusion. The nucleation rate remains high and drops off with the significant loss of solute atoms from the solution. The nucleation process stops eventually when the mean solute concentration in the matrix approaches the equilibrium solute concentration at the particle/matrix interface.

To simplify the computation process, the precipitates are assumed to be spherical with the radius r. In the growth and coarsening process, most of the formed precipitates keep growing while the remainder shrink quickly, depending on whether the radius is greater than the critical radius. The expressions for the critical radius and growth rate are shown in Eqs. (2-5) and (2-6) (Aaron et al., 1970).

$$r_c = \frac{2\gamma V_m}{RT} (\ln(\frac{C_t}{C_e}))^{-1} \tag{2-5}$$

$$v = \frac{d_r}{d_t} = \frac{C_t - C_{int}}{C_p - C_{int}} \frac{D}{r} \tag{2-6}$$

where r_c is the critical radius, γ is the particle-matrix interface energy, V_m is the molar volume of the particle, v is the growth rate, C_t is the mean solute concentration in the matrix, C_e is the equilibrium solute concentration in the matrix, C_{int} is the solute concentration at the particle/matrix interface and C_p is the solute concentration in the precipitates. The critical radius relies on the current values of C_t and C_e. C_e is a function of the temperature so that the prediction of microstructural evolutions during non-isothermal heat treatment is considered as well. For instance, the ideal artificial ageing condition is to age the material isothermally at a constant temperature. However, in the practical process, the workpiece is heated from a lower temperature to the target ageing temperature. In this case, the temperature dependent prediction of C_e enables the accurate simulation of the heating stage.

2.3.2.2 Shercliff and Ashby strength model

Later, Shercliff and Ashby proposed a process model to couple the precipitation process with a dedicated strength model (Shercliff and Ashby, 1990). The hardening phenomenon was considered as a superposition of precipitation hardening (bypassing and shearing), solid solution hardening and intrinsic matrix hardening. The yield strength model is able to predict the strength evolution of the material via correlation of three major internal state variables: solute concentration, volume fraction of precipitates and mean radius of precipitates.

The mean solute concentration in the matrix is assumed to decay exponentially with time when subjected to a constant artificial ageing temperature.

$$C_t = C_e + (C_i - C_e) \cdot e^{-\frac{t}{\tau}} \tag{2-6}$$

where C_t is the transient solute concentration in the matrix, C_e is the equilibrium solute concentration at ageing temperature, C_i stands for initial solute concentration and τ is a temperature-dependent constant indicating the decay speed.

With the simplification that all precipitates share identical stoichiometry and uniform thermodynamic properties, the volume fraction of the precipitates are only dependent on the amount of solute atoms precipitated from the solid solution. The increase of volume fraction is proportional to the solute loss in the aluminium matrix.

$$f_t = f_e \cdot \frac{C_i - C_t}{C_i - C_e} \tag{2-7}$$

where f_t is the transient volume fraction and f_e is the equilibrium volume fraction at a certain ageing temperature. It is noted that both equilibrium solute concentration and volume fraction are temperature-dependent. Conventionally, the higher artificial ageing temperature yields a lower equilibrium solute concentration and greater equilibrium volume fraction. The maximum volume fraction and minimum solute concentration are obtained at absolute zero, where all the alloying elements are precipitated out from the pure aluminium matrix with no mobility.

The cubic coarsening law is applied to compute the mean radius of all the formed precipitates (Lifshitz and Slyozov, 1961).

$$r^3 - {r_0}^3 = C_1 \cdot \frac{t}{T} e^{-\frac{Q_A}{RT}} \tag{2-8}$$

where r_0 is the initial mean radius of precipitates, C_1 is the coarsening constant and Q_A is the activation energy for diffusion. r_0 equals to 0 when the material is aged immediately from the supersaturated solid solution.

Based on the solution hardening theory, Friedel effect and Orowan bowing theory, the contributions of solid solution, shearing precipitates and bypassing precipitates are modelled as shown in Eqs. (2-9) – (2-11). The overall precipitation hardening is the harmonic mean of shearing hardening and bypassing hardening.

$$\sigma_{sh} = C_2 \cdot {f_t}^{1/2} \cdot r^{1/2} \tag{2-9}$$

$$\sigma_{by} = C_3 \cdot {f_t}^{1/2} \cdot r^{-1} \tag{2-10}$$

$$\sigma_{ss} = \sum_j k_j \cdot {C_j}^{2/3} = C_4 \cdot {C_t}^{2/3} \tag{2-11}$$

C_j, C_2, C_3 and C_4 are the effective material constants (equivalent values containing different parameters) describing the interaction between resistance to dislocation motions and properties of the precipitates.

2.3.2.3 Extended models

The development of KWN microstructure model and Shercliff and Ashbys' strength model allow the accurate prediction of the microstructural nature as well as the strength evolutions during static artificial ageing for the Al-Mg-Si material in the supersaturated solid solution state. Over the last two decades, the functionality of these classic microstructure and strength models have been further extended and applied to more complicated systems with various conditions.

Researchers have also made great efforts to investigate the effect of precipitates morphology on the precipitation response. In the original model, precipitates are assumed to be in the spherical shape with a constant aspect ratio (length over radius). In order to model the contributions of rod-shaped, needle-shaped and plate-shaped precipitates on the overall yield strength, the length and the aspect ratio are taken into consideration during different stages of artificial ageing (Bahrami et al., 2012; Liu et al., 2003). Furthermore, the transition from shearable to non-shearable precipitates during ageing has been defined and the contribution of non-spherical precipitates has also been embedded (Du et al., 2016; Holmedal et al., 2016). Diffusion-controlled needle-shaped precipitation growth rate and the interfacial phase composition are correspondingly considered.

In addition, extended models were developed to simulate microstructural evolutions for materials under different heat treatment or deformation conditions. Esmaeili et al proposed a refined model for the precipitation hardening of the naturally-aged 6xxx aluminium alloys, considering the deleterious effects of natural ageing (Esmaeili et al., 2003a). The volume fraction of clusters formed $f_{clusters}$ during natural ageing is modelled and then implemented in the artificial ageing model. This model considers the kinetics of strengthening precipitates and dissolution of room temperature clusters concurrently with different levels of natural ageing. Pre-ageing is widely utilised to eliminate the adverse effect of natural ageing and improve the stability of the as-quenched material stored at room temperature. Accordingly, the model for pre-aged Al-Mg-Si alloys during artificial ageing has been established with the

correction factor *m* induced, which describes the level of maximum possible precipitate content for a regular artificial ageing procedure (Esmaeili and Lloyd, 2005). The volume fraction of precipitates and the mean radius of precipitates are corrected for the start of artificial ageing as well. Additionally, Du et al. modified the modelling framework and extended the applicability of the model to over-aged materials (Du et al., 2017). The proposed model takes account of the coexistence of precipitates with different stoichiometry and predicts the precipitation kinetics of these mixed precipitates during prolonged artificial ageing. Myhr and Grong made great contributions on the development of the strength model for material undergoing non-isothermal heat treatment (Myhr et al., 2001; Myhr and Grong, 2000). With minor corrections in the expression of nucleation rate, the extended model can be further applied to predict strength evolution during post-form welding process (Myhr et al., 2004). In real manufacturing processes, it is insufficient to only consider the heat treatment conditions of the workpiece as the dislocations induced via plastic deformation have a vital influence on the ageing response. The effect of cold-working operations on the subsequent artificial ageing has also been modelled by changing the nucleation rate (Myhr et al., 2015, 2010).

2.4 Summary

One typical hot stamping technology (HFQ®) as well as a novel Fast light Alloys Stamping technology (FAST) were reviewed. Among the reviewed technologies, the FAST exhibits a great potential to boost mass production of complex-shaped components from high strength 6xxx series Al-Mg-Si alloys in the automotive industry. The structural panel components can be manufactured efficiently with low energy consumption as the cycle time is shortened without conducting lengthy solution heat treatment or prolonged artificial ageing.

The heat treatable Al-Mg-Si alloys normally require additional heat treatment to improve the mechanical properties through precipitation hardening. The desired microstructure of the formed parts facilitates the enhancement of the mechanical properties and it is highly dependent on the thermo-mechanical histories imposed on the material. Reviews have been carried out on the elementary precipitation hardening processes and corresponding underlying theories, which favours the establishment of the modelling framework.

On the basis of the comprehensive understanding of precipitation hardening mechanisms, various coupled microstructure and strength models were developed to predict the yield

strength of Al-Mg-Si alloys under different conditions as reviewed. It is obvious that these advanced models are competent to be applied to the pure as-quenched, naturally aged, pre-aged, non-isothermally aged and cold-deformed materials during artificial ageing. However, the above-mentioned models are currently unable to be used directly to predict the microstructure and strength of workpieces undergoing hot stamping in conjunction with artificial ageing. It is more challenging for the prediction of the FAST process as the involved ultra-fast heating, high temperature plastic deformation and rapid quenching influence the precipitation behaviour significantly. It is widely accepted that the pre-existing precipitates and dislocations generated in the complicated thermo-mechanical loadings would accelerate the precipitation kinetics and have a pronounced effect on the final peak strength. Therefore, a new modelling scheme for the unique FAST technology is crucial and highly demanded.

As desired, the present research addresses the issue by comprehensively studying the microstructure and strength evolutions during the novel process as well as establishing a mechanism-based unified post-form strength (PFS) prediction model, which consists of flow stress, quenching, artificial ageing, multi-stage artificial ageing and particle size distribution (PSD) sub-models. The detailed experimental results and the dedicated modelling framework are presented in the following chapters.

Chapter 3. Experimental details

A series of experiments including ultra-fast heating tests, uniaxial tensile tests, quenching tests, artificial ageing tests, EDXS tests, TEM observations and forming trials were conducted in the present research to investigate the microstructural evolutions and changes in mechanical properties during the Fast light Alloys Stamping Technology (FAST).

The Al-Mg-Si alloy used in the present investigation was a commercial AA6082 alloy in T4 temper. The as-received material was rolled sheet with a thickness of 1.6 mm and chemical composition as shown in Table 3.1. The material used was solute-rich as the combined weight percent of Mg and Si was greater than 1%.

Table 3.1: Chemical composition of AA6082 alloy (wt. %)

Alloy	Al	Mg	Si	Mn	Fe	Cu	Cr	Zn	Ti
AA6082	97.37	0.7	0.9	0.42	0.38	0.08	0.02	0.05	0.03

3.1 Ultra-fast heating tests

Ultra-fast heating tests were conducted to investigate the effect of ultra-fast heating on the precipitation response.

The tests were conducted on a Gleeble 3800 thermo-mechanical testing machine. The Gleeble 3800 system is an advanced thermo-mechanical simulation system capable of heating specimens at rates of more than 10000°C/s by utilising the direct resistance heating. Temperature feedback control is provided by thermocouples connected to the chamber. Quenching can be achieved by either air quenching tubes or water cooling channels, enabling different controlled cooling rates in the tests. The integrated mechanical system provides up to 10 tons of tensile force and the maximum stoke velocity of 2000 mm/s. The temperature and stroke histories are programmed in advance to precisely control the experimental routine.

This chapter is based on the paper work:

"Zhang, Q., Luan, X., Dhawan, S., Politis, D.J., Cai, Z., Wang, L., 2018. Investigating the quench sensitivity of high strength AA6082 aluminium alloy during the new FAST forming process. IOP Conf. Ser. Mater. Sci. Eng. 418, 12028"

"Zhang, Q., Dhawan, S., Luan, X., Du, Q., Liu, J., Wang, L., 2019. Investigation and Constitutive Modelling of High Strength 6xxx Series Aluminium Alloy: Precipitation Hardening Responses to FAST (Fast Light Alloys Stamping Technology) and Artificial Ageing. Mater. Sci. Forum. 941, 814–820."

Axisymmetric dumb-bell shaped specimens were machined from the sheet alloy by laser-cutter. The geometry of the specimens is shown in Figure 3.1. Three holes were drilled on each side for accurate positioning of the specimens.

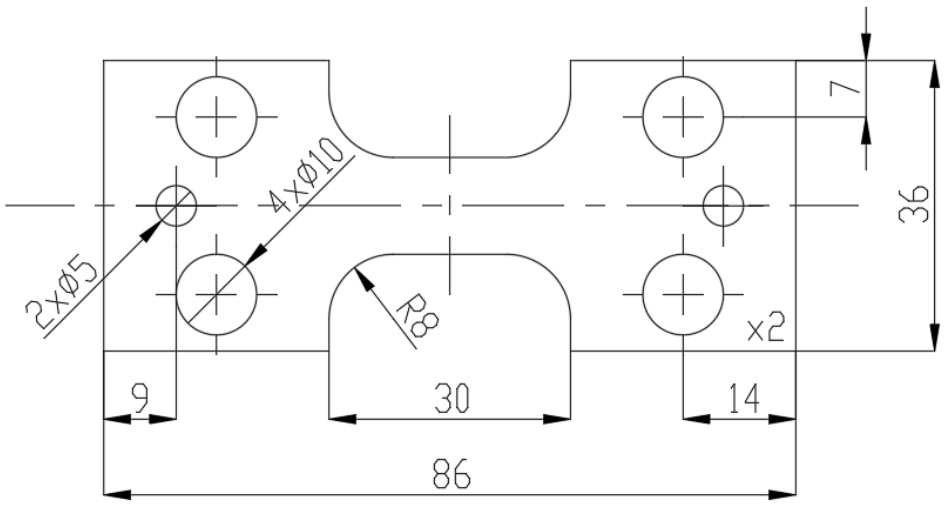

Figure 3.1: The geometry of the specimen for uniaxial tensile test

During the tests, 300, 350 and 450°C were selected as the target heating temperatures to represent the most common stamping temperatures. The specimen was fixed in the testing chamber with a pair of K-type thermocouples spot welded at the centre, and heated to a target temperature at a rate of 50°C/s. According to the results of preliminary tests, it is found that the ultra-fast heating influences the strength and precipitation response of Al-Mg-Si alloys profoundly. The FAST is sensitive to the material utilised and the minimum heating rate required for 6xxx series aluminium alloys is 50°C/s (Luan, 2019), over which no obvious difference in mechanical properties can be observed. Therefore, this rate is selected consistently in the current research. Once reaching the target temperature, water quenching was immediately triggered to cool the specimen rapidly. The control mode during the tests was set as force control to allow the specimen to expand freely with increasing temperature, otherwise a compression force would be induced and hence lead to unexpected induced dislocations. The cooled specimens were subsequently artificially aged to avoid natural ageing with the aim of restoring the material properties to full strength.

3.2 Uniaxial tensile tests

Uniaxial tensile tests were carried out to characterise the viscoplastic behaviours of Al-Mg-Si alloys in T4 temper at elevated temperatures.

Tensile test guidelines were created based on the analysis of the FAST simulation database that includes evolutions of temperature, strain and strain rate of each element at each simulation stage for different components. The test boundaries and specific values of strain rate and temperature as well as the pre-strain level were determined through the analysis of database. The temperature and strain rate distribution for AA6082 formed under FAST conditions is shown in Figure 3.2, where horizontal axes represent the strain rate and temperature and the vertical axis represents the percentage of the elements at the corresponding strain rate and temperature condition.

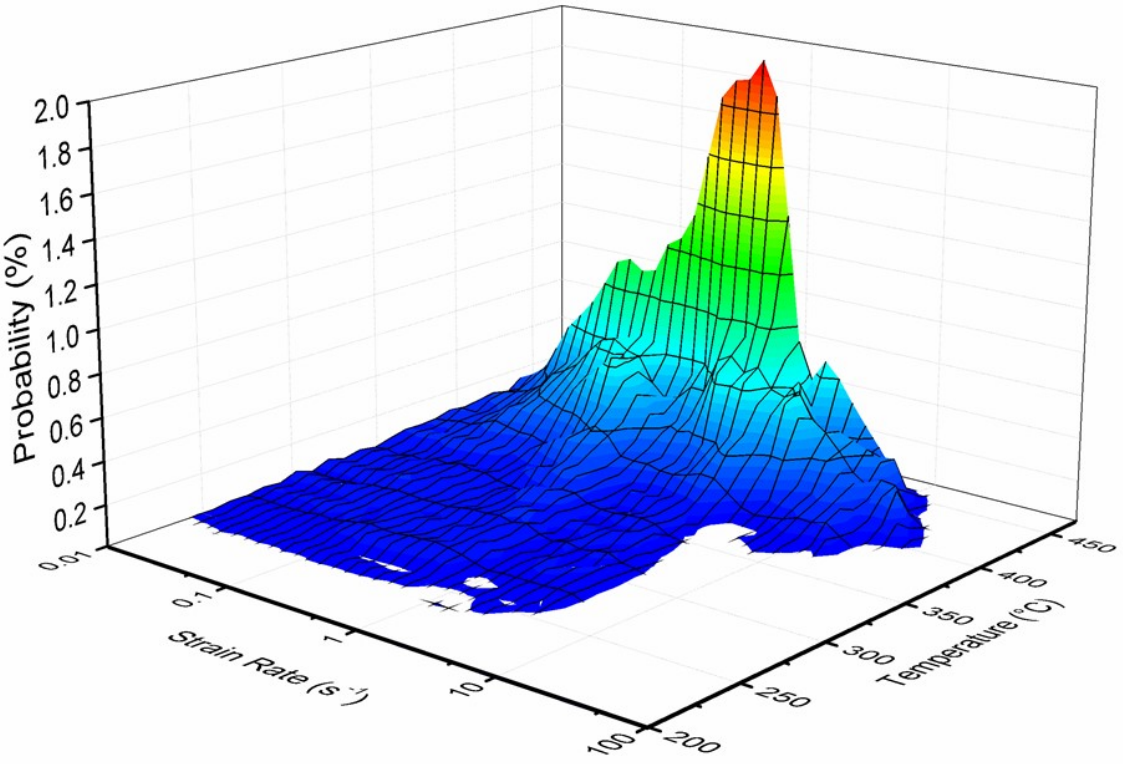

Figure 3.2: Temperature and strain rate distribution for AA6082 formed under FAST conditions (Wang et al., 2016)

The peak of the distribution is shown with red colour and indicates the most frequent occurrence condition. It is found that elements deformed between 400 and 450°C cover the

largest share of test temperatures with a probability of 66%. The strain rate distribution exhibits a normal distribution, showing that strain rates of 0.01-5 s^{-1} are most commonly used with the percentage greater than 94% (Wang et al., 2016). With this insight into parameter distribution, upper and lower boundaries were set to encompass the greatest probability of test conditions. The detailed conditions of the tensile tests are specified in Table 3.2 below. It is worth mentioning that room temperature test was also performed as the control group.

Table 3.2: Test matrix for uniaxial tensile tests

Temperature (°C) / Strain rate (s^{-1})	25	350	400	450	500
0.01				√	
0.1				√	
1	√	√	√	√	√
5				√	

The effect of strain rate was investigated at 450°C that is a common temperature for stamping of 6xxx aluminium alloys and the temperature effect on the viscoplastic response was studied by using a constant strain rate of 1 s^{-1} that is the strain rate of greatest probability used for forming process.

Due to the limit of the specimen size, C gauge data recording of Gleeble could not be performed. Therefore, digital image correlation (DIC) was utilised to precisely analyse the stress-strain response during tensile tests. DIC is a non-contact technique to measure strain and displacement during deformation processes. A high-speed camera and dedicated software are used to track the movement of points on the painted surface of the specimen. A clear speckle pattern painted on the surface is required to produce a high correlation with minimal noise, which should consist of the following characteristics: (i) High contrast between the background and the dots; (ii) Equal amount of contrast colours on the surface; (iii) Consistent speckle sizes and (iv) Uniform distribution of the painted dots. The schematic diagram is shown in Figure 3.3.

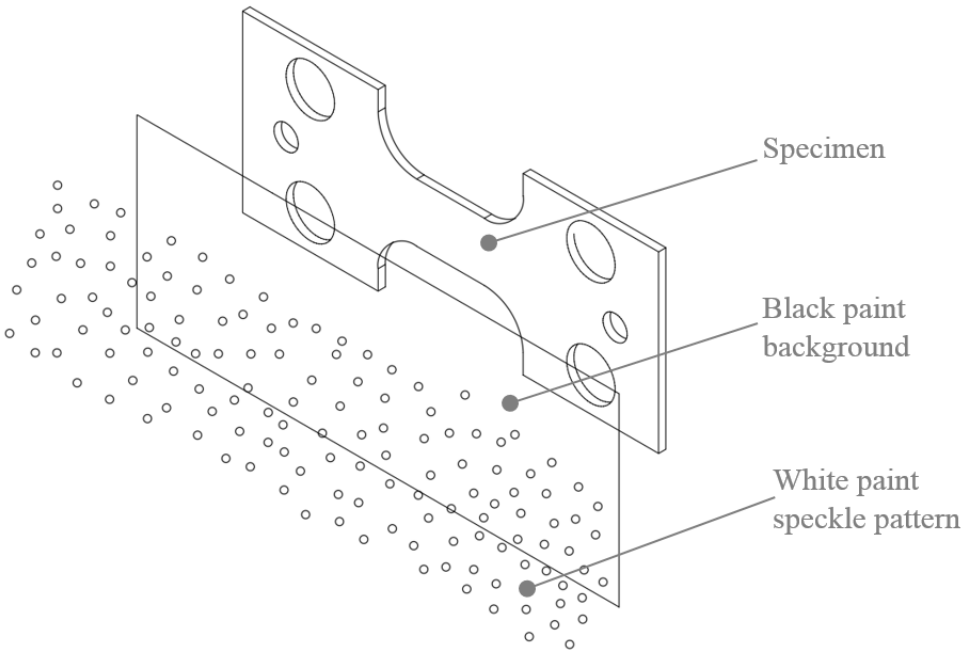

Figure 3.3: Schematic diagram of the painting procedures

The dumb-bell shaped specimen was carefully prepared before the test by polishing the surface with sand paper at first to remove the oxide layer. The surface of the central region of the specimen was spray painted with black paint. White spray paint was subsequently used to paint a contrasting speckle pattern on top of the black paint. The painting process was performed in a BenchVent recirculating fume cabinet that filters, absorbs and dilutes the solvent odours, vastly reducing the potential exposure to the hazardous substances.

Figure 3.4: BenchVent recirculatory spray booth ("D & T General Spraybooths," 2019)

A pair of K-type thermocouples were welded at the centre of the specimen and connected to the testing chamber of Gleeble 3800 to monitor the temperature evolution of the specimen. The specimen was then fixed between the grips and clamped between jaws in the chamber. The uniform temperature distribution across the deformation zone was guaranteed by using the stainless steel grips. Air cooling tubes were set up around the specimen to achieve sufficient quenching rate after the stretching process.

(a)

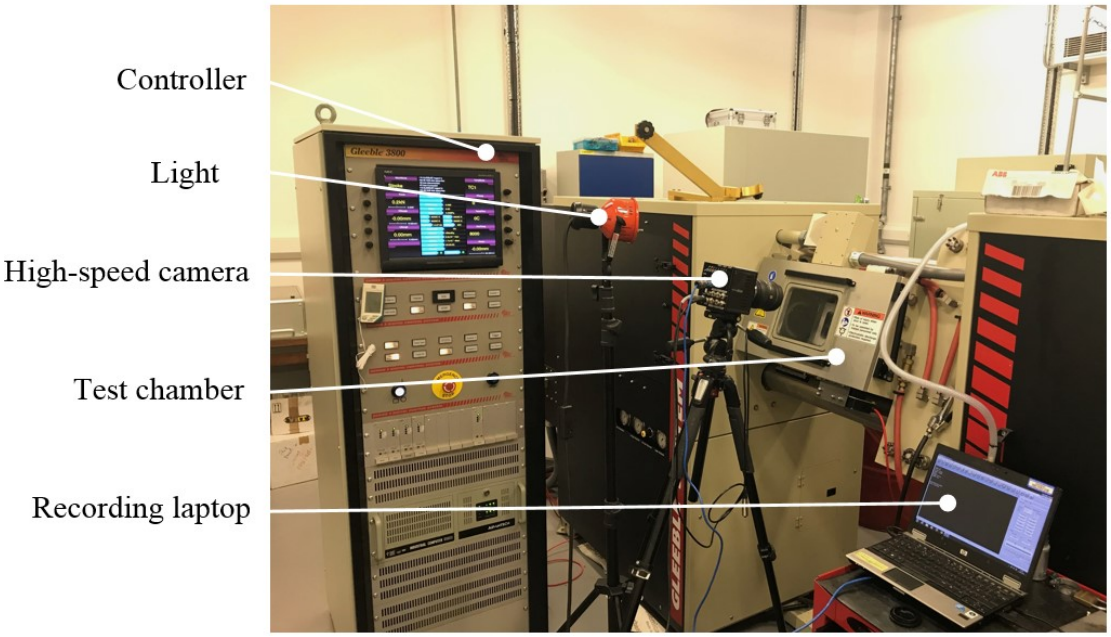

(b)

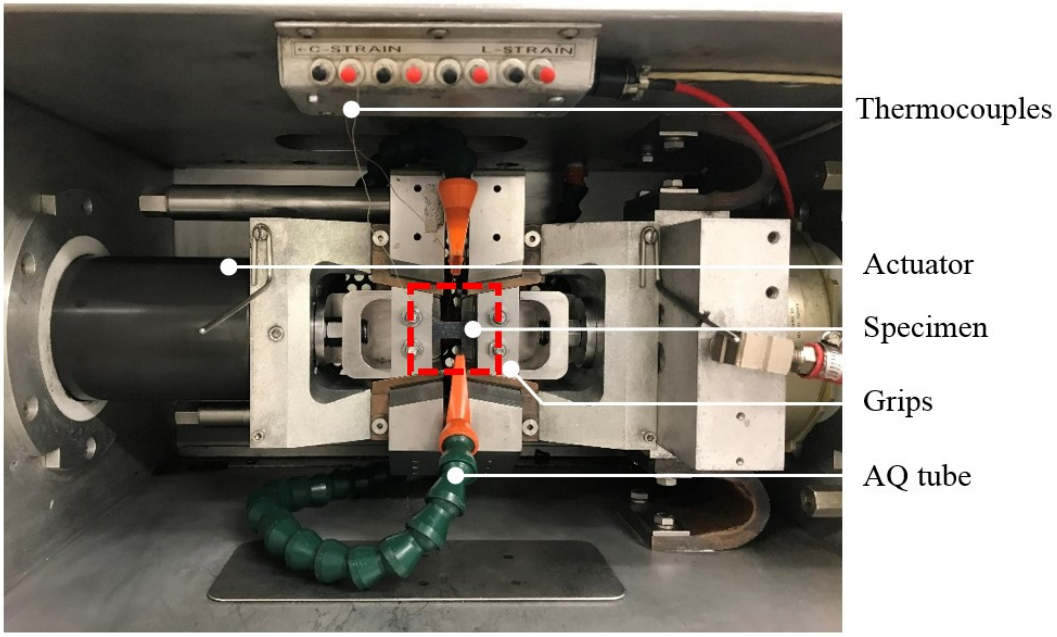

Figure 3.5: Gleeble 3800 thermo-mechanical system (a) setup of the DIC and (b) setup of the specimen with air quenching tubes

During the test, the specimen was heated to a temperature 25°C lower than the target temperature at a rapid heating rate (50°C/s) and subsequently slowly heated to the target temperature (5°C/s). The temperature overshoot was avoided and no fluctuation or overheating would occur. Force control was adopted in the heating process with the force set to zero once the target test temperature was reached. This enables the actuator to automatically compensate for thermal expansion caused by the temperature increase of the specimen. The Gleeble 3800 system was subsequently switched to stroke control, enabling accurate control of the displacement of the grips and hence the strain rate. The initial gauge length of the specimen was 8mm after calibration. The displacement at each time step during deformation was computed by multiplying the transient gauge length with the constant strain rate. Once the control mode was switched to stroke control, the operator pulled the trigger of the high-speed camera that is capable of recording up to 160,000 images per second. The images taken during the test were transferred to the laptop for further analysis. Air quenching was applied immediately when the specimen was stretched to failure.

The stress-strain curves of each testing condition were obtained by post-processing of the Gleeble data and DIC analysis was completed by using the commercial software 'Aramis'. The force applied to stretch the specimen was recorded by Gleeble 3800. The stress σ_y was calculated accordingly via dividing the force by the cross section area S of the uniform deformation region.

$$\sigma_y = F/S \tag{3-1}$$

However, the recorded stroke could not be used directly as it represented the deformation of the entire specimen rather than the uniform deformation region. Alternatively, 'Aramis' was utilised, with the help of the images, to compute displacement of the uniform deformation region and hence the strain during the tests. The stored images were first imported into 'Aramis'. The scale of the specimen in the images was modified to represent the true size and the analysed region was defined manually. The software computed the strain throughout all stages automatically and generated a report with the results. Figure 3.6 illustrates the deformed specimen and the strain analysis of the specimen stretched to 10% strain at 1 s^{-1}.

(a)

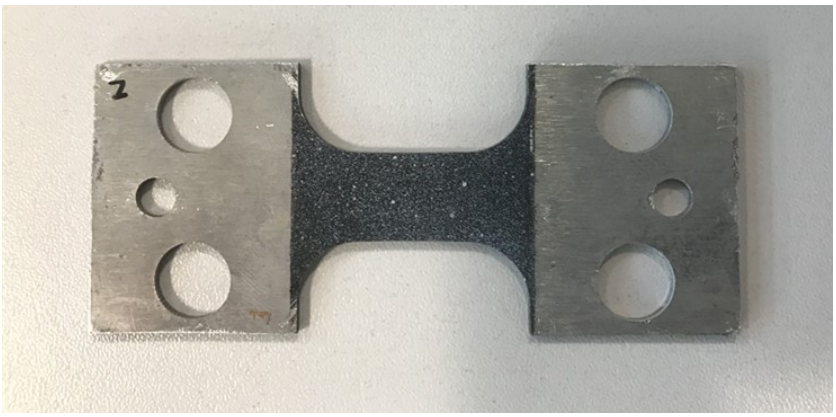

(b)

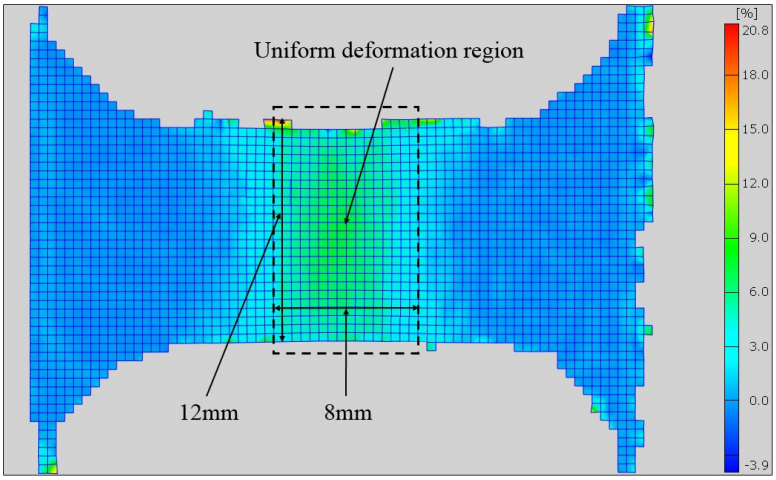

Figure 3.6: (a) Painted dumb-bell shaped specimen and (b) strain analysis of the specimen in Aramis

3.3 Pre-straining uniaxial tensile tests

To investigate the effect of dislocations induced during high-temperature plastic deformation on the subsequent precipitation response, pre-strained specimens were produced by using the Gleeble 3800 system and DIC. The data analysis approach was also employed to determine the deformation conditions for the preparation of the pre-strained specimens. Consistently, 450°C was selected as the target temperature and strain rates of 0.01, 0.1 and 1 s^{-1} were selected to cover the largest percentage of the elements during the hot stamping process. It was found that the strain of 98% elements was smaller than 0.3 therefore the upper limit of the pre-strained specimen was set as 30%. The test matrix of the pre-strained specimens is outlined in Table 3.3.

Table 3.3: Test matrix for pre-straining uniaxial tensile tests

Strain (%) / Strain rate (s^{-1})	10	20	30
0.01	√		
0.1	√		
1	√	√	√

In order to obtain thermo-mechanical histories of the specimens similar to those of the real FAST process, the specimens were heated to 450°C at an ultra-fast rate of 50°C/s and immediately isothermally stretched to pre-defined strain levels (10%, 20% and 30%) with strain rates ranging from 0.01 to 1 s^{-1}. Water quenching was used to rapidly cool the specimens to room temperature with the purpose of maintaining the microstructure without the formation of undesired precipitates. The spray direction of the cooling water was adjusted in advance to ensure the deformation zone (centre of the specimen) can be quenched efficiently. Figure 3.7 shows the setup of the specimen in the Gleeble testing chamber with water quenching channels assembled.

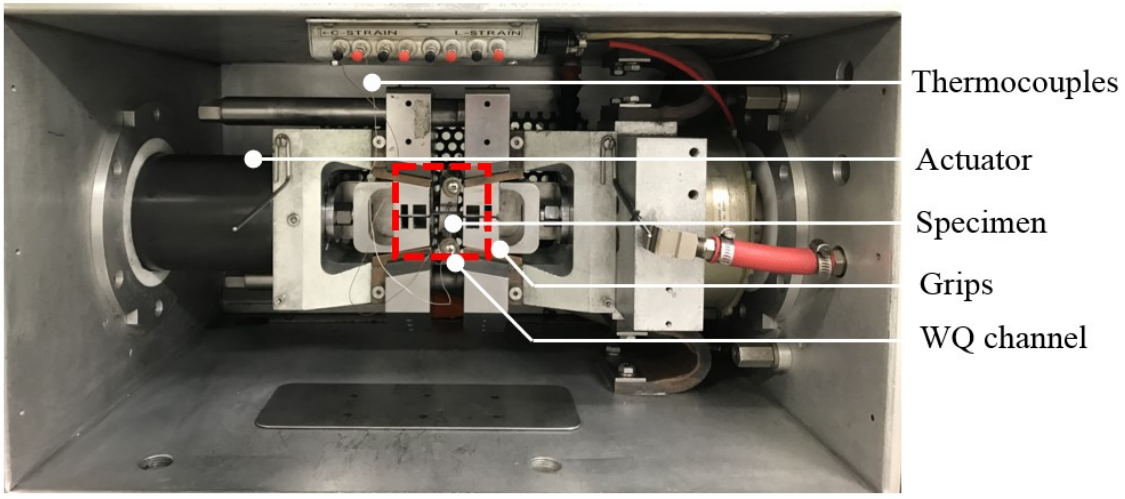

Figure 3.7: Setup of the specimen in the testing chamber with water quenching channels

DIC was utilised to post-process the strain evolution during deformation. It is worth mentioning that the control program of Gleeble system was calibrated with the strain-displacement report generated by 'Aramis', the stroke of the actuator was correlated with the true strain detected by the high-speed camera to enable accurate recording of the strain induced to the specimen.

3.4 Quenching tests

In order to identify the formation of pre-existing precipitates and study their effect on the precipitation response during artificial ageing processes, quenching tests were performed in Gleeble 3800. In this series of tests, no deformation was induced on the specimens to exclude the effect of dislocations.

The rate applied to quench the specimen from elevated stamping temperature to room temperature is crucial to the material properties. According to the CCT diagram for aluminium alloys, insufficient quenching rate would cause the formation of undesired precipitates that lower the precipitation response in the ageing processes.

In the quenching test, the specimen was heated to 450°C at a rate of 50°C/s to maintain consistency between the tests. Accurate temperature feedback control was realised by welding a pair of thermocouples at the specimen centre. The non-deformed specimen was then quenched to ambient temperature by either water (WQ) or air (AQ) with varying cooling rates. Water quenching rate in the test was greater than 1000°C/s where the precipitation response was suppressed completely, and hence the water quenched specimen was the control group. It is difficult to maintain a constant air cooling rate during the whole quenching process in the Gleeble 3800 system. The temperature usually decreases exponentially against cooling time with higher cooling rate in the early stage and slowing down gradually. It is reported that the formation of precipitates is highly sensitive at the temperature range between 450 and 200°C. Therefore, an average quenching rate ranging from 180 to 310°C/s in the critical temperature range was used to perform the tests.

3.5 Artificial ageing tests

A series of artificial ageing tests, including one-stage and multi-stage ageing, were performed to characterise the precipitation kinetics of Al-Mg-Si alloys, and investigate the effect of ultra-fast heating, pre-straining and quenching on the artificial ageing response. The tests were split into two main groups. The first group of tests were conducted to study the strength evolution of the specimens in supersaturated solid solution state during artificial ageing at different temperatures. In the other group of tests, ultra-fast heated, pre-strained and

sufficient/insufficient quenched specimens were produced by previous tests and artificially aged in order to explore the potential effect on the precipitation behaviour.

(a) (b)

Figure 3.8: Facilities used in the artificial ageing tests (a) solution heat treatment furnace ("Zwick/ZHU 187.5 Universal hardness tester," 2019) and (b) environmental chamber ("Instron environment chamber," 2019)

The Lenton furnace (temperature range: 0-900°C) and the Instron environment chamber (temperature range: 0-250°C) were used to carry out solution heat treatment and artificial ageing, respectively. The furnaces were set to the target temperatures with two identical steel blocks (250x80x15 mm) placed inside. A pair of K-type thermocouples with one end fixed to a piece of specimen was held between the steel blocks to monitor the temperature. It is required to wait for a certain period of time (dependent on the target temperature) until the temperature shown in the thermal meter reached the target elevated temperature and remained stable. The specimens were placed uniformly between the steel blocks during the heat treatments. As the specific heat capacity of steel is larger than air, the usage of blocks would minimise severe temperature fluctuations caused by the air flow when opening and closing the doors of the furnace. Furthermore, the specimens were held between the blocks in a sandwich structure, which ensures both sides of the specimen are in good contact with the blocks. Therefore, a high

heating rate was acquired and the temperature of the specimens was stable and uniform during the test.

The testing conditions of both groups of artificial ageing tests are listed in the table below:

Table 3.4: Testing conditions for the specimens undergoing artificial ageing

	UF heating	Pre-strain	Quenching	Single-stage AA	Two-stage AA
UFH tests	300, 350, 450°C	/	WQ	180°C	/
PS tests	450°C	10, 20, 30%; 0.01, 0.1 $1s^{-1}$	WQ	180°C	/
Q tests	450°C	/	WQ/AQ	180°C	/
AA tests	/	/	/	180, 190, 220, 240°C	/
MAA tests	/	/	/	/	220 + 190°C

In the first group of pure artificial ageing tests, the specimens were manufactured from the sheet blank by laser-cutter with the consistent dimensions of 40x40x1.6 mm. The size was designed relatively small to avoid distortion that can possibly be induced during rapid quenching. The test specimens were positioned into the Lenton furnace for solution heat treatment. The SHT temperature was 535°C and the soaking time was 30 minutes. Once SHT was completed, all the specimens in the chamber were removed quickly and dropped into the water tank for quenching to obtain the supersaturated solid solution state. Either one-stage artificial ageing or two-stage artificial ageing was performed immediately to avoid the effect of room temperature storage. In the one-stage artificial ageing tests, the specimens were soaked at 180, 190, 220 and 240°C until obvious over-ageing phenomenon could be detected. The required ageing time was reduced with increasing ageing temperature. In order to capture the full strength evolutions, the ageing time at 180, 190, 220 and 240°C was 16, 8, 3.5 and 1 hours, respectively. In the two-stage artificial ageing tests, the material was held at 220°C for 3-6 minutes in the first stage and then followed by second-stage ageing at 190°C for 20, 40, 120 and 240 minutes. In the present work, hardness was used to indicate the strength of all

specimens. The resulting specimen hardness was measured with a Zwick Roell hardness tester to parametrize the performance of the specimens in this thesis. All hardness measurements were made by using a 30 N (HV3) load and 10 seconds dwell time at room temperature. For each specimen, at least three indentations were performed to obtain an average value of hardness.

Figure 3.9: Hardness tester Zwick Roell ZHU ("Zwick/ZHU 187.5 Universal hardness tester," 2019)

In the other group of coupled pre-treatment and artificial ageing tests, the ultra-fast heated, pre-strained, air- and water-quenched specimens produced from the preceding tests were placed in the Instron environment chamber and held between the steel blocks for isothermal artificial ageing at 180°C, until the full strength evolution of each specimen was achieved. The artificially aged dumb-bell shaped specimens were removed from the environment chamber and polished by using sand paper in order to remove the oxide layer caused by the exposure to elevated temperatures. Hardness measurements were then performed on the uniform deformation region of each specimen. This procedure was repeated for the pure artificial ageing tests to ensure consistency between the results.

3.6 Transmission electron microscopy tests

Microstructure investigations were conducted on an FEI Tecnai F20 transmission electron microscope (TEM) operating at 200 kV accelerating voltage. Small samples were cut from the square specimens for pure artificial ageing tests and the uniform deformation region of the dumb-bell shaped specimens operated in Gleeble. After electropolishing, the disc-shaped samples with a diameter of 3mm were punched from the ground slice. Ion thinning was conducted by Gatan 691 precision ion polishing system. For each TEM sample, more than 50 images in different scales (1 – 200 nm) were taken to measure the radius, number density and volume fraction of precipitates. All images were acquired along the preferential ⟨100⟩ Al-zone axis, where the distribution of precipitates can be readily observed.

(a) (b)

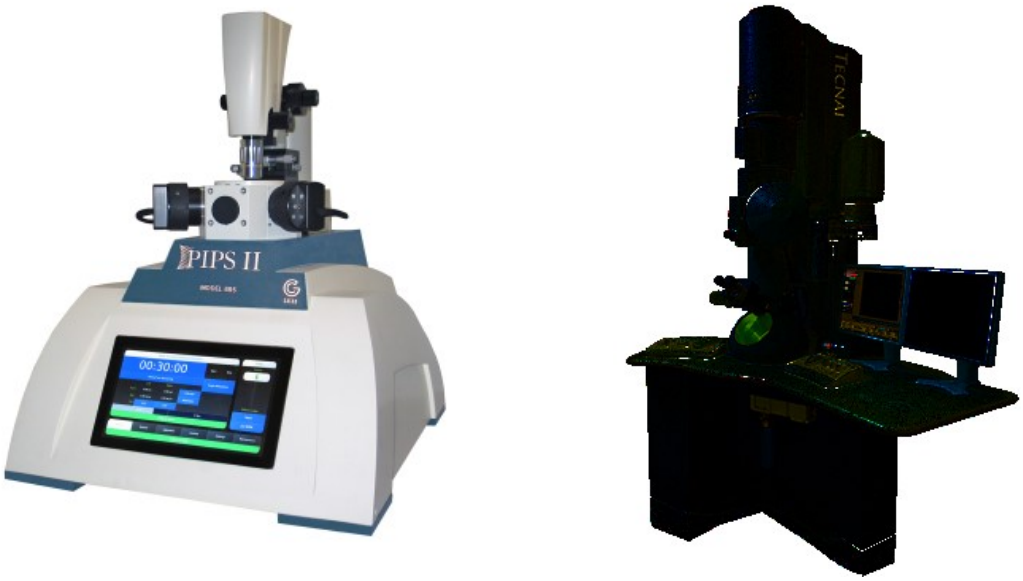

Figure 3.10: Facilities used for TEM observations (a) ion polishing system ("PIPS II System," 2019) and (b) transmission electron microscopy ("FEI Tecnai F20," 2019)

3.7 Uni-form forming tests

Forming trials of a U-shaped component were conducted in a dedicatedly developed pilot production line – 'Uni-Form' with forming parameters accurately controlled, to independently validate the capability of the developed post-form strength prediction model. The FAST process involving ultra-fast heating, hot stamping, rapid quenching and artificial ageing can be

simulated in lab scale through this testing facility. As can be seen in Figure 3.11, the modular designed 'Uni-Form' is comprised of four sub-systems: furnace, forming tool, incubation chamber and conveyor. Each sub-system can be positioned in the allocated space on the frame and can be removed and replaced by other modules for different forming processes, cycles or geometries. The furnace has two conductive platen heaters with heating cartridges embedded. 'Uni-Form' is capable of providing a maximum heating rate up to 200°C/s and maximum forming temperature of 650°C. The temperature deviation between the centre and the edge of the heater is less than 5% enabling a good temperature homogeneity of the specimen during heating. 'Uni-Form' is mounted on a 100-ton hydraulic press with a gas spring cushion positioned on the machine bed. The adjustable stamping force is provided by the pressure charged to the gas spring (maximum 40 bar). The incubation chamber is designed to simulate pre-form and post-form heat treatment at elevated temperatures. The chamber is filled with a thermal insulation material Firefly Millborad F700 with an extremely low thermal conductivity of 0.1 W/m·K, to minimise the heat loss from the specimen. A tubular air heater is installed at the base of the chamber to maintain the artificial ageing temperature. The polymer belts of the conveyor system offer a high degree of positional precision with an accuracy of at least ±0.5mm and good repeatability by maintaining constant contact with driving gears and reducing backlash greatly. The fully automated 'Uni-Form' system incorporates a PIC 4331 microcontroller programmed in C language, which coordinates different sub-systems and controls the forming processes. The dedicated processing windows applied in the 'Uni-Form' system can also be specified and modified remotely through the cloud based FEA platform that will be further discussed in Chapter 6.

(a)

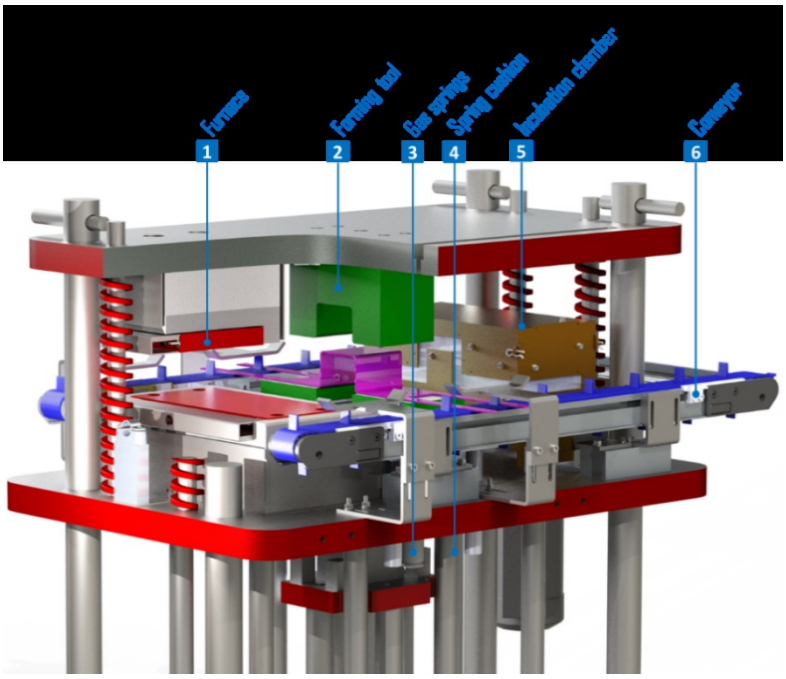
Furnace
Forming tool
Gas springs
Spring cushion
Isolation chamber
Conveyor
1
2
3
4
5
6

(b)

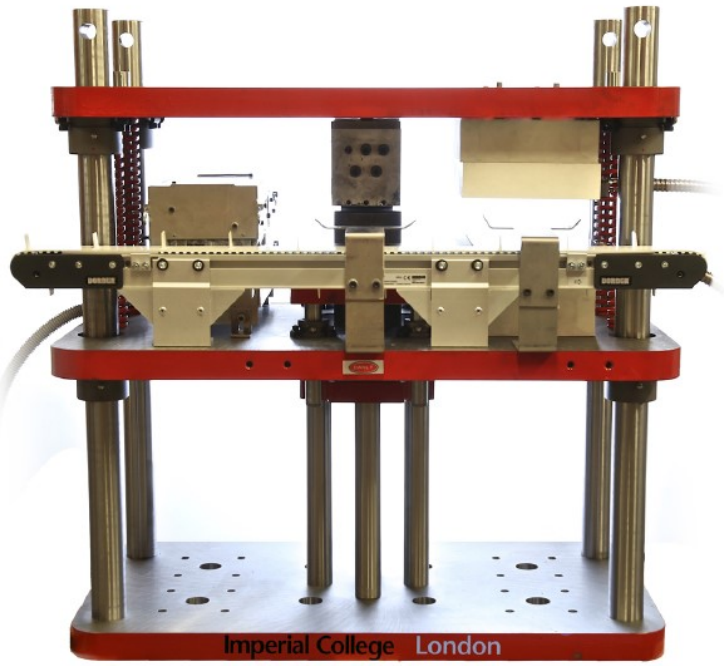
Imperial College London

(c)

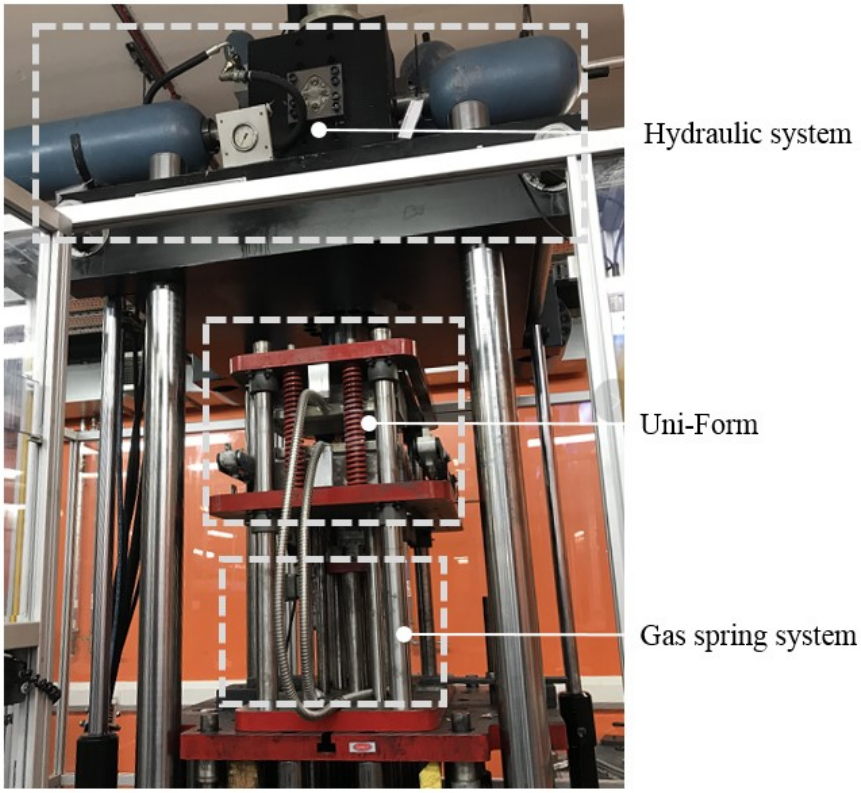

Figure 3.11: (a) 3D schematic diagram of the 'Uni-Form' production line, (b) The 'Uni-Form' production line and (c) The installation of the 'Uni-Form' production line on the press

The processing windows were determined and initialised before the start of the tests. In the forming trials, the workpiece with the geometry shown in Figure 3.12 was located on the polymer conveyor at first. Once the controller was activated, the conveyor belts would transfer the blank to the furnace. The upper platen heater moved down towards the lower one and formed a tight contact while the workpiece was clamped between the platens for a few seconds until heated to 450°C. The upper heater was then released and the workpiece was transferred to the forming tools. After the stamping process, the workpiece was held in the forming tools for in-die quenching until the temperature reached 180°C. Then the upper platform released the formed component again and it was transferred into the incubation chamber for artificial ageing at 180°C. Finally, hardness measurements were conducted at different regions of the formed components.

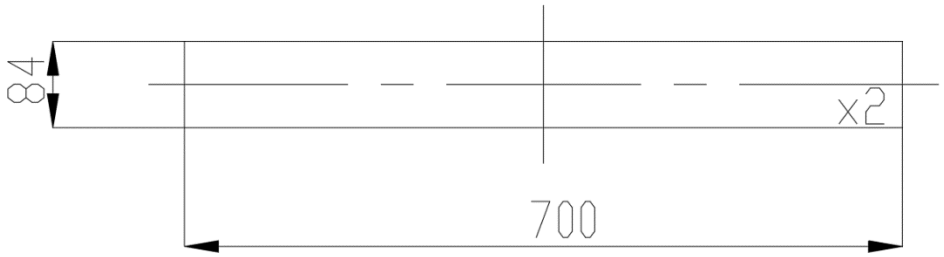

Figure 3.12: The geometry of the workpiece in the forming trails

3.8 Summary

A series of ultra-fast heating tests, uniaxial tensile tests, pre-straining uniaxial tensile tests, quenching tests, artificial ageing tests and TEM observations were conducted to simulate the FAST process and study the microstructural evolution and changes of mechanical properties during the whole FAST process. The in-depth analysis of the experimental results would assist in the development of the post-form strength prediction (PFS) model. The forming trials of U-shaped components were performed on the pilot production line 'Uni-Form' to validate the capacity and accuracy of the PFS model.

Chapter 4. Microstructure and strength evolutions of 6xxx aluminium alloys during the FAST process

This chapter discusses the results of the experimental work outlined in the previous chapter. Results of ultra-fast heating tests, uniaxial tensile tests, pre-straining uniaxial tensile tests, quenching tests, artificial ageing tests and TEM observations are presented. The microstructure and strength evolutions are analysed and used to develop and calibrate the post-form strength prediction model.

4.1 Precipitation behaviour during ultra-fast heating

Ultra-fast heating tests were conducted under a rate of 50°C/s to the target temperatures of 300, 350 and 450°C, followed by water quenching and artificial ageing at 180°C for a range of times. The results of the hardness evolution with target temperature against ageing time are shown in Table 4.1 and Figure 4.1. The hardness curve of the as-quenched specimen during 180°C is also plotted as a reference. The microstructures of the specimens undergoing ultra-fast heating and water quenching are shown in the TEM images in Figure 4.2.

Table 4.1: Hardness values of the specimens after the 180°C artificial ageing with different target heating temperatures

Target heating temperature / °C	Hardness / HV						
	0h AA	0.67h AA	1.33h AA	3.5h AA	6.5h AA	10.75h AA	15.75h AA
300	60.9	111.9	118.6	**119.9**	118.6	116.1	108.8
350	59.5	97.8	109.4	**112.4**	110.6	107.1	102.8
450	56.9	106.0	116.5	119.6	**121.8**	118.9	112.3

This chapter is based on the paper work:

"Zhang, Q., Luan, X., Dhawan, S., Politis, D.J., Du, Q., Fu, M.W., Wang, K., Gharbi, M.M., Wang, L., 2019. Development of the post-form strength prediction model for a high-strength 6xxx aluminium alloy with pre-existing precipitates and residual dislocations. Int. J. Plast. 119, 230–248."

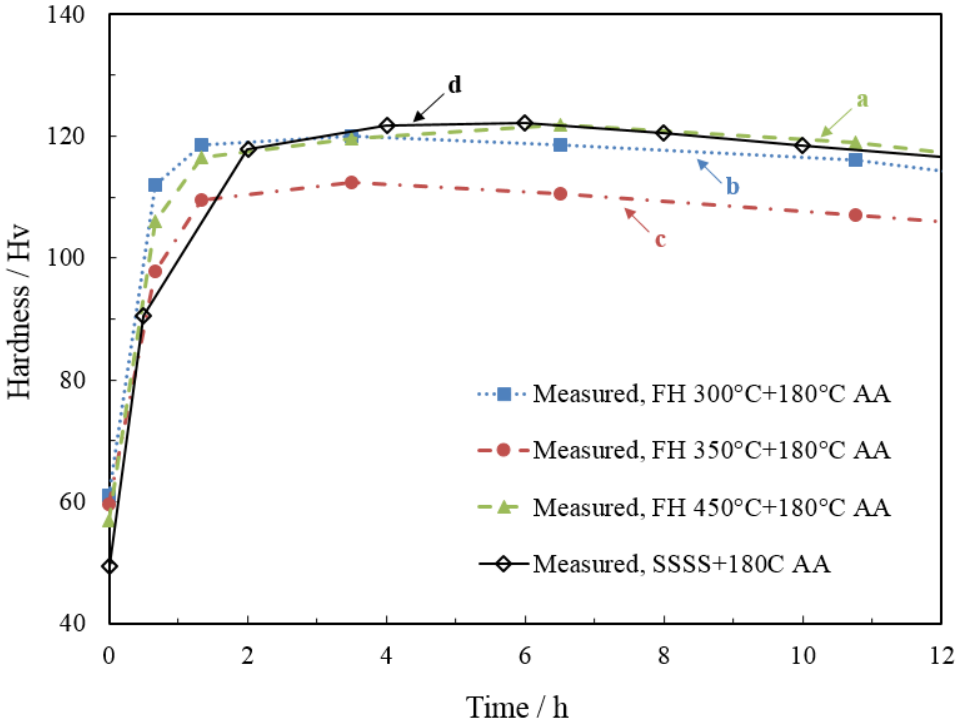

Figure 4.1: Hardness evolutions of the ultra-fast heated specimens during artificial ageing at 180°C

As can be seen, after ultra-fast heating and water quenching (time = 0 hours), the hardness values for specimens with different target heating temperatures are 60.9 HV, 59.5 HV and 56.9 HV respectively. Comparatively, these are lower than the hardness of the initial T4 temper (80.0 HV), but greater than the hardness of the material in its supersaturated solid solution state, approximately 48 HV. The hardness of all three ultra-fast heated specimens increases rapidly during the early stage of artificial ageing at 180°C where the hardness increases from approximately 60 HV to more than 105 HV within the first 1.5 hours. It also indicates that the peak hardness occurs after approximately 6 hours ageing for the specimen that was rapidly heated to 450°C while it takes 3.5 hours to reach peak condition when heated to 300 and 350°C. Additionally, the peak hardness of curves (a) and (b) in Figure 4.1 are 121.8 HV and 119.9 HV respectively, while the peak value for the curve (c) in the figure is relatively lower (112.4 HV). The peak hardness of all the specimens after ageing can be retained to at least 92% of the T6 temper value. With further increase in ageing time, the material over-ages as can be clearly observed with the resulting hardness reduction. Apart from the initial stage, the hardness trend of the specimen heated to 450°C is very similar to that of pure ageing for the as-quenched material.

Figures 4.2. (a), (b) and (c) show the TEM scans performed on specimens after ultra-fast heating to the target temperatures of 300, 350 and 450°C, and followed by water quenching.

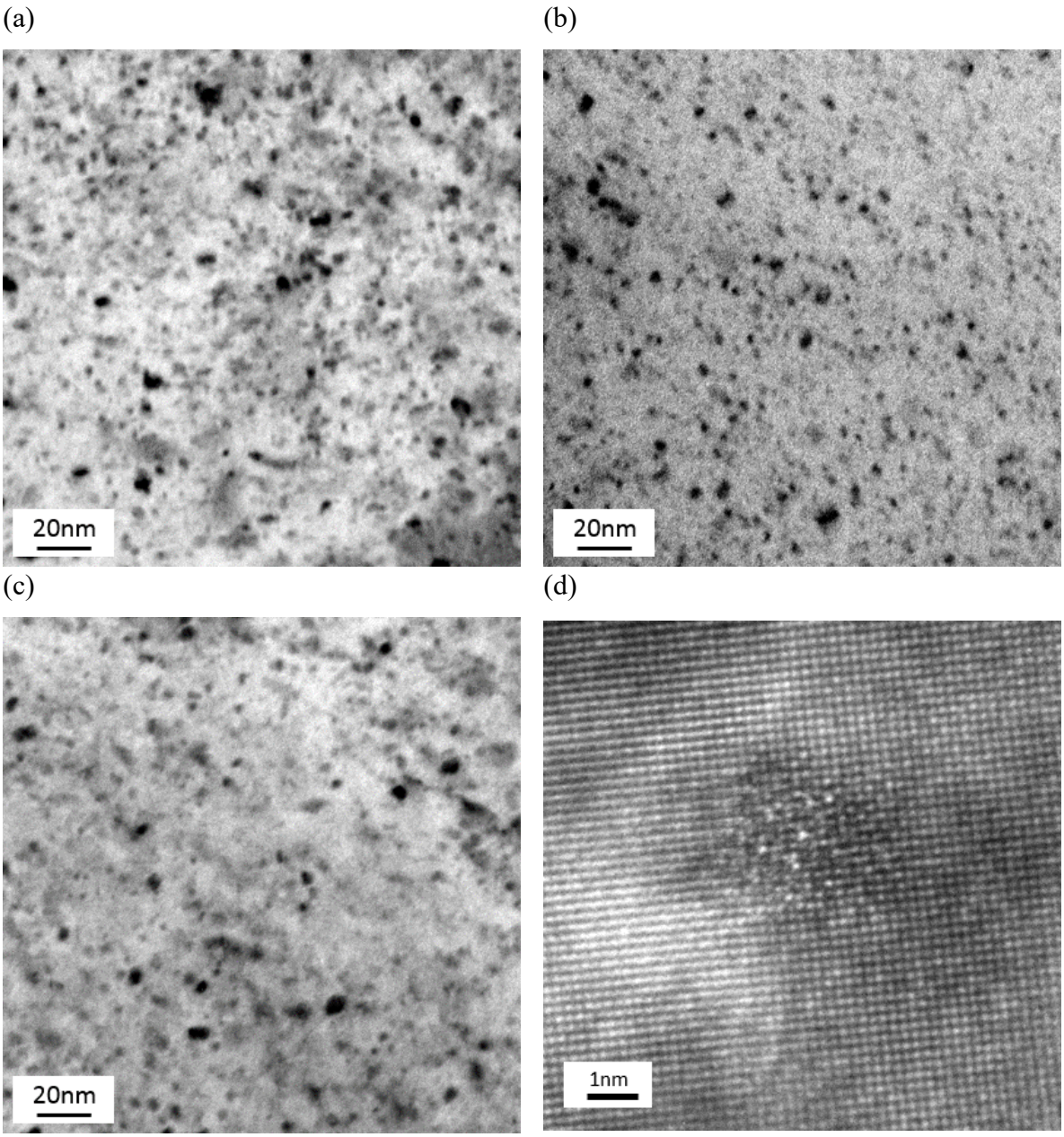

Figure 4.2: TEM bright field images of microstructures observed in the <100> Al zone axis orientation after (a) fast heating to 300°C + water quenching, (b) fast heating to 350°C + water quenching, (c) fast heating to 450°C +water quenching and (d) HR-TEM image of the pre-*β''* precipitates

Dot-like precipitates with an average radius of approximately 3.9 nm, are observed and found to be relatively finely dispersed in the aluminium matrix. The high-resolution TEM image of this spherical precipitate is demonstrated in Figure 4.2. (d). The lowest precipitate density is

found when heated to 450°C while the highest density was observed in the 350°C specimen. EDXS (Energy-dispersive X-ray spectroscopy) tests were conducted to determine the chemical composition of the observed spherical precipitates. The Mg: Si ratio lies between 1 and 1.5 by analysing the results.

The initial temper of the material is T4 with undetectable room temperature clusters. With the hardness decreasing from 80 HV to less than 60 HV, it is deduced that most of the metal-stable natural ageing clusters of the raw material are dissolved again into the matrix during the ultra-fast heating process. The observed spherical precipitates are supposed to be formed either in ultra-fast heating or water quenching. As the cooling rate of water quenching (greater than 1000°C/s) is far higher than the required critical quenching rate, the increased post-quenched hardness (> 48 HV of SSSS material) is attributed to the formation of these pre-β'' precipitates in the heating process (heated to 300, 350 and 450°C), instead of the cooling process (Milkereit et al., 2012; Zhang et al., 2018). It is well accepted that the Mg/Si ratio of pre-β'' is over 1 and their shape is almost spherical with a radius of approximately 3 nm. These precipitates are well coherent with the matrix, which is consistent with the observed precipitates above (Marioara et al., 2003). Regarding the morphology and the ratio of Mg to Si, these dot-like precipitates are identified to be pre-β'' phase. In the case of continuous fast heating to 450°C, most of the formed precipitates may have dissolved into the matrix, resulting in an infinitesimal amount remaining, which agrees with the precipitate number density observed in TEM images. This results in the initial hardness of curve (a) being the lowest of the three (56.9 HV) although it is still greater than the as-quenched value (48 HV) of the curve (d).

The growth and coarsening of precipitates occur quickly compared to the material in the SSSS state. These pre-existing pre-β'' precipitates consume solute elements and quenched-in vacancies and are readily to be transferred to the strongest needle-shaped β'' precipitates in the artificial ageing. However, nucleation sites are occupied by these pre-existing precipitates, reducing the density of precipitate formation as ageing proceeds. In the diffusion process, additional solute atoms will accumulate around these precipitates as less diffusion energy is needed. As a result, the distribution of precipitates in peak condition would be not as fine or uniform as without pre-existing precipitates, leading to a slight decrease in peak hardness. This phenomenon can be readily observed for the specimen being fast heated to 350°C, with 8% hardness loss (112.4 HV) compared to T6 temper material (122.2 HV). The hardness evolution

of curve (a) is very similar to the curve (d) as the amount of pre-*β"* precipitates in the specimen heated to 450°C is lowest and hence the minimum effect is involved.

The beneficial and detrimental effects of pre-existing precipitates on the precipitation response have been carefully investigated. In the modelling framework, the size and volume fraction of the pre-existing precipitates are specified and would be implemented in the age-hardening sub model as the initial material condition. The evolutions of these precipitates are tracked in the subsequent computation to accurately predict the overall strength.

4.2 Viscoplatic behaviour

Uniaxial tensile tests were conducted on Gleeble 3800 thermo-mechanical testing machine to investigate the viscoplatic behaviour of AA6082. Figure 4.3 shows the room temperature flow stress curve as well as high temperature flow stress curves at different strain rates and forming temperatures.

(a)

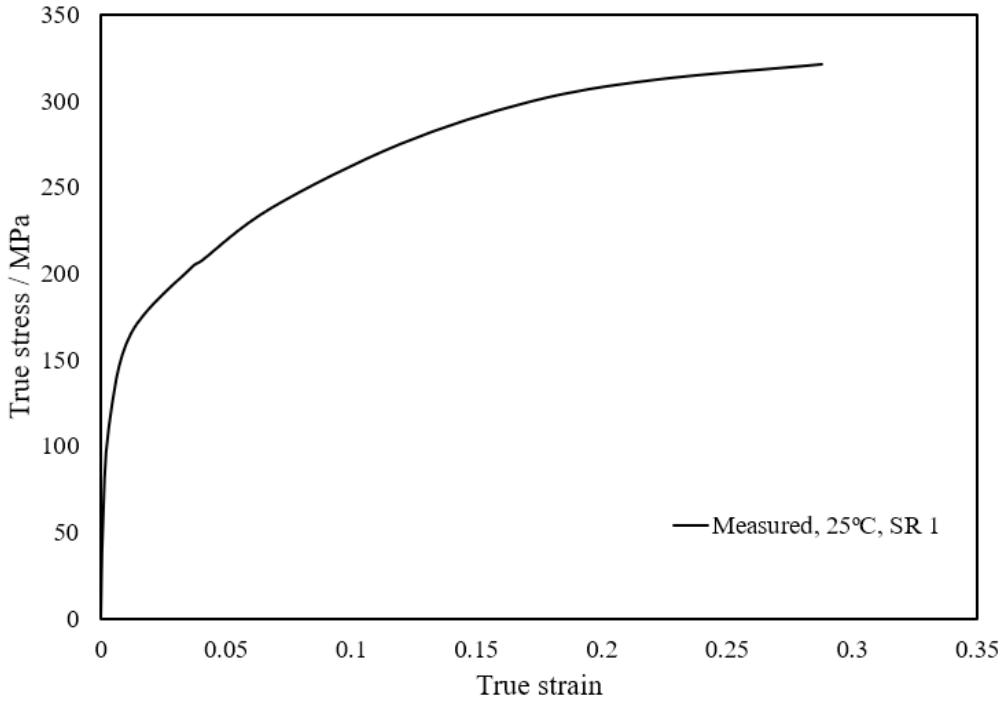

(b)

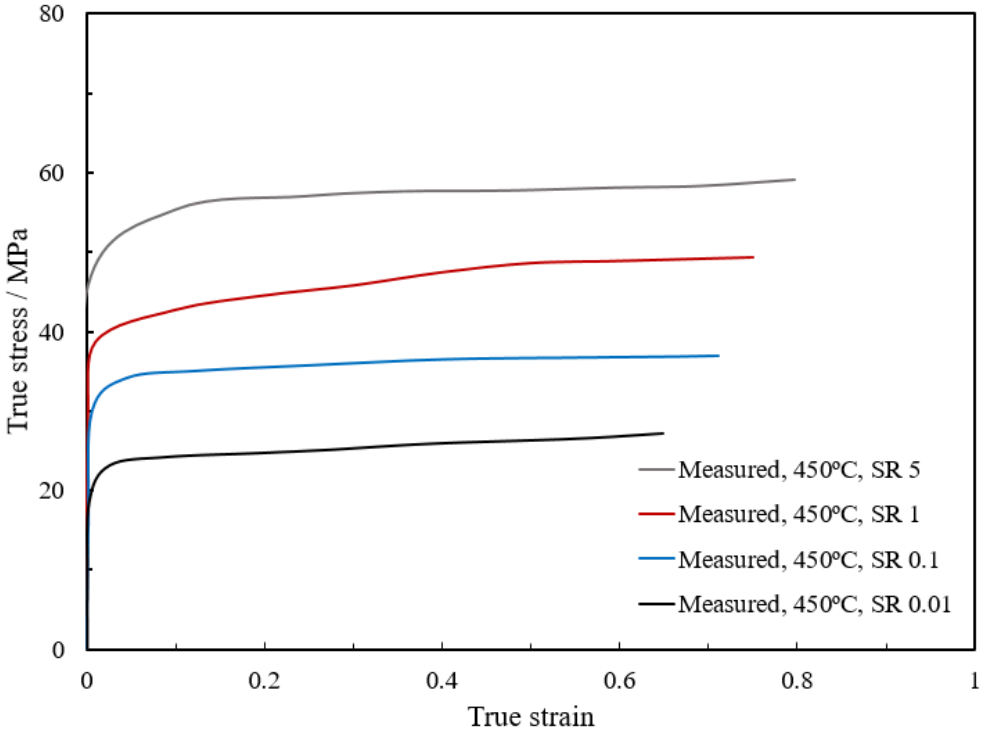

(c)

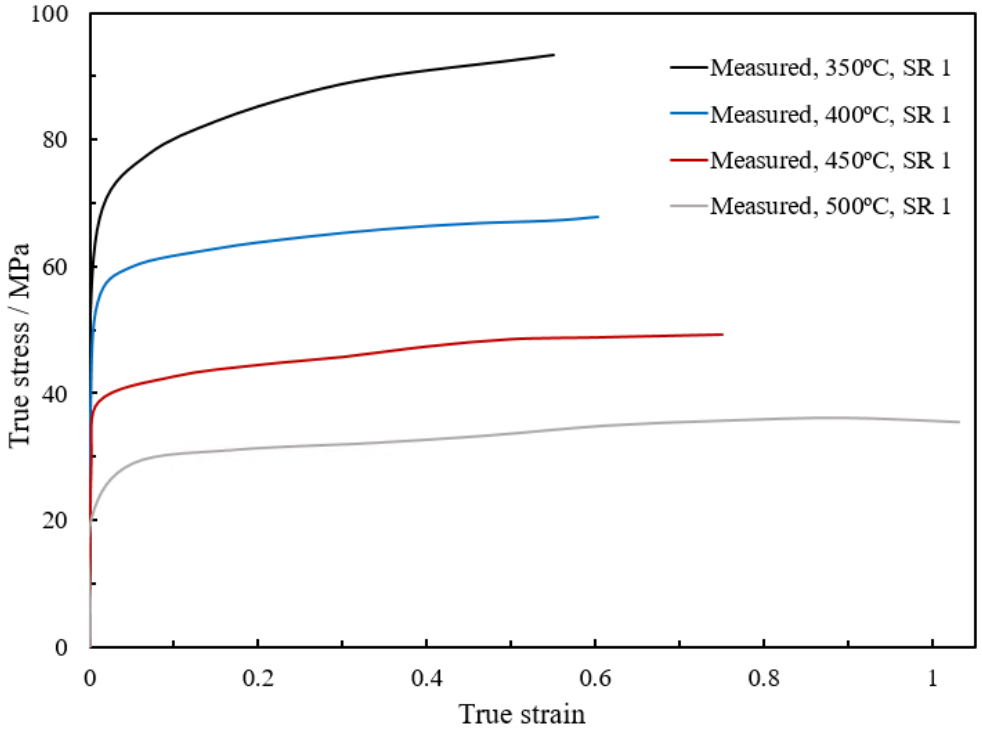

Figure 4.3: Stress-strain curves of AA6082 (a) at room temperature, (b) at different strain rates and (c) at different temperatures

The effect of strain rate on the flow stress at 450ºC is shown in Figure 4.3. (b). The flow stress of the material increases with the increasing strain rate due to the strain rate hardening effect. In addition, the higher strain rate leads to a greater ductility. Similar results were observed by (El-Danaf et al., 2008; Lassance et al., 2007). The failure strain increases from 0.65 to 0.8 when the strain rate increases from 0.01 to 5 s^{-1}. The observed behaviour can be explained by the effect of grain growth theory. The grain size grows larger within aluminium matrix at lower strain rates, which offsets the grain boundary deformation effect and results in a lower ductility (Mohamed et al., 2012).

The effect of temperature at 1 s^{-1} strain rate is illustrated in Figure 4.3. (c), the flow stress decreases with increasing temperature whereas the ductility of the material increases. The failure strain increases from 0.55 to 1.03 when the temperature increases from 350 to 500 ºC. This phenomenon is thermally activated as the mobility of dislocations is enhanced at higher temperature due to the activation of diffusion controlled processes, such as grain boundary rotation and dynamic recovery (Mohamed et al., 2012).

4.3 Effect of dislocations induced by high temperature plastic deformation

During pre-straining uniaxial tensile tests, the specimens were stretched to certain strain levels with different strain rates at 450°C and water quenched using Gleeble 3800 to simulate the FAST process. The pre-strained specimens were subsequently aged at 180°C until the full hardness curve of each specimen was achieved with obvious over-ageing phenomenon. Strength evolution and key information of each specimen during artificial ageing are demonstrated in Figure 4.4 and Table 4.2, respectively.

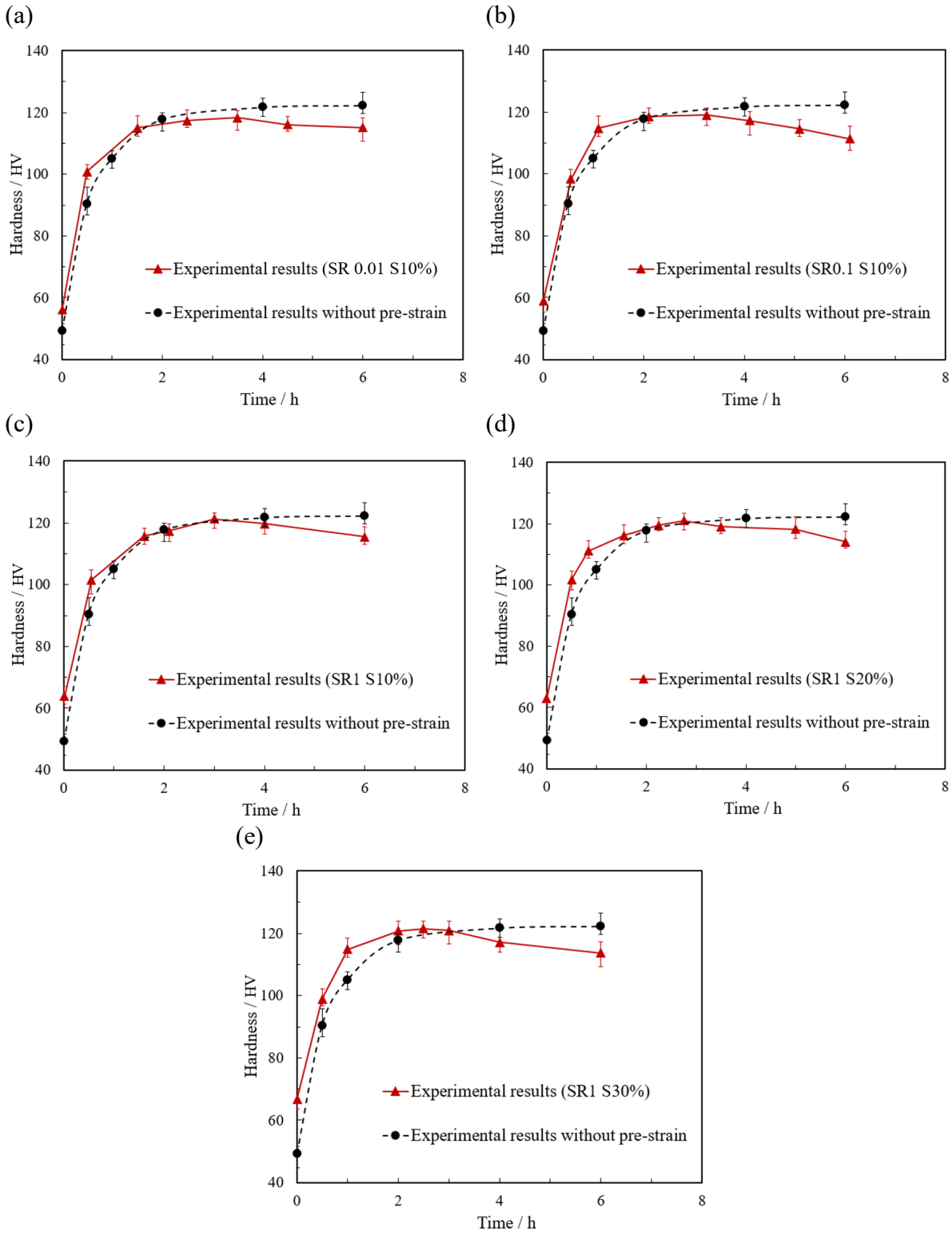

Figure 4.4: Comparison of hardness evolution for pre-strained specimens and the non-deformed specimen (a) SR 0.01s-1, Strain 10%, (b) SR 0.1s^{-1}, Strain 10%, (c) SR 1s^{-1}, Strain 10%, (d) SR 1s^{-1}, Strain 20% and (e) SR 1s^{-1}, Strain 30%

Figure 4.4 illustrates the comparison of the strength evolution between pre-strained specimens and the SSSS specimen, where solid curves represent the experimental results of pre-strained

specimens and dashed curves represent the experimental results of non-deformed specimens. After undergoing high temperature tensile tests and water quenching, the post-quenched hardness of pre-strained specimens is evidently higher than the SSSS material (48 HV). Compared to the SHTed specimen, hardness of pre-strained specimens increases more rapidly in the first 2 hour of artificial ageing and reaches to the peak hardness earlier. The time to obtain peak hardness is reduced from approximately 6 hours to at most 3.5 hours. The peak hardness of pre-strained specimens (118.3-121.3 HV) is slightly lower than that of the T6 temper material (122.2 HV). Both conditions exhibits a steep decrease in hardness during the over-ageing stage.

Table 4.2: Peak hardness and the corresponding ageing time for the samples with different pre-strained conditions (ageing at 180°C)

Strain rate (s^{-1})	Strain	Post-quenched hardness (HV)	Peak hardness (HV)	Peak ageing time (h)
0	0	48.0	122.2	6
0.01	10%	56.1	118.3	3.5
0.1	10%	58.9	119.0	3.25
1	10%	63.8	121.3	3
1	20%	63.9	121	2.75
1	30%	65.8	120.9	2.5

Table 4.2 clearly shows the detailed information of each specimen, such as post-quenched hardness, peak hardness obtained and peak artificial ageing time. With increasing strain level and strain rate, the time to reach peak hardness continues reducing from approximately 6 hours to less than 3.5 hours. At least 96.8% of the peak hardness can be retained among all the pre-strained specimens after ageing at 180°C for a certain period of time.

TEM analysis was conducted on a pre-strained specimen without ageing and multiple specimens that had been aged at 180 or 220°C with/without pre-strain as shown in Figure 4.5.

(a)

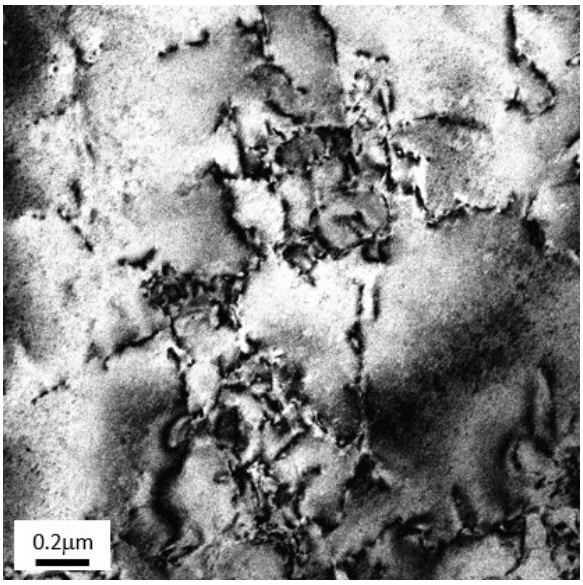

(b)

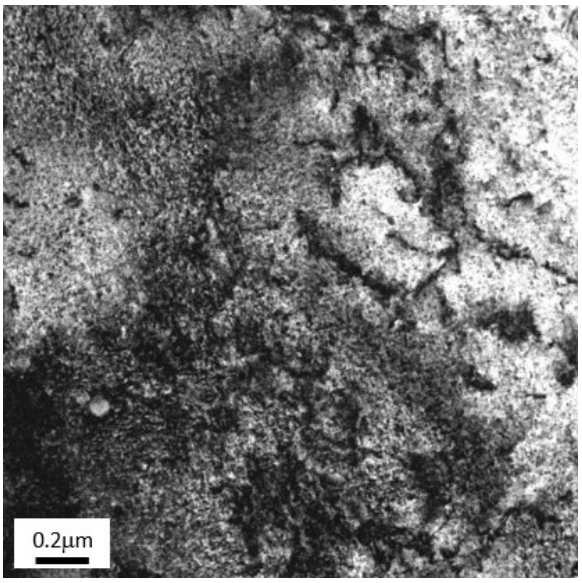

(c)

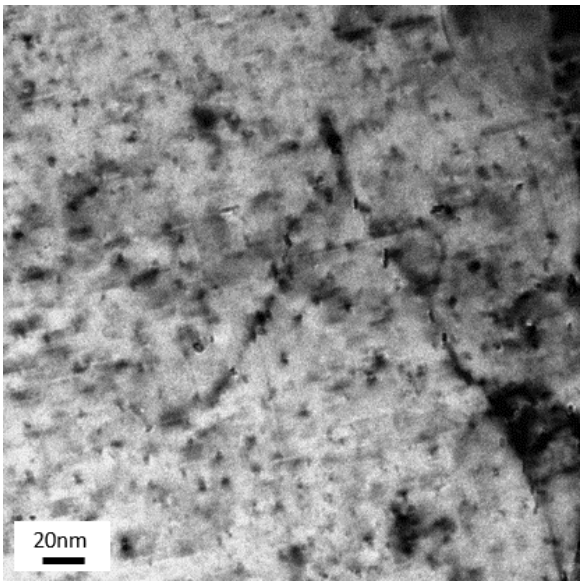

(d)

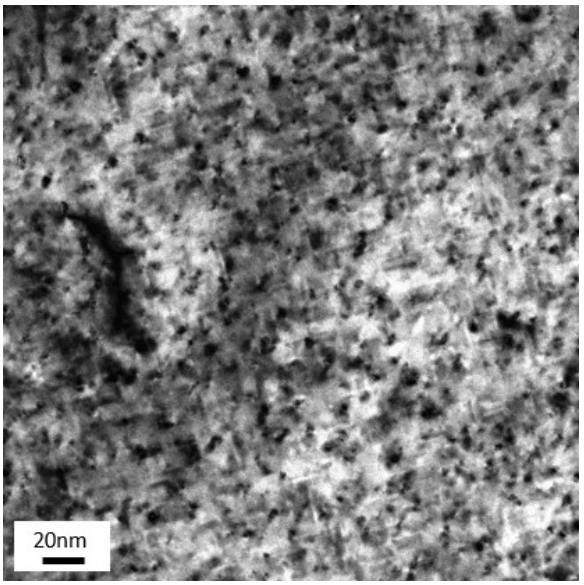

(e) (f)

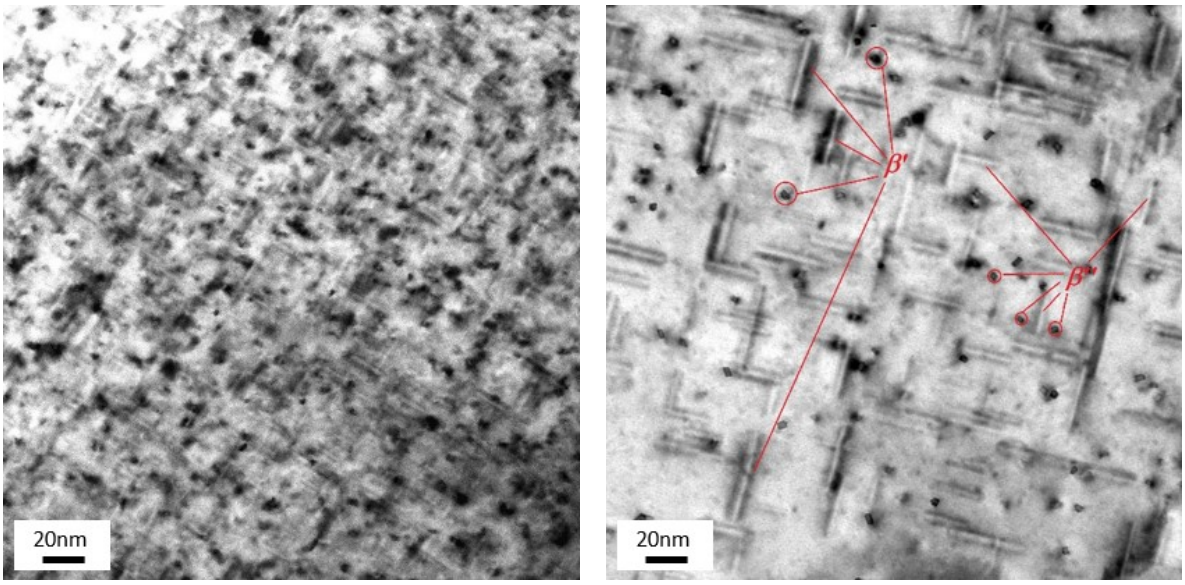

Figure 4.5: TEM bright field images of microstructures observed in the <100> Al zone axis orientation after artificial ageing with/without pre-strain (a) as-quenched sample with pre-strain (10%), (b) under-aged sample with pre-strain (10%), (c) under-aged sample with pre-strain (180°C), (d) peak-aged sample with pre-strain (180°C), (e) peak-aged sample without pre-strain (180°C) and (f) peak-aged sample without pre-strain (220°C)

Figure 4.5. (a) demonstrates large numbers of residual dislocations observed in the specimen undergoing high temperature stretching and subsequent rapid water quenching. By comparing with the microstructure in Figure 4.5. (b), it can be noticed that the density of dislocations decreases as artificial ageing begins.

Two major types of precipitates (needle-shaped *β''* and rod-shaped *β'* morphology), aligned along the <100> major axis of the aluminium matrix were observed in the specimens experiencing various ageing procedures. The needle-shaped *β''* and rod-shaped *β'* can be differentiated based on the respective shape of their cross sections. The cross section of the highly coherent *β''* follows the rectangular or parallelogram shape when scanned along <100> axis, which is consistent with the arrangement of a monoclinic unit cell identified earlier (Marioara et al., 2006). The *β'* precipitates clearly appear larger and have more roundish and irregular cross sections (Du et al., 2016). Figures 4.5. (c) and (d) show the bright-field TEM micrographs of pre-strained (10%) specimens aged at 180°C for 1 hour and 3 hours, respectively. Small *β''* precipitates (approximately 12.4 nm in length) are the dominant microstructural phases in Figure 4.5. (c) and a large number of dislocations are observed in the

grains. In Figure 4.5. (d), the dislocation density is decreased and the needle-shaped β'' phase precipitates grow gradually from 12.4 nm to around 15.6 nm. Moreover, some rod-shaped β' precipitates also exist, which means the transitional process from β'' to β' is underway. The number density of both phases of precipitates is higher around dislocation lines.

Figures 4.5. (e) and (f) show the typical micrographs of peak-aged specimens without pre-strain at 180°C and 220°C. In these two figures, β'' and β' phase precipitates are observed clearly while dislocation lines are difficult to identify which accords with the non-deformed testing conditions. In addition, the distribution of precipitates in Figure 4.5. (e) is more uniform than that of Figure 4.5. (f), and the average size is evidently smaller (13.2 nm vs 28.8 nm in length). Compared with the microstructure of the peak aged specimen with pre-strain in Figure 4.5. (d), it is noticed that the size of precipitates in Figure 4.5. (e) is slightly smaller (15.6 nm vs 13.2 nm in length) and distribution is finer as well. During the high temperature tensile tests, all the T4 temper specimens were pre-stretched (10%, 20% and 30%) with different strain rates (0.01, 0.1 and 1 s^{-1}) prior to artificial ageing. It is deduced from the post-quenched hardness in Table 4.2 that a higher strain rate and amount of pre-strain at deformation period would induce larger dislocation densities but remain even after water quenching. The presence of these residual dislocations will strongly influence the mechanical properties of the aluminium alloys, especially strength. In the FAST process, the dislocation density in a material increases with plastic deformation, following the relationship: $\rho \propto \tau^2$, where τ is flow stress and ρ is dislocation density (Khan et al., 2008). According to the Frank-Read theory, these dislocations frequently propagate and pile up on slip planes at the grain boundaries (Dieter and Bacon, 1986). On the other hand, in high temperature deformation, dislocations become mobile and are able to glide, cross-slip and climb, where annihilation of dislocations becomes possible (Pei and Stocks, 2018; Yan et al., 2016). The residual dislocations are dependent on the amount of strain and strain rate due to different recovery times at high temperature. The tangled dislocations gradually increase the resistance to further dislocation motion, and hence strengthen the material. This strain hardening effect explains the higher hardness of specimens after pre-straining when compared to the SSSS specimen. After water quenching, dislocations act as sinks for quenched-in vacancies so that the suppressed supersaturated state of the aluminium matrix prevents low-temperature clustering activities (Birol, 2005). These clusters otherwise have a detrimental effect on the precipitation response of the material, because they are difficult to dissolve and are not suitable nucleation sites for the main hardening phase β''

(Martinsen et al., 2012; Torsæter et al., 2010). On the contrary, dislocations act as favourable nucleation sites for the pre-β'' phase precipitates. The slower bulk diffusion mechanism for the formation of precipitates is replaced by the faster dislocation-assisted diffusion mechanism (Kolar et al., 2012). The presence of dislocations ensures more solute elements but also a larger driving force to form GP-I zones that readily grow to β'' phase, following the artificial ageing process. In the early stage of artificial ageing, the density of the precipitates is higher and the distribution of the precipitates is evenly dispersed for the pre-strained specimen, contributing to a shorter required time to obtain peak hardness compared with the non-deformed specimen. As seen in Figures 4.5. (c) and (d), numerous precipitates are distributed around the dislocations in the pre-deformed specimens. As ageing continues, however, the drawbacks associated with induced dislocations are observed. Due to the faster growth and coarsening rates provided from dislocations, the hardening β'' phase and rod-shaped β' phase precipitates in the pre-deformed specimen begin to coarsen earlier as compared to the non-deformed specimen. This can be observed from the precipitate sizes in Figures 4.5. (d) and (e) (15.6 nm vs 13.2 nm in length). Consequently, the peak hardness of pre-strained specimens is lower than that of non-deformed specimens. Moreover, the precipitates coarsen more rapidly under higher ageing temperature as observed in Figures 4.5. (e) and (f).

In conclusion, the presence of induced dislocations influences the change in the strength of the material significantly. The strain hardening and acceleration of precipitation response are beneficial as the time to achieve peak hardness is shortened greatly. However, the loss of peak strength can also occur, which depends on the pre-strain levels. The effect of residual dislocations on the artificial ageing response was qualitatively and quantitatively studied and integrated into the post-form strength prediction model.

4.4 Quenching sensitivity

After reaching the target temperature 450°C, the ultra-fast heated specimens were immediately quenched either by air or by water with various rates and artificially aged at 180°C for 5 hours. The details of quenching are shown in Table 4.3 and the temperature histories of the specimens are plotted in Figure 4.6. The experimental hardness evolution and corresponding peak hardness for each specimen are illustrated in Table 4.4 and Figure 4.7.

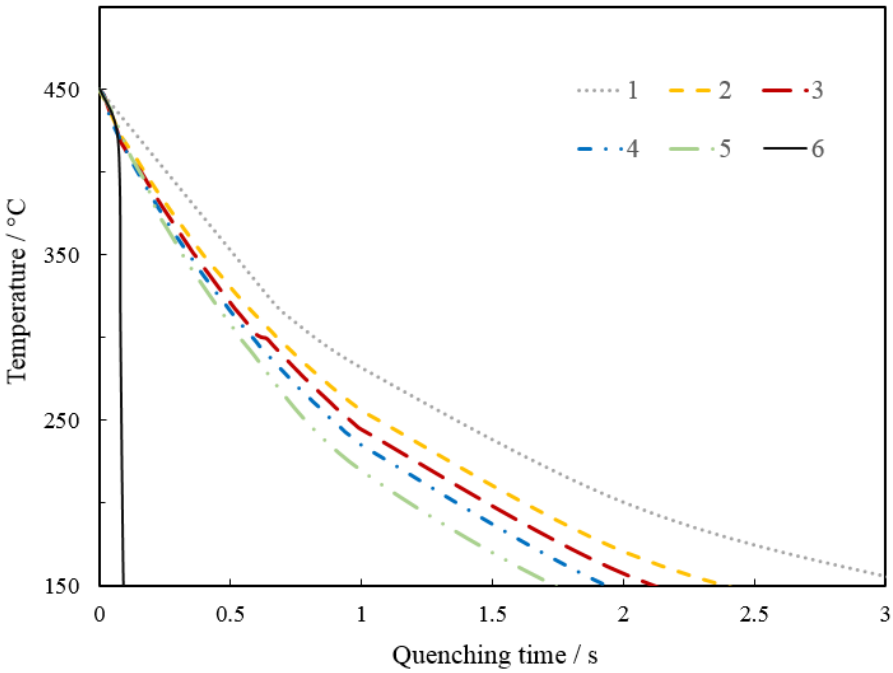

Figure 4.6: Temperature evolutions of the specimens in the quenching tests

Table 4.3: Quenching information for each specimen

Number of specimens	1	2	3	4	5	6
Quenching method	AQ	AQ	AQ	AQ	AQ	WQ
Quenching rate (450-200°C) (°C/s)	181.2	235.8	260.4	285.1	311.0	1632.9
Average quenching rate (°C/s)	67.9	73	75.2	76.1	77.9	1632.9

In Figure 4.6, Curve 6 is the temperature evolution of the water quenched specimen and curves 1-5 are temperature evolutions of air quenched specimens. This figure shows the transient nature of the cooling rate and demonstrates the need to calculate an average quenching rate at the sensitive temperature range during FAST, in order to make quantifiable comparisons. As shown in Table 4.4, the quenching rate of the water-quenched specimen is extremely high (up to 1632.9°C/s) which means less than 0.3 seconds is required to cool the hot specimen to room temperature. The average air cooling rates range from 181.2 to 311.0°C/s (with 25°C increment) between 450 and 200°C.

Table 4.4: Peak hardness obtained for each specimen after artificial ageing at 180°C

Number of specimens	1	2	3	4	5	6
Peak hardness (HV)	63.6	85.4	103.0	115.5	121.8	122.4

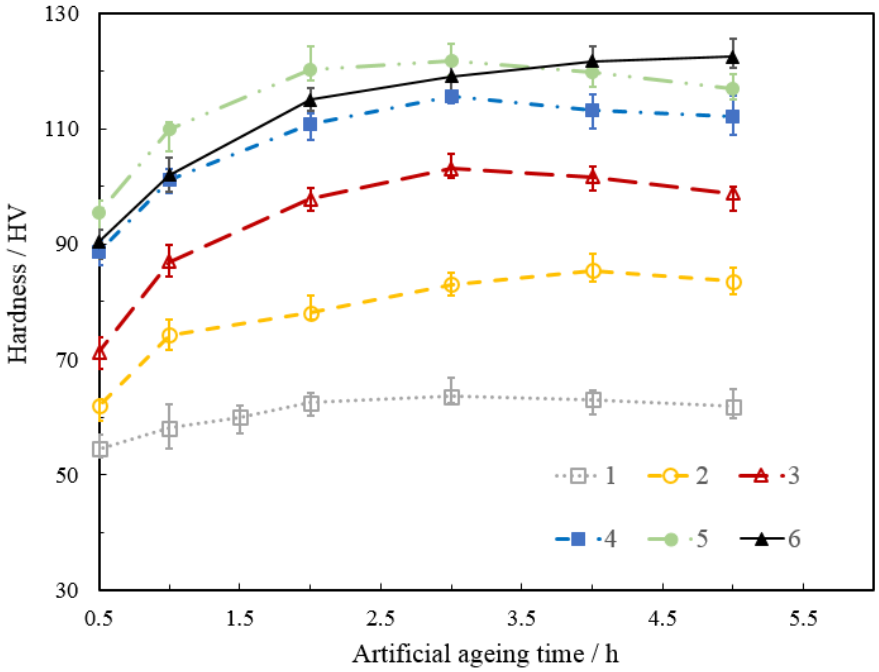

Figure 4.7: Hardness evolutions of the post-quenched specimens during artificial ageing

As seen in Table 4.4, the hardness of specimen 1 is the lowest among all other samples, settling to a peak value of approximately 63 HV after 3 hours artificial ageing. Moreover, hardness evolution curves for specimens 2 to 5 (Figure 4.7) lie between specimen 1 and specimen 6, for which the peak hardness increases in ascending order. Hardness evolution for water-quenched specimen 6 exhibits an ever-increasing trend with highest values. The peak hardness values for specimen 5 and specimen 6 are very close while the time to reach the peak hardness is 3 and 5 hours, respectively. Comparing with the quenching rates displayed in Figure 4.7, it can be deduced that the peak hardness obtained during artificial ageing is positively correlated with quenching rate. It follows the generally accepted trend that rapid quenching leads to a higher peak value, with a negligible difference after the critical quenching rate is achieved. However, the time to obtain peak hardness for the water-quenched specimen is longer while the difference between air-quenched specimens is not very apparent.

After 5 hours artificial ageing, specimens 3 and 6 were selected to further conduct TEM observations. TEM images were taken along <100> Aluminium axis where precipitates can be easily observed.

(a) (b)

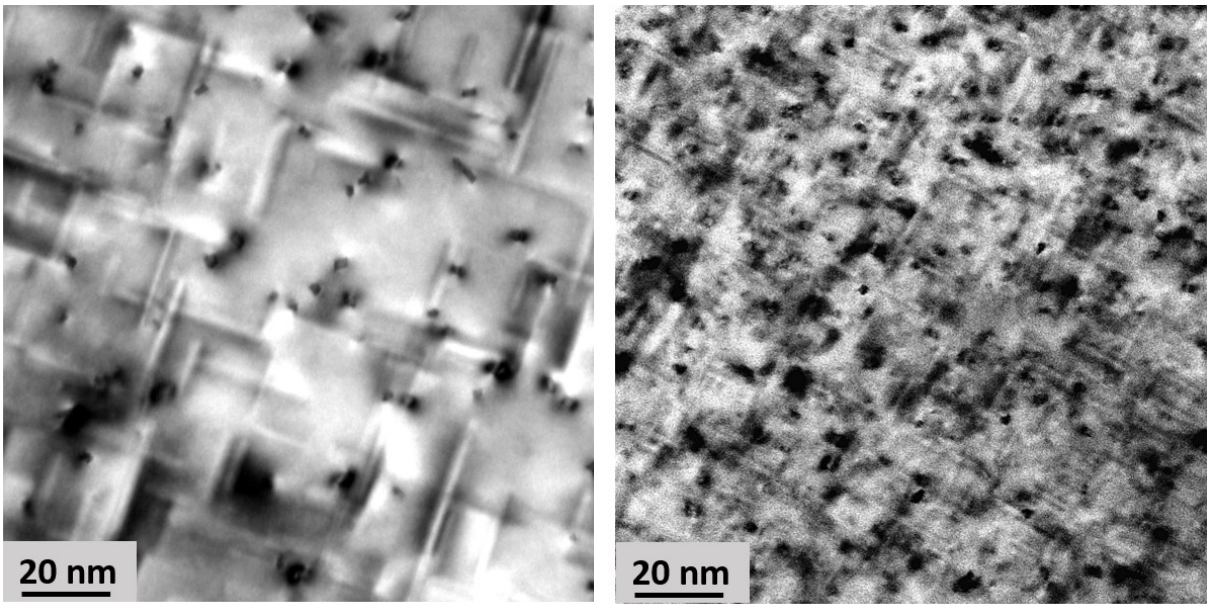

Figure 4.8: TEM bright field images of microstructures observed in the <100> Al zone axis orientation (a) specimen 3 after AQ & 5h AA and (b) specimen 6 after WQ & 5h AA

Specimen 3 and specimen 6 are quenched either by air or water and their peak hardness values are 103.0 and 122.4 HV, respectively. A lower peak hardness value for Specimen 3 suggests a suboptimal quenching rate (260.4°C/s) was used when compared with the water quenched specimen 6 (1632.9°C/s). With regard to the microstructures, needle-shaped β'' precipitates, observed as dots when considering their end-on views, have been observed along the <100> major axis in both TEM images. However, large size rod-shaped β' precipitates can only be detected in specimen 3 and the distribution of precipitates in the aluminium matrix in Figure 4.8. (b) is more uniform and finer than Figure 4.8. (a). Additionally, the number density of precipitates is notably greater and the average size of precipitates is obviously smaller in Figure 4.8. (b) compared with microstructures in Figure 4.8. (a), 13.2 nm vs 30.6 nm in length respectively.

Summarising the quenching details and peak hardness values shown in Table 4.3 and Table 4.4, it can be observed that the obtained peak hardness is particularly sensitive to the average quenching rate in the critical temperature range 450-250°C when compared to the overall average quenching rate (rate difference is less than 10°C/s for the air-quenched specimens), which suggests that the detrimental effect is mainly induced at relatively higher temperatures. From the point view of precipitation, it is due to the formation of equilibrium phase β

precipitates during the quenching process when the cooling curve of temperature crosses the CCP diagram. The final peak hardness of the specimen could be markedly lowered to 63.6 HV if the quenching rate is below 180°C/s in the critical temperature range. Conversely, full strength is attained as long as the quenching rate is over the required critical quenching rate (CQR), inferred as approximately 300°C/s in the first 250°C temperature drop, in this case. It is also worth mentioning that if the requirement of CQR is met, the obtained peak hardness values will be very close, even if the difference between the quenching rates is over 1000°C/s.

With the aid of well correlated TEM bright field micrographs, it was easy to observe that for well-quenched specimens after artificial ageing, the number density of needle-shaped β'' precipitates is large and distribution is fine. From the aforementioned established precipitation sequence of heat treatable 6xxx series aluminium alloys during artificial ageing, the major hardening precipitates are the needle-shaped β''. For specimens with an insufficient quenching rate, the coarse β' and β precipitates are most likely induced. These β' and β precipitates consume lots of Si and Mg solute atoms, are unable to reversely transform to the preferred needle-shaped strongest β'' and coarsen rapidly during artificial ageing. In comparison to β'', they contribute poorly to strength as they are readily bypassed by the dislocation movements. Thus, with a blend of β'', β' and β precipitates, the volume fraction of precipitates is lower and average radius of precipitates is larger leading to a weaker ability to hinder dislocation motions and hence a lower peak hardness, compared to the well-quenched specimens with finely distributed needle-shaped β'' precipitates in the matrix.

Therefore, it is of importance to control the quenching rate during the FAST process to suppress the formation of the equilibrium and less hardening phases of β' and β precipitates that would deteriorate the post-form heat treatment response. It is revealed that the quenching rates utilised should be greater than 300°C/s in the most sensitive temperature range after ultra-fast heating. The experimental results for the specimens quenched at different rates during the artificial ageing contribute to the quantitative analysis of quenching sensitivity and the development of the quenching sub-model.

4.5 Multi-stage artificial ageing response

In the one-stage artificial ageing tests, the specimens were aged at 180, 190, 220 and 240°C until obvious over-ageing phenomenon could be detected. The hardness evolutions are given in Figure 4.9 and the key parameters of artificial ageing are summarised in Table 4.5.

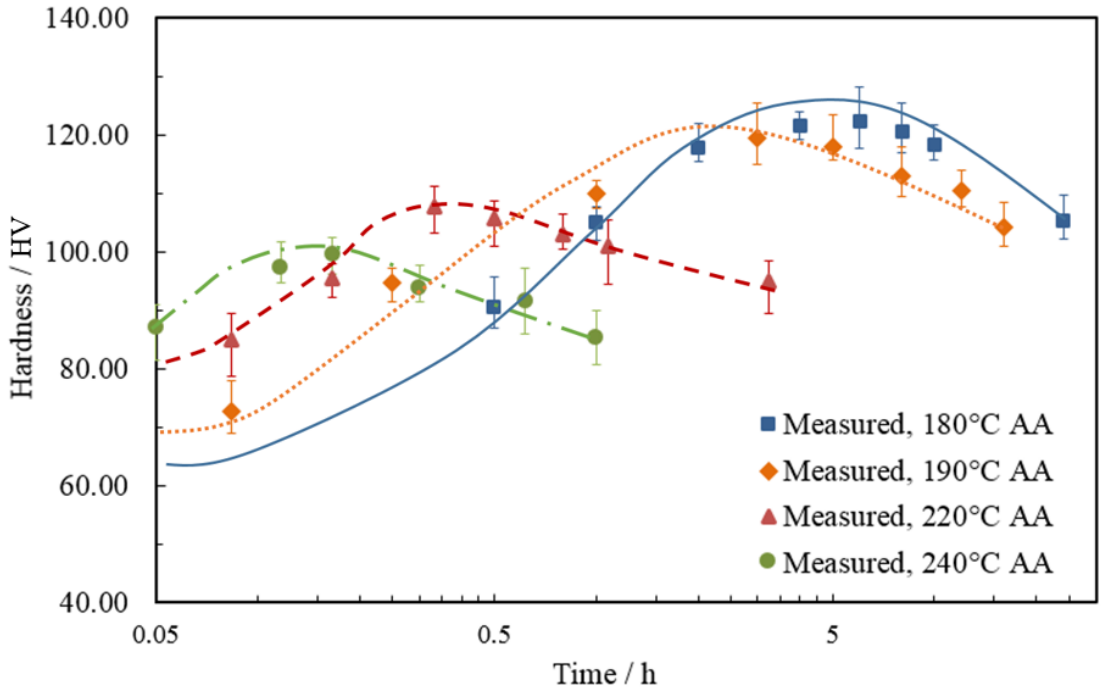

Figure 4.9: Experimental results for the specimens aged at different temperatures

The hardness of specimens artificially aged at different temperatures increases rapidly during the early stage until reaching the peak hardness. Then the hardness starts to decrease with ageing time that is denoted as over-ageing phenomenon. The time to reach peak hardness is shortened with increasing artificial ageing temperature and the consequent peak hardness is decreasing. The detailed information is listed in Table 4.5.

Table 4.5: Key artificial ageing parameters

	180°C	190°C	220°C	240°C
Peak hardness / HV	122.2	118.0	107.7	99.7
Time to achieve peak hardness / h	6.0	3.0	0.3	0.17

With regard to the two-stage ageing, the first-stage ageing was conducted at 220°C with the time ranging from 3 to 6 minutes. The second-stage ageing was then carried out at 190°C for

20, 40, 120 and 240 minutes to determine the ageing response, respectively. The measured post-form hardness is shown in Table 4.6.

Table 4.6: The hardness of specimens during two-stage artificial ageing (Unit: HV)

1st stage 220°C ageing time (min)	2nd stage 190°C ageing time (min)			
	20	40	120	240
3	101.9	111.0	**116.3**	113.7
4	103.2	110.7	**114.6**	113.8
5	101.9	109.2	**114.0**	110.8
6	99.6	98.7	**112.3**	111.3

The peak hardness of one-stage ageing at 190 and 220°C are 118.0 and 107.7HV respectively. For the two-stage ageing results shown in Table 4.6, all of the peak values of the two-stage ageing lie between 118.0 and 107.7HV and the peak strength decreases with increased ageing time at 220°C. Additionally, the time to obtain peak strength is reduced from 3 hours at 190°C one-stage ageing to approximately 2 hours at two-stage ageing .

This phenomenon can be explained by the effect of temperature on the ageing response of Al-Mg-Si alloys. Theoretically, the equilibrium solute concentration at lower ageing temperature is less than that at higher temperature due to the reduced matrix phase solubility. The volume fraction is directly proportional to the loss of solute concentration in the aluminium matrix. Therefore, the equilibrium volume fraction of precipitates decreases with increasing ageing temperature, indicating that fewer precipitates form at a higher temperature. Furthermore, the higher ageing temperature accelerates the formation, growth and coarsening of precipitates due to the faster solute transportation via diffusion. Given that precipitation hardening is the controlling hardening mechanism during ageing, the fewer formed equilibrium precipitates and the coarser distribution of precipitates leads to a lower peak hardness. The distribution of precipitates formed at the first-stage ageing (220°C) is non-uniform in nature. However, during the second-stage ageing (190°C), the remaining alloying elements can precipitate around the nucleation sites more finely and uniformly, which compensates the effect of the first-stage ageing to a certain extent. This results in the peak strength of two-stage ageing being greater than the single-stage ageing at 220°C but lower than that at 190°C. The acceptable peak strength can be achieved through multi-stage ageing with optimal ageing conditions as the

nucleation is greatly accelerated during early stage ageing at a higher temperature, which allows the rapid growth of precipitates in subsequent ageing at a lower temperature.

4.6 Summary

The post-form strength of 6xxx aluminium alloys manufactured by the FAST process is highly dependent on the thermo-mechanical history in the stamping process and conditions of post-form heat treatment. The microstructure and strength evolution during the FAST process have been comprehensively studied. A good understanding to the nature of the novel stamping technology was achieved through the analysis of decoupled experimental results, which provides the foundation for the development of the post-form strength prediction model.

Figure 4.10 shows the schematic diagram of the corresponding microstructural evolutions during FAST process. Spherical pre-β'' phase precipitates are formed during ultra-fast heating process and dislocations are induced by high-temperature plastic deformation. As artificial ageing proceeds, pre-β'' precipitates are converted to needle-shaped β'' precipitates and residual dislocations start to annihilate. In the peak ageing condition, a blend of numerous β'' precipitates and minute rod-shaped β' can be observed in the matrix.

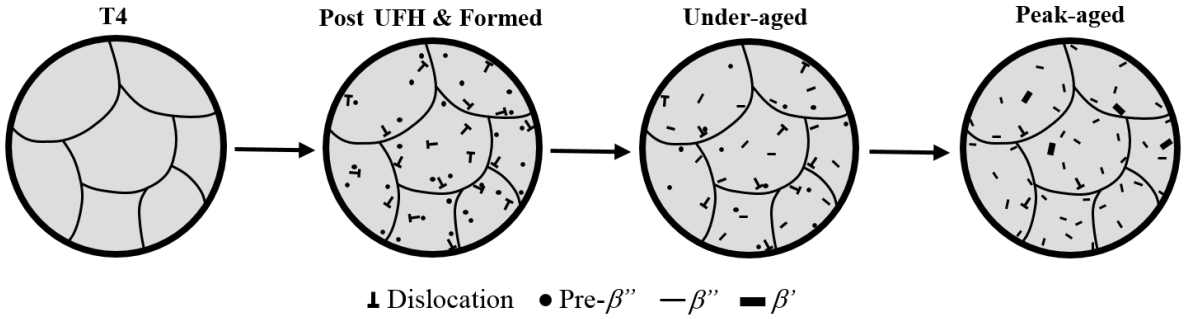

Figure 4.10: Schematic diagram of microstructural evolutions during FAST process

Ultra-fast heating to an elevated temperature causes the dissolution of room temperature clusters and formation of spherical pre-β'' phase precipitates that would accelerate their transformation to major hardening phase needle-shaped β'' precipitates. However, reduction in peak strength is also possible to occur with the additional level of these precipitates. The residual dislocations induced by high-temperature plastic deformation strengthen the material and favour the precipitation response during artificial ageing. Effective quenching is able to

suppress the precipitation process. Insufficient quenching is proved to be harmful to the post-form strength of the material as the undesired precipitates formed would weaken the precipitation kinetics. Multi-stage ageing can reduce the time to obtain peak strength significantly at the cost of slight loss in strength.

Chapter 5. Development of the post-form strength prediction (PFS) model for 6xxx aluminium alloys during FAST

In this chapter, the development of the post-form strength prediction model is documented. The PFS model is comprised of five sub-models: flow stress model, quenching model, artificial ageing model, multi-stage artificial ageing model and particle size distribution (PSD) sub-model. First four sub-models aim to predict strength evolution of 6xxx aluminium alloys under various manufacturing conditions and the PSD sub-model offers an additional function of simulating size distribution of precipitates. The experimental results obtained in Chapter 3 are used to calibrate the PFS model.

5.1 Development of the unified PFS model

5.1.1 Flow stress sub-model

Based on the well-known viscoplastic theory, a set of modified constitutive equations of Eqs. (5-1) to (5-5), were used to model the yield stress and the relevant microstructural evolutions during high temperature plastic deformation stage in the FAST process (Garrett et al., 2005; Lin et al., 2002; Lin and Liu, 2003; Zhan et al., 2011).

$$\sigma_{total} = E\left(\varepsilon_T - \varepsilon_p\right) \tag{5-1}$$

$$\dot{\varepsilon_p} = \left(\frac{\sigma_{total}-\sigma_{dis}-k}{K}\right)^{n_1} \tag{5-2}$$

$$\sigma_{dis} = B \cdot \bar{\rho}^{0.5} \tag{5-3}$$

$$\overline{\rho} = \frac{\rho-\rho_i}{\rho_m} \tag{5-4}$$

$$\dot{\overline{\rho}} = A_0 \cdot \dot{\varepsilon_p} - A_0\overline{\rho} \cdot \dot{\varepsilon_p} - C_p\overline{\rho}^{n_2} \tag{5-5}$$

This chapter is based on the paper work:

"Zhang, Q., Luan, X., Dhawan, S., Politis, D.J., Du, Q., Fu, M.W., Wang, K., Gharbi, M.M., Wang, L., 2019. Development of the post-form strength prediction model for a high-strength 6xxx aluminium alloy with pre-existing precipitates and residual dislocations. Int. J. Plast. 119, 230–248."

where n_1, n_2, A_0, B and C_p are material constants, determined from experimental data. $\sigma_{total}, E, \varepsilon_T, \varepsilon_p, \sigma_{dis}, k, \overline{\rho}$ denote flow stress, Young's modulus, total strain, plastic strain, stress due to dislocation hardening, threshold stress and the normalized dislocation density of the material, respectively. It is noticed that K, k, B, n_1, A_0 and C_p are temperature dependent. Eqs. (5-6) to (5-12) represents the Arrhenius equations for these parameters.

$$K = K_0 \exp(Q_K/RT) \tag{5-6}$$

$$k = k_0 \exp(Q_k/RT) \tag{5-7}$$

$$B = B_0 \exp(Q_B/RT) \tag{5-8}$$

$$n_1 = n_{10} \exp(Q_{n_1}/RT) \tag{5-9}$$

$$A_0 = A_{00} \exp(Q_{A_{00}}/RT) \tag{5-10}$$

$$C_p = C_{p0} \exp(Q_{C_p}/RT) \tag{5-11}$$

Eq. (5-2) describes the traditional power law formulation of viscoplastic deformation, computing the plastic strain rate by correlating flow stress, dislocation hardening and threshold stress (Lin and Liu, 2003). In Eq. (5-3), the normalized dislocation density is used to characterise the isotropic hardening phenomenon in the plastic deformation period based on the classic work hardening theory in the following (Nieto-Fuentes et al., 2018; Zhang and Ngan, 2018):

$$\sigma_{dis} = \alpha MGb \cdot \rho^{0.5} \tag{5-12}$$

where α is a material constant, M is the Taylor factor, G is the shear modulus and b is the magnitude of Burgers vector. In Eq. (5-3), all the material constants are replaced by a single constant B and the normalized dislocation density $\overline{\rho}$ is used instead, to simplify the calculation of Eq. (5-12).

The normalized dislocation density is defined in Eq. (5-4) (Zhan et al., 2011) and ρ_i is the initial dislocation density and ρ_m is the maximum dislocation density the material could generate during deformation. Typically, $\rho_i \ll \rho_m$ and therefore the value of normalized dislocation density is assumed to be in-between 0 and 1. In this method, the evolution of dislocation density is adjusted from different orders of magnitude to a notionally common scale.

In the FAST process, the dislocation density is affected by the accumulation and annihilation effects (Garrett et al., 2005; Zhang et al., 2013). Eq. (5-5) illustrates the normalized dislocation density in a rate form, where the first term ($A_0 \cdot \dot{\varepsilon_p}$) denotes the dislocations generated due to plastic deformation, the second term ($A_0\overline{\rho} \cdot \dot{\varepsilon_p}$) represents the dynamic recovery of dislocations at elevated temperature and the final term ($C_p\overline{\rho}^{n_2}$) describes the effect of static recovery. The computed value of dislocation density will be an imported parameter in the artificial ageing sub-model, allowing the prediction of the effect of dislocations on the precipitation behaviour.

5.1.2 Quenching sub-model

In the FAST process, quenching is a critical stage following high temperature plastic deformation, which determines the precipitation order and hence affects the achievable peak strength. Therefore, the quenching sub-model is required to be established to facilitate the complex strength prediction for insufficiently quenched components during the entire process.

The investigation of quenching sensitivity was presented in Section 4.4. It is found that the stable equilibrium β phase precipitates are formed due to insufficient quenching, leading to a weaker precipitation response during artificial ageing. These equilibrium phase precipitates coarsen rapidly during artificial ageing and cannot convert to the hardening phase β'' (Milkereit et al., 2012; Milkereit and Starink, 2015). As a consequence, the contribution of the quench-induced precipitates to the overall strength of the material is very limited. Additionally, based on the previous analysis, the most sensitive temperature range for precipitation during quenching is between 450 and 200°C, during which the critical quenching rate is 300°C/s. It is notable that once the critical quenching rate is reached, the difference in the strength evolutions during artificial ageing is negligible.

The temperature history is selected to compare with the continuous cooling precipitation diagram to compute the specific amount of precipitates formed in the quenching. The

quenching sub-model showed in Eqs. (5-13) and (5-14) is an important part of the unified PFS model.

$$Q = Q_0 \cdot e^{\frac{Q_q}{RT_c}} \tag{5-13}$$

$$C_q = (1 - Q) \cdot C_0 \tag{5-14}$$

where C_q is the loss of solute concentration after quenching, Q is the quenching factor, C_0 is the maximum solute concentration after quenching (C_i of SSSS), Q_0 is the pre-exponential quenching factor, Q_q is the activation energy for diffusion controlled precipitation behaviour during quenching, R is universal gas constant, and T_c is the start temperature when the quenching evolution curve intersects the CCP curve. It is noticed that T_c equals to infinity if the intersection point of two curves does not exist and the value of C_q equals to zero, which means the quenching rate is sufficient and no undesirable precipitates are induced. When the quenching evolution curve is tangent to the CCP curve, C_q is also set as zero because the quenching rate is same as the critical quenching rate.

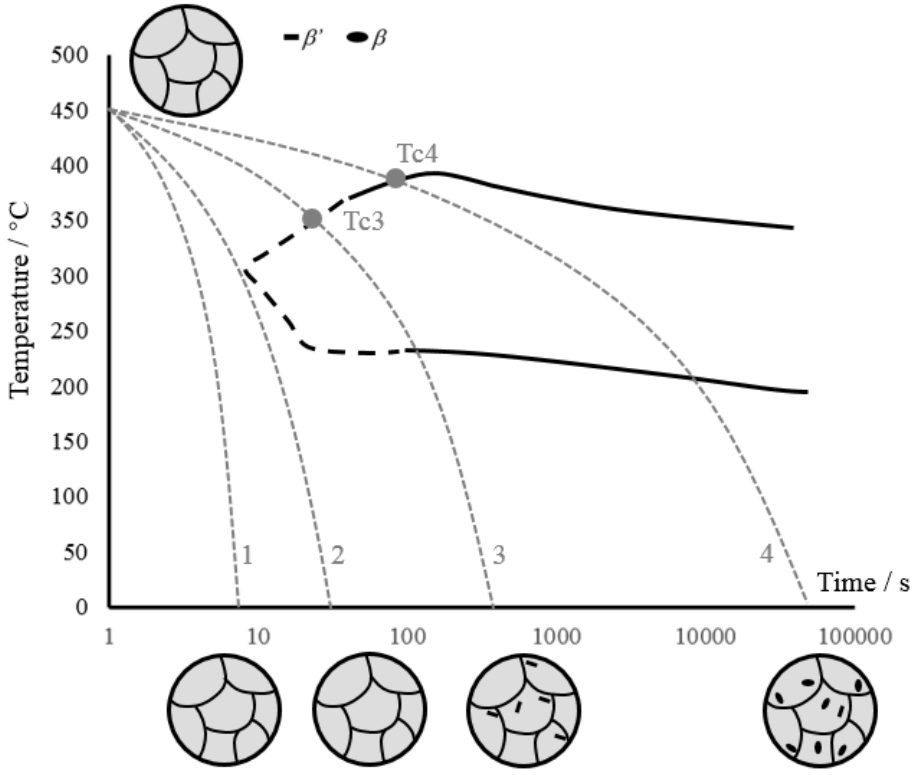

Figure 5.1: Schematic diagram of the precipitation mechanism during quenching

Figure 5.1 shows the schematic diagram of the precipitation mechanism during quenching. Quenching rates of curve 1 and curve 2 are greater than/equal to the critical quenching rate so that no microstructural change can be observed after quenching. Quenching curves 3 and 4 cross the CCP curve and the corresponding intersection points are T_{c3} and T_{c4}. In curve 3, rod-shaped β' phase precipitates are formed after quenching. In the aluminium matrix of the material with quenching curve 4, a blend of β' and equilibrium β phase precipitates can be observed, which would reduce strengthening behaviour in the subsequent artificial ageing. Consequently, the loss of solute concentration after quenching follows the relationship: $C_{q1} = C_{q2} < C_{q3} < C_{q4}$.

The volume fraction and solute concentration of the atoms in the matrix are affected due to the formation of the quench-induced precipitates. Its strength contribution is minimal and decreases sharply as artificial ageing time increases. This type of precipitate consumes solute atoms and occupies the volume fraction of the strengthening phases, with large size (radius and length). Thus, the status of the microstructural parameters C_t, f and r are required to be modified. However, the changes in the volume fraction or the mean radius of precipitates are not tracked. The quenching sub-model assumes the solubility is reduced after insufficient quenching and ignores the minimal strength contribution of this quench-induced precipitate, so that the values of f and r are set as zero. The σ_{ppt} after quenching is guaranteed as zero by this approach. As artificial ageing proceeds, the solute concentration decays with time starting from the initial value C_i. The volume fraction is proportional to the solute loss and newly formed strengthening precipitates follow the cubic law. The value of loss of solute concentration during quenching C_q is imported to the artificial ageing sub-model when computing the evolution of solute concentration during ageing process.

5.1.3 Artificial ageing sub-model

A refined age-hardening model of Eq. (5-15) was developed to predict the precipitation response during post-form heat treatment. It considers several important microstructural variables, such as volume fraction, the mean radius of precipitates, dislocation density and solute concentration.

$$\sigma_y = f(f_t, r, \rho, C_t) = g(\sigma_{dis}, \sigma_{ss}, \sigma_i, \sigma_{ppt}) \tag{5-15}$$

The precipitation of 6xxx series aluminium alloy during artificial ageing has been widely investigated and the yield strength is usually computed by the summative contributions of aluminium matrix, solid solution and precipitates (Esmaeili et al., 2003b; Esmaeili and Lloyd, 2005). Notably, in the refined model, the effect of dislocations is introduced in Eq. (5-16). The yield strength is then the sum of dislocation hardening contribution σ_{dis}, solid solution strength σ_{ss}, intrinsic strength of the aluminium matrix σ_i and contribution from precipitation hardening σ_{ppt} (including the contributions from shearable precipitates σ_{sh} and bypassing precipitates σ_{by} mechanism). The conversion between hardness and yield strength can be readily expressed by an empirical equation of Eq. (5-17) (Zhan et al., 2011). A schematic graph of the summative nature of each contribution effect on the yield strength is shown in Figure 5.2, which is obtained by running the complete post-form strength prediction model for the material with 10% pre-strain prior to performing artificial ageing at 180°C.

$$\sigma_y = \sigma_{dis} + \sigma_{ss} + \sigma_i + \sigma_{ppt} = \sigma_{dis} + \sigma_{ss} + \sigma_i + \frac{\sigma_{by} \cdot \sigma_{sh}}{\sigma_{by} + \sigma_{sh}} \tag{5-16}$$

$$HV = 0.33\sigma_y + 22.2 \tag{5-17}$$

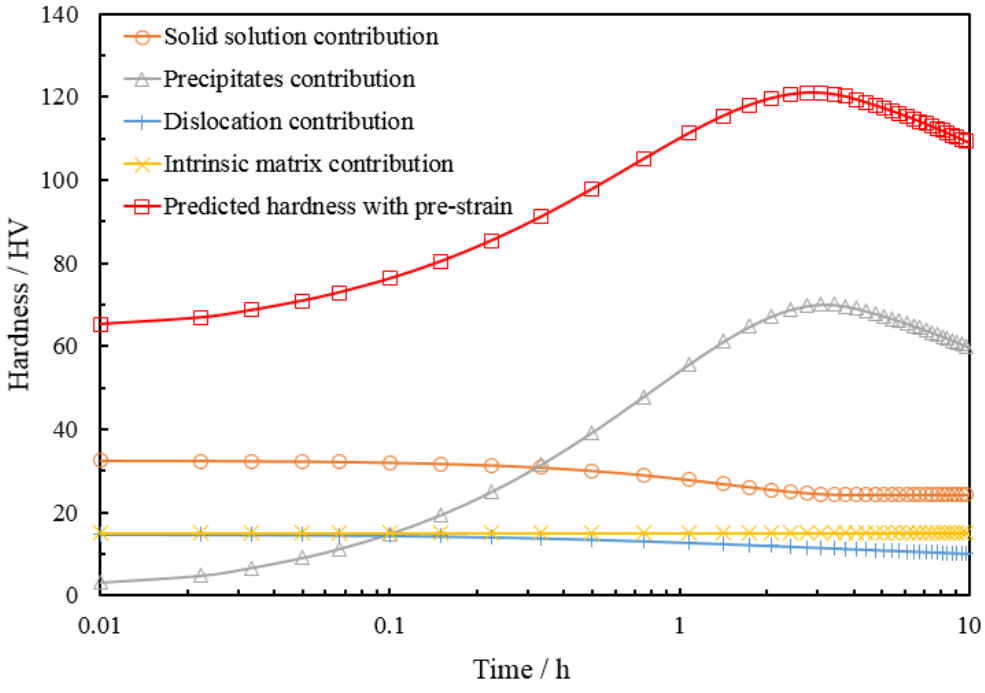

Figure 5.2: Contributions of solid solution, aluminium matrix and precipitates to hardness during 180°C ageing with 10% pre-strain

To accurately model the precipitation sequence behaviour, it is necessary to consider the composition of the alloys. AA6082 aluminium alloy is a ternary alloy, where Mg and Si are the major alloying elements dissolved in the aluminium matrix (Myhr et al., 2004; Shercliff and Ashby, 1990) Most of the solute atoms (including Mg, Si, Mn, Fe, Cu, etc) are re-dissolved in the aluminium matrix after ultra-fast heating and precipitate gradually during subsequent artificial ageing processes. The equilibrium solute concentration depends on the temperature of artificial ageing and represented by Eq. (5-18).

$$C_e = A \cdot e^{-Q_s/RT} \tag{5-18}$$

where A is a constant, Q_s is the solvus boundary enthalpy, R is the universal gas constant (8.314 J/mol·K) and T is artificial ageing temperature. When $T = T_s$, the metastable solid solvus temperature, the maximum solute concentration that can be reached at solvus temperature C_s is (Shercliff and Ashby, 1990):

$$C_s = A \cdot e^{-Q_s/RT_s} \tag{5-19}$$

Rearranging Eqs. (5-18) and (5-19), a new expression of the equilibrium solute concentration at ageing temperature is obtained as follows:

$$C_e = C_s \cdot e^{-\frac{Q_s}{R}\cdot\left(\frac{1}{T}-\frac{1}{T_s}\right)} \tag{5-20}$$

During the artificial ageing at elevated temperature, the supersaturation of the matrix gradually depletes due to the formation of precipitates. The precipitation kinetics can be described with Shewmon's law (Shewmon, 1963) designated in Eq. (5-21) and it reveals that the transient solute concentration in the matrix C_t decays exponentially with artificial ageing time t in the following:

$$C_t = C_e + (C_i - C_e) \cdot e^{-\frac{t}{\tau}} \tag{5-21}$$

$$\tau = k_1 \cdot t_p \tag{5-22}$$

where C_i stands for initial solute concentration, τ is a temperature-dependent constant indicating the decay speed in Eq. (5-22). k_1 is a constant and t_p represents the time to achieve the peak strength at a given temperature.

During the entire process, pre-existing precipitates, formed during ultra-fast heating, consume the alloying solute atoms and affect the subsequent artificial ageing response. The initial solute concentration C_i is redefined in Eq. (5-23) in the following:

$$C_i = C_0 - C_{pep} - C_q \tag{5-23}$$

where C_0 represents the solute concentration of the material in supersaturated solid solution state (SSSS), and C_{pep} and C_q refer to the solute concentration loss of pre-existing precipitates induced during ultra-fast heating and quenching.

To better capture the evolution of solute concentration, the format of Eq. (5-21) is revised to a differential equation:

$$\dot{C}_t = \frac{C_e - (C_0 - C_{pep} - C_{iq})}{\tau} \cdot e^{-\frac{t}{\tau}} \tag{5-24}$$

According to Eq. (5-24), the decay rate of solid solution is mainly determined by temperature-dependent parameters, C_e and τ at a given artificial ageing temperature. For a pre-deformed material, the traditional decay rate equation is no longer suitable to accurately model the evolution of solute concentration due to the effect of dislocations. The presence of dislocations decreases the activation energy of ageing and provides more nucleation sites for precipitates, which accelerates the precipitation response during artificial ageing (Birol, 2005; Myhr et al., 2015; Saito et al., 2013). Thus, a kinetic factor B_1 (controlled by dislocation density) is introduced and formulated to model the effect of pre-existing dislocations in Eq. (5-25), where the solute loss rate provided by dislocations shows a linear relationship with the normalized dislocation density. For the components without pre-strain, the normalized dislocation density $\overline{\rho}$ equals to zero, which means the decay of solute concentration is purely dominated by Shewmon's law.

$$\dot{C_{tp}} = \left(\frac{C_e-(C_0-C_{pep})}{\tau} \cdot e^{-\frac{t}{\tau}}\right) + B_1 \cdot \overline{\rho} \tag{5-25}$$

Through measurement of the solute elements dissolved in the aluminium matrix, the volume fraction of precipitates can be evaluated. To simplify the computation process, it is assumed that all precipitates have a constant chemical composition and uniform thermodynamic properties, even though the ratio of Mg to Si could be slightly different. The volume fraction of precipitates, *f*, is then directly proportional to the solute loss in the aluminium matrix $C_i - C_t$ in Eqs. (5-26) and (5-27) (Esmaeili et al., 2003a; Shercliff and Ashby, 1990; Starink and Wang, 2003).

$$\frac{f_t}{C_i-C_t} = \frac{f_e}{C_i-C_e} \tag{5-26}$$

$$\frac{f_{max}}{f_e} = \frac{C_s}{C_s-C_e} \tag{5-27}$$

where f_e represents equilibrium volume fraction of precipitates when C_i=C_e and it is the minimum value of *f* that can be obtained at a certain ageing temperature. f_{max} is the maximum possible volume fraction at absolute zero (0K), when the matrix is purely comprised of aluminium atoms.

By rearranging Eqs. (5-26) and (5-27), Eq. (5-28) is then obtained to express the volume fraction of precipitates during artificial ageing (Shercliff and Ashby, 1990).

$$f_t = f_e \cdot \frac{C_i-C_t}{C_i-C_e} = \frac{f_e \cdot C_i}{C_i-C_e} - \frac{f_e}{C_i-C_e} \cdot C_t = f_{max} \cdot \left(1 - e^{-\frac{t}{\tau}}\right) \cdot [1 - e^{-\frac{Q_S}{R}(\frac{1}{T}-\frac{1}{T_S})}] \tag{5-28}$$

Accordingly, the volume fraction of precipitates *f* is transformed into a rate form by differentiating Eq. (5-28) for accuracy and ease of computation by discretizing into a small time scale. As *f* is directly related to solute concentration variation, the kinetic factor B_1 is also introduced to quantify the corresponding volume fraction evolution as follows:

$$\dot{f_t} = -\frac{f_e}{C_i-C_e} \cdot \dot{C_t} = -\frac{f_e}{C_i-C_e} \cdot \left(\left(\frac{C_e-C_i}{\tau} \cdot e^{-\frac{t}{\tau}}\right) + B_1 \cdot \overline{\rho}\right) \tag{5-29}$$

For modelling strength evolution, the mean radius of precipitates is another important microstructural parameter. In the early stage of artificial ageing, precipitates grow rapidly with the coherency loss and structural change, and the volume fraction is increased sharply to a high level. The growth rate is subsequently reduced, resulting in the volume fraction approaching the equilibrium value gradually. This precipitation kinetic is approximated based on the classical cubic coarsening law (Shercliff and Ashby, 1990):

$$r^3 - {r_0}^3 = C_1 \cdot \frac{t}{T} e^{-\frac{Q_A}{RT}} \tag{5-30}$$

where C_1 is the coarsening constant, Q_A is the activation energy for the volumetric diffusion of atoms between particles. r is approximated as the mean radius of circular-section of precipitates through all periods of ageing. Its initial value is the radius of precipitates formed during ultra-fast heating (prior to artificial ageing). Thus, the growth rate of the radius of precipitates can be readily obtained from Eq. (5-30) and designated in the following:

$$\dot{r} = \frac{1}{3}\left(\frac{C_1 \cdot e^{-\frac{Q_A}{RT}}}{T}\right)^{\frac{1}{3}} \cdot t^{-\frac{2}{3}} \tag{5-31}$$

As mentioned above, it is found that the pre-deformed Al-Mg-Si alloys experience faster precipitation in the early stage of artificial ageing compared with non-deformed material due to the existence of dislocations. At first, the number density and the size of precipitates increase more rapidly until reaching a dynamic equilibrium, which is accompanied by a decrease of dislocation density (Kolar et al., 2012; Yin et al., 2016). When accounting for the effect of dislocations on precipitate growth, Eq. (5-31) is not accurate enough to express the coarsening rate for pre-deformed alloys as the growth rate of precipitates is proportional to the solute loss from the matrix. Similarly, the kinetic factor B_2 is adopted in Eq. (5-32) to account for the effect of dislocations.

$$\dot{r}_p = \frac{1}{3}\left(\frac{C_1 \cdot e^{-\frac{Q_A}{RT}}}{T}\right)^{\frac{1}{3}} \cdot t^{-\frac{2}{3}} + B_2 \cdot \overline{\rho} \tag{5-32}$$

The second term ($B_2 \cdot \overline{\rho}$) in Eq. (5-32) captures the accelerated precipitate growth due to dislocations. As artificial ageing proceeds, the effect of dislocations becomes weaker because

of the annihilation of dislocations at elevated temperature. Correspondingly, the contribution of the second term is reduced and a dynamic equilibrium is achieved.

$$\dot{\bar{\rho}} = -C_{ageing}\bar{\rho}^{n_3} \tag{5-33}$$

The normalized dislocation density rate can be computed by using Eq. (5-33) which is adopted from Eq. (5-5). Only the static recovery of dislocations is included in the equation because no plastic deformation is involved and thus both strain and strain rate $\dot{\varepsilon}_p$ are zero. C_{ageing} is a material constant and depends on the relationship between static recovery rate and dislocation density during heat treatment.

Figure 5.3 shows an example with the evolution of the relevant microstructural variables ($\bar{\rho}, f$ and r) for the deformed specimens (SR1, S10%) during artificial ageing at 180°C. It is simulated by using the post-form strength prediction model.

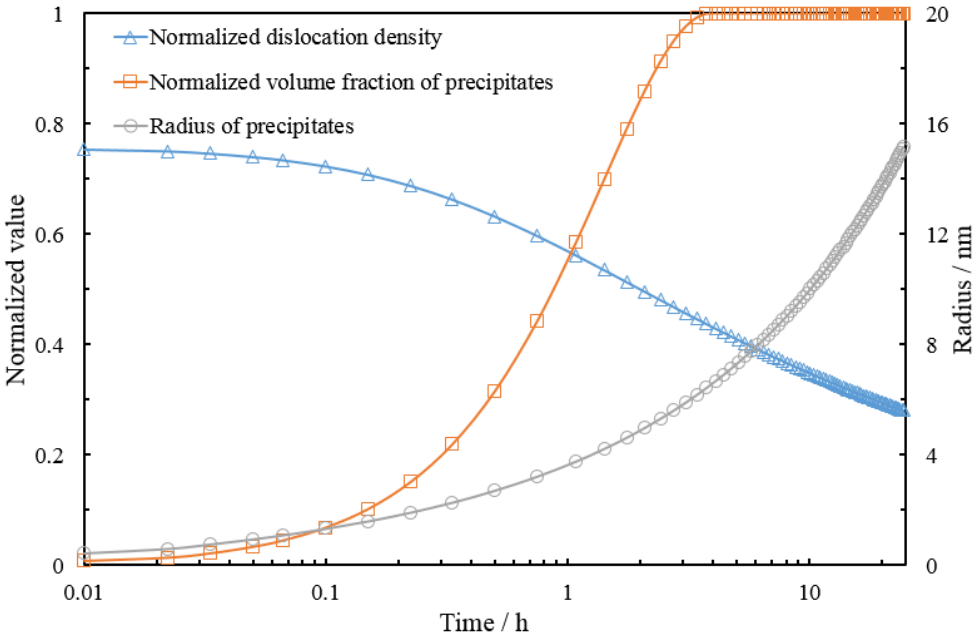

Figure 5.3: Microstructural variable evolutions during ageing (180°C, SR1, S10%)

A set of hardening equations were used to model the contribution of dislocations, solute elements, precipitates and aluminium matrix to the yield strength separately by correlating these microstructural variables. As mentioned before, the overall yield strength is the sum of each term and precipitation hardening is a mixture of weak particle hardening (shearing) and

strong particle hardening (bypassing). When the average size of particles is small, the interaction between dislocations and precipitates is dominated by particle shearing while bypassing becomes more important as the particles grow larger. The overall contribution of precipitates is designated as the harmonic mean of shearing and bypassing hardening in Eqs. (34-36) (Shercliff and Ashby, 1990). The solute atoms (including Mg, Si, Mn, Fe, Cu, etc) dissolved in the aluminium matrix provide the solid solution hardening. As a ternary alloy, Mg and Si elements are attributed to most of the hardening potential in AA6082 aluminium alloy and the contribution of solutes is summarised in Eq. (5-37) and the dislocation hardening is expressed in Eq. (5-38).

$$\sigma_{sh} = C_2 \cdot {f_t}^{1/2} \cdot r^{1/2} \tag{5-34}$$

$$\sigma_{by} = C_3 \cdot {f_t}^{1/2} \cdot r^{-1} \tag{5-35}$$

$$\sigma_{ppt} = \frac{\sigma_{by} \cdot \sigma_{sh}}{\sigma_{by} + \sigma_{sh}} \tag{5-36}$$

$$\sigma_{ss} = \sum_j k_j \cdot {C_j}^{2/3} = C_4 \cdot {C_t}^{2/3} \tag{5-37}$$

$$\sigma_{dis} = A_d \overline{\rho}^{0.5} \tag{5-38}$$

where $\sigma_{sh}, \sigma_{by}, \sigma_{ppt}, \sigma_{ss}$, and σ_{dis} represent shearable precipitate hardening, bypassing precipitate hardening, overall precipitate hardening, solid solution hardening and dislocation hardening, respectively. C_2, C_3, C_4, k_j and A_d are material constants. C_2 describes the interaction between the resistance to shear of one particle and properties of the particles (population and size); C_3 (C_3=cGb, c is a constant) is a constant used to calculate the stress required to bend a dislocation, which combines Burgers vector b and shear modulus G (Shercliff and Ashby, 1990); C_4 is a factor related to the contribution of the solute (Esmaeili et al., 2003b). C_j is the concentration of a specific alloying element and k_j is the corresponding scaling factor (Myhr et al., 2001). A_d describes the isotropic hardening due to dislocations at room temperature (Garrett et al., 2005; Zhan et al., 2011).

5.1.4 Multi-stage artificial ageing sub-model

The multi-stage artificial ageing model is established based on the idea of equivalent time, which is an important variable associating the microstructural parameters (volume fraction of precipitates and mean radius of precipitates) with the first stage ageing and the second stage ageing. Two-stage ageing is used to demonstrate the modelling approach for multi-stage ageing operations. In the two-stage artificial ageing process, the workpiece is heated to a relatively higher first-stage ageing temperature T_1 to accelerate the ageing response, followed by second-stage ageing at T_2. The solute concentration is assumed to be the same at the end of first-stage ageing as the beginning of second-stage ageing. The concept of the equivalent time $t_{eq,c}$ is introduced. This term summarises the effects of first-stage ageing at T_1, enabling the compatibility with the second-stage ageing at T_2 and ensures the consistency between artificial ageing times to be maintained. The solute concentrations when aged at different temperatures are denoted in Eqs. (5-39) and (5-40).

$$C_{t1} = C_{e1} + (C_i - C_{e1}) \cdot e^{-\frac{t_1}{\tau_1}} \tag{5-39}$$

$$C_{t2} = C_{e2} + (C_i - C_{e2}) \cdot e^{-\frac{t_2}{\tau_2}} \tag{5-40}$$

The equivalent time $t_{eq,c}$ shown in Eq. (5-42) is then computed by combining the equations above, which assumes that ageing proceeds from $t_{eq,c}$ on the ageing curve for temperature T_2.

$$C_{t1} = C_{t2} \tag{5-41}$$

$$t_{eq,c} = t_2 = -\tau_2 \cdot \ln\left(\frac{C_{e1} - C_{e2}}{C_i - C_{e2}} + \frac{C_i - C_{e1}}{C_i - C_{e2}} \cdot e^{-\frac{t_1}{\tau_1}}\right) \tag{5-42}$$

Consequently, the solute concentration during the second-stage ageing is represented by Eq. (5-43):

$$C_{t2} = C_{e2} + (C_i - C_{e2}) \cdot e^{-\frac{t + t_{eq,c}}{\tau_2}} \tag{5-43}$$

where t is the time of second-stage ageing.

In the multi-stage ageing process, the average radius of precipitates does not change abruptly when the temperature changes. In order to model precipitate growth, the radius is assumed to remain unchanged during the transition between different stages of ageing, which is illustrated in Eqs. (5-44) and (5-45).

$$r_1 = r_2 \tag{5-44}$$

$$\frac{t_1}{T_1} e^{-\frac{Q_A}{RT_1}} = \frac{t_2}{T_2} e^{-\frac{Q_A}{RT_2}} \tag{5-45}$$

As shown in Eq. (5-46), the equivalent time $t_{eq,r}$ is introduced to represent the radius of precipitates in the second-stage ageing and the classical cubic coarsening kinetic is accordingly modified as Eq. (5-47).

$$t_{eq,r} = t_2 = \frac{T_2}{T_1} \cdot e^{\frac{Q_A}{RT_2} - \frac{Q_A}{RT_1}} \tag{5-46}$$

$$r_2{}^3 - r_0{}^3 = C_1 \cdot \frac{t + t_{eq,r}}{T} e^{-\frac{Q_A}{RT_2}} \tag{5-47}$$

With increased artificial ageing temperature, the precipitation rate and equilibrium solute concentration increase while the equilibrium volume fraction drops. Precipitates are assumed to have a constant chemical composition, hence the volume fraction of precipitates is proportional to the solute loss from the aluminium matrix. For the multi-stage ageing process, the solute concentration and volume fraction of precipitates after first-stage ageing are set as C_x and f_x, generating Eqs. (5-48) and (5-49) below:

$$\frac{C_i - C_x}{f_x} = \frac{C_x - C_t}{f_t - f_x} \tag{5-48}$$

$$f_t = \frac{C_i - C_t}{C_i - C_x} \cdot f_x \tag{5-49}$$

where f_t, C_t are the corresponding values in the second-stage ageing.

5.1.5 Particle size distribution (PSD) sub-model

The developed PFS model (with four sub-models abovementioned) is capable of predicting post-form strength of the components during FAST and subsequent heat treatment through the correlation of three key microstructural parameters: solute concentration, volume fraction of precipitates and mean radius of precipitates. However, it is challenging to accurately interpret the microstructural evolutions such as predicting the nucleation phenomenon and capturing the size distribution of precipitates. Based on the classic KWN microstructure model (Kampmann et al., 1985), the particle size distribution (PSD) sub-model is established with consideration of the effect of residual dislocations, which is an important supplement to the PFS model. The key computation principles are to classify the precipitates by size and track the size evolution of each class during the entire forming process. The nucleation, growth and coarsening of precipitates are no longer independent processes and are interrelated at different stages of artificial ageing.

$$j = j_0 \exp\left(-\frac{\Delta G^*_{het}}{RT}\right) \exp\left(-\frac{Q_d}{RT}\right) \tag{5-50}$$

$$\Delta G^*_{het} = \frac{(A')^3}{(RT)^2[\ln(C_t/C_e)]^2} \tag{5-51}$$

Eq. (5-50) describes the nucleation rate j in the precipitation process (Russel, 1970). The energy barrier for nucleation is expressed in Eq. (5-51) (Myhr et al., 2004). j_0 is the pre-exponential term of nucleation, ΔG^*_{het} is the energy barrier for nucleation, Q_d is the activation energy of diffusion, A' is the energy barrier constant, C_t is the solute concentration in the matrix, C_e is equilibrium solute concentration.

The presence of residual dislocations generated during high temperature plastic deformation facilitates the nucleation process by providing more nucleation sites for the precipitates, which means the conventional nucleation equations need to be modified by considering the effect of dislocations. Thus, a kinetic factor B_3 is introduced to model the effect of dislocations on the precipitation as shown in Eq. (5-52). Based on the TEM observations, it was found that the nucleation rate is highly dependent on the artificial ageing temperature. Eq. (5-53) shows that the pre-exponential nucleation term is corrected as a temperature dependent parameter.

$$j_0 = j_0' + B_3 \cdot \bar{\rho} \tag{5-52}$$

$$j_0' = j_{00}' \exp(Q_j / RT) \tag{5-53}$$

where j_0 is the modified pre-exponential nucleation term, j_0' is the initial pre-exponential nucleation term at non-deformation condition, B_3 is the material parameter characterising the acceleration effect of residual dislocations on the nucleation process, $\bar{\rho}$ is the normalised dislocation density and Q_j is the activation energy.

Nucleation is the first stage of the precipitation process with a significant amount of solute atoms precipitate from the aluminium matrix in the beginning. The nucleation rate decreases sharply when the driving force provided by the concentration difference approaches to zero (solute concentration in the matrix C_t = the equilibrium solute concentration C_e). The number density of precipitates exhibits an increasing trend until coarsening becomes the dominant mechanism. The precipitates coarsen to single large precipitate when exposed to an elevated temperature for a sufficiently long time. The related evolutions of nucleation rate and number density of the material aged at 220°C are shown in Figure 5.4:

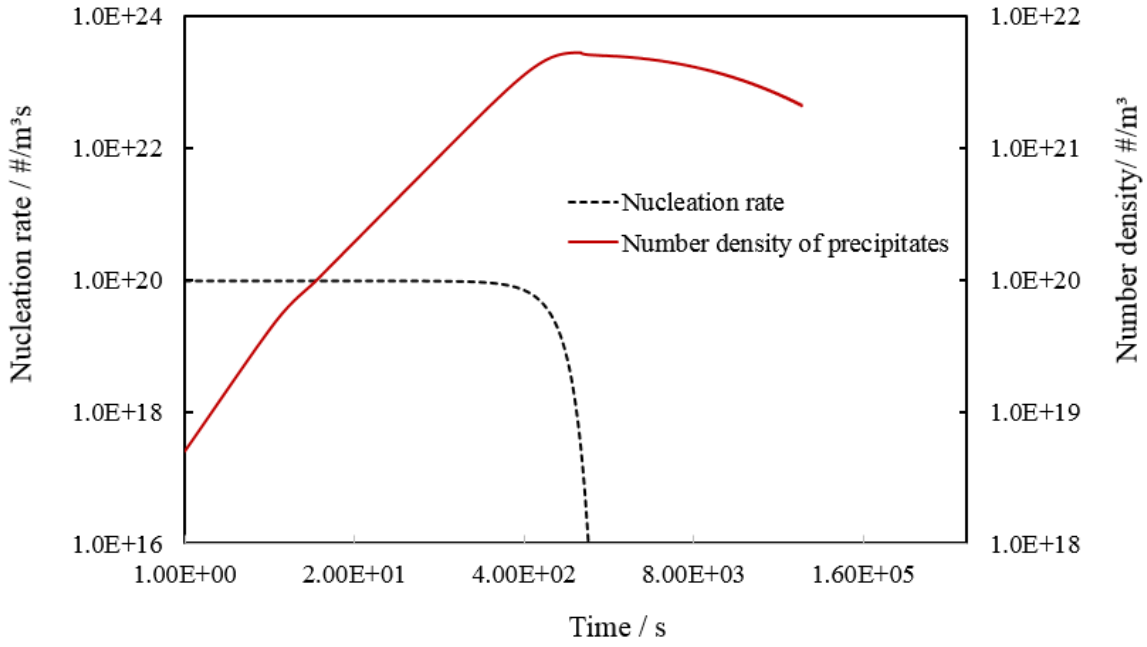

Figure 5.4: Evolutions of nucleation rate and number density during the artificial ageing at 220°C

Based on the assumption that the stoichiometry of the precipitates are identical, the growth rate of the precipitate $\dot{r}$ is calculated by Eq. (5-54) (Kampmann et al., 1985).

$$\dot{r} = \frac{C_t - C_{int}}{C_{sp} - C_{int}} \frac{D}{r} \tag{5-54}$$

where C_{int} is the solute concentration at the precipitate/matrix interface, C_{sp} is the concentration of a specific element inside the precipitates and D is the diffusion coefficient. The value of C_{sp} is set as one in the computation as Si and Mg elements are considered to evenly contribute to formation of the precipitates and the difference in stoichiometry is neglected. Thus, Eq. (5-54) is refined as Eq. (5-55).

$$\dot{r} = \frac{C_t - C_{int}}{1 - C_{int}} \frac{D}{r} \tag{5-55}$$

As analysed in Section 4.2, the presence of residual dislocations not only accelerates the nucleation rate during the early stage of artificial ageing, but also plays a vital role in the growth and coarsening stages as the required activation energy of bulk diffusion is reduced. Therefore, the diffusion is subdivided into bulk diffusion and dislocation core dislocation and the kinetic factor B_4 is introduced to quantify the dislocation effect. The conventional Arrhenius equation to compute diffusion coefficient is modified by Eqs. (5-56) to (5-58).

$$D = D_{diff} + B_4 \cdot D_{dis} \cdot \bar{\rho} \tag{5-56}$$

$$D_{diff} = D_0 \cdot \exp\left(\frac{-Q_{diff}}{RT}\right) \tag{5-57}$$

$$D_{dis} = D_0 \cdot \exp\left(\frac{-Q_{dis}}{RT}\right) \tag{5-58}$$

where D_{diff} and Q_{diff} are the diffusion coefficient and activation energy for bulk diffusion while D_{dis} and Q_{dis} are for the dislocation core diffusion coefficient. B_4 is the factor to quantify the dislocation effect on the growth of precipitates.

The interface concentration is related to equilibrium concentration through the Gibbs-Thomson equation as described in Eq. (5-59) (Aaron et al., 1970).

$$C_{int} = C_e \cdot \exp(\frac{2\gamma V_m}{rRT}) \tag{5-59}$$

where γ is the precipitate-matrix interface energy and V_m is the molar volume of the precipitates.

In the growth and coarsening processes, some of the small precipitates will dissolve in the matrix and provide atoms for the growth of the larger ones. The precipitates that will grow are determined by whether their radius is greater than the critical radius (Kampmann et al., 1985). From Eq. (5-55), it is indicated that the term $(1 - C_{int})$ is always greater than 1, which means C_t should equal to C_{int} at the critical condition. Then Eq. (5-60) is obtained by substituting C_{int} with $C_e \cdot \exp\left(\frac{2\gamma V_m}{rRT}\right)$ and rearranging the equation. r_c is the critical radius determining a precipitate that neither will grow nor shrink.

$$r_c = \frac{2\gamma V_m}{RT}(\ln(\frac{C_t}{C_e}))^{-1} \tag{5-60}$$

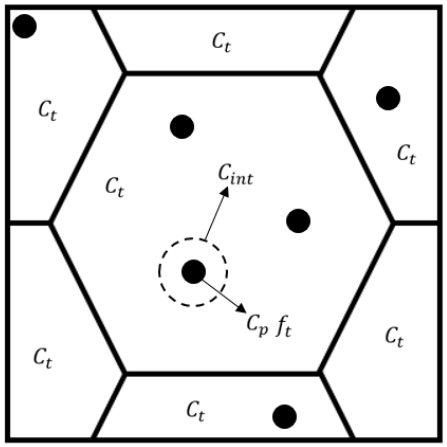

Figure 5.5: Schematic diagram about the relationship between solute concentration and volume fraction

Figure 5.5 shows the relationship between solute concentration and volume fraction. Based on the assumption that the total solute concentration C_0 is the sum of solute concentration in the aluminium matrix C_t and solute concentration in the precipitates C_p, Eq. (5-61) is obtained.

$$C_t = C_0 - C_p \cdot f_t \tag{5-61}$$

Volume fraction f_t is the sum of the fraction of precipitates in each discrete size class.

$$f_t = f_0 \sum \frac{4}{3} \pi {r_i}^3 N_i \tag{5-62}$$

where N_i and r_i are the number and mean radius of precipitates in a specific radius class within a certain volume and f_0 is the pre-exponential factor to adjust the volume fraction f_t to the scale of entire testing material under computation. The number and radius of precipitates N_i and r_i in each class are calculated by Eqs. (5-50) and (5-55) during each time interval and recorded for the computation in the next iteration.

5.2 Calibration of the PFS model

The unified PFS model couples five sub-models: flow-stress, quenching, artificial ageing, multi-stage artificial ageing and PSD models. The flow-stress sub-model describing the mechanical behaviour of the material was calibrated using the results of uniaxial tensile tests. Artificial ageing sub-model considering effects of pre-existing precipitates and residual dislocations was calibrated with the results of ultra-fast heating and pre-straining tests. Calibration of the quenching and multi-stage artificial ageing sub-models that act as supplements to the main AA sub-model were conducted as well. Similar work was performed for the PSD sub-model by using ageing results and microstructure observations. The order of the calibration procedure is: calibration of flow stress sub-model → artificial ageing sub-model → quenching and multi-stage AA sub-models (supplement to the AA model) → PSD sub-model.

Each parameter in the unified PFS model represents a physical characteristic of the material and was determined based on the parameter boundary conditions presented in the literature and optimised by using an advanced Simulated Annealing (SA) algorithm with details presented in the following chapter. With regard to the viscoplastic deformation sub-model, the boundaries of material parameters are referred to the literature (Wang et al., 2017). In the artificial ageing model, the universal gas constant is 8.314 J/mol K, and intrinsic strength σ_i is measured through hardness tests. Q_A, Q_s and T_s are referred to the literature (Myhr et al., 2001; Shercliff and Ashby, 1990). C_i, C_s and f_{max} are read from the phase diagram which is obtained by inputting

the chemical composition of the material into a computational material software "Thermo-Calc". Quenching parameters T_C, Q_0 and Q_q are acquired from a continuous cooling precipitation diagram. Based on the size of the precipitates statistically counted from extensive TEM images of the specimens deformed to certain strain levels and artificial aged at elevated temperatures, B_1 and B_2 are calibrated. C_2, C_3, C_4, n_2, A_d, C_{ageing} are optimised with simulated annealing (SA) algorithm against the experimental results. The details of calibration procedures are outlined in the flow chart in Figure 5.6.

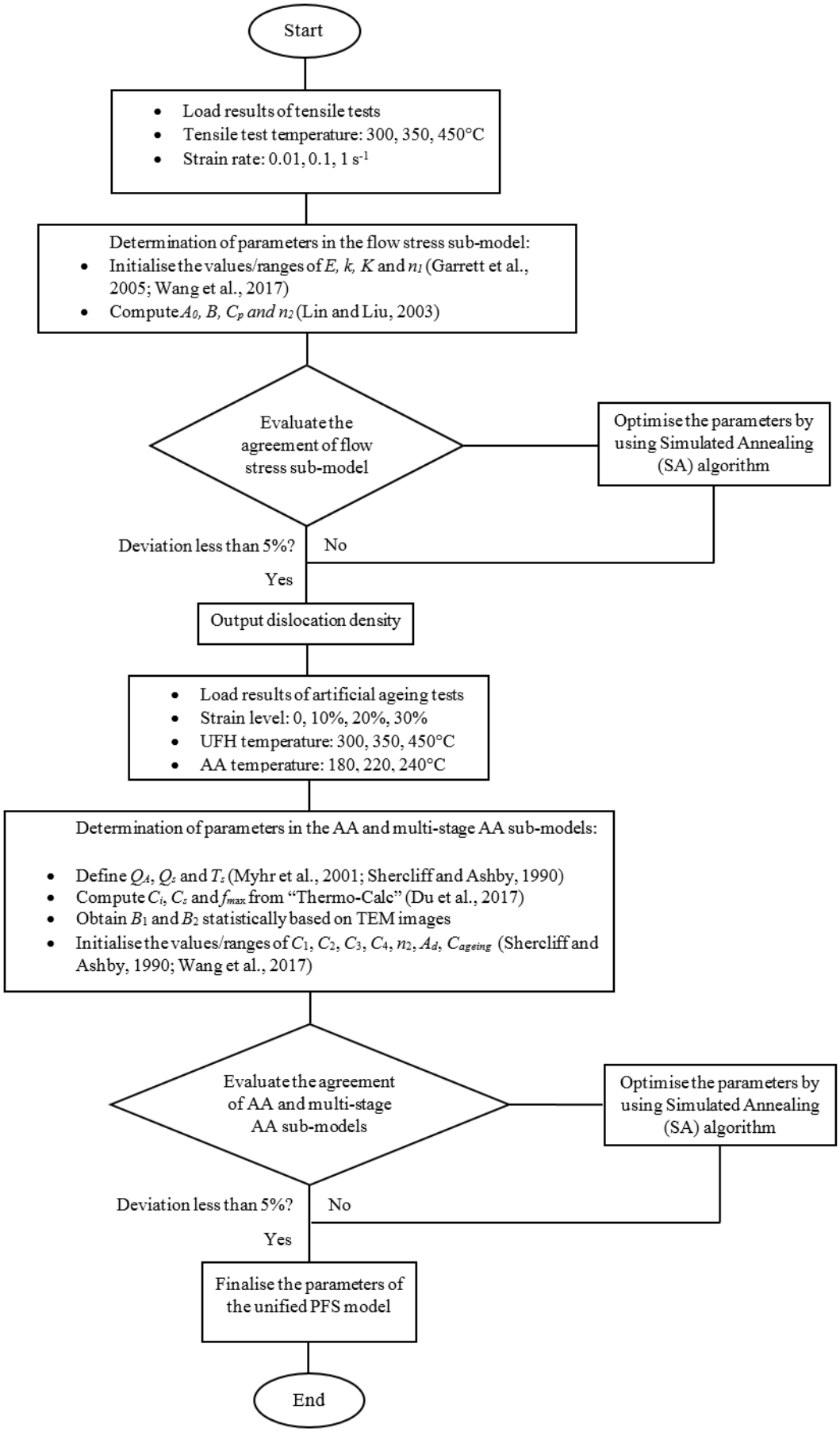

Figure 5.6: The methodology to obtain the parameters in the unified PFS model

5.2.1 Calibration of the flow stress sub-model

The calibrated values of material parameters for the flow stress sub-model are presented in Table 5.1 and the comparison between measured and modelled stress-strain curves of AA6082 is illustrated in Figure 5.7.

Table 5.1: Material parameters of the flow stress sub-model

E_0 (MPa)	K_0 (MPa)	k_0 (MPa)	B_0 (MPa)	n_{10}
13211	1.2	0.14	0.118	3.9
A_0	C_p	Q_E (kJ/mol K)	Q_K (kJ/mol K)	Q_k (kJ/mol K)
0.75	15	6520	19223	13856
Q_B (kJ/mol K)	Q_{n_1}(kJ/mol K)	$Q_{A_{00}}$(kJ/mol K)	Q_{C_p} (kJ/mol K)	n_2
30498	2050	12421	-21986	3.5

(a)

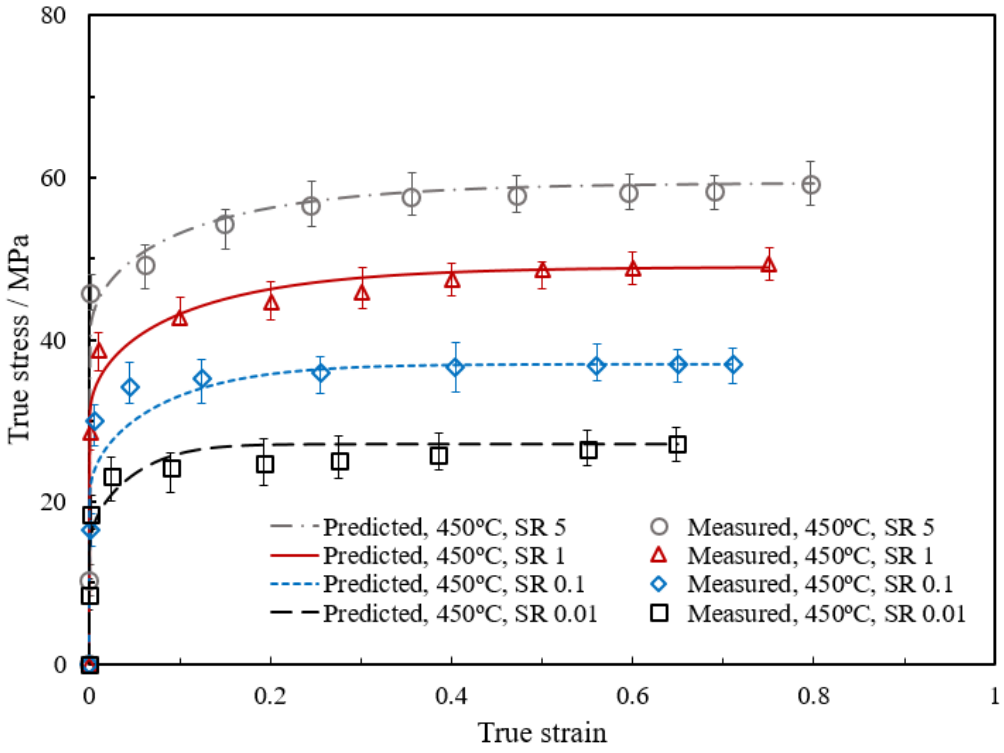

(b)

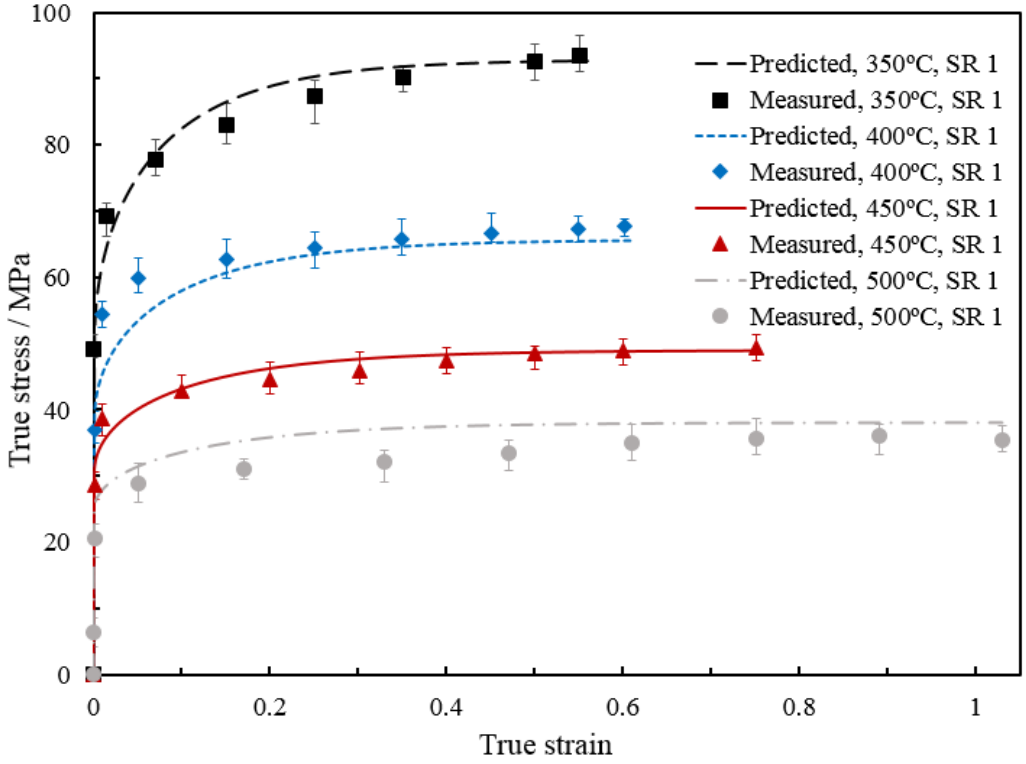

Figure 5.7: The measured and modelled stress-strain curves of AA6082 (a) at different strain rates and (b) at different temperatures

Figures 5.7. (a) and (b) show the stress-strain curves of AA6082 deformed at a constant temperature with different strain rates and a constant strain rate with varying temperatures, respectively. The symbols in the figure represent the experimental data and the solid line refers to the modelling results. The modelling results fit very well with the experimental ones for all experimental conditions within acceptable accuracy.

5.2.2 Calibration of the quenching, artificial ageing and multi-stage artificial ageing sub-model

Table 5.2 shows calibrated material parameters of quenching, artificial ageing and multi-stage artificial ageing sub-models. The related calibration results are presented in Figures 5.8-5.11.

Table 5.2: Material parameters of the artificial ageing and quenching sub-models

Q_0 (kJ/mol K)	Q_q (kJ/mol K)	R (kJ/mol K)	C_0	σ_i (HV)
5.06E-60	6.76E5	8.314	0.025	15
Q_s (kJ/mol K)	T_s (K)	C_s	k_1	B_1
25	553	0.0263	0.5	7.8E-07
$f_{\max}$	C_1	Q_A (kJ/mol K)	B_2	C_{ageing}
1.95E-3	4.5E-3	140	1.5E-13	0.0005
n_2	C_2	C_3	C_4	A_d
5	380	1.35E6	0.077	17

The comparisons between the experimental and modelled hardness values for the ageing at different temperatures without pre-strain are given in Figure 5.8. It can be clearly seen that the model captures the general trend and the peak hardness values with a deviation of less than 5%. The best fit can be observed for the 180°C curve and this is advantageous as this temperature yields the most optimum value of the post-form strength.

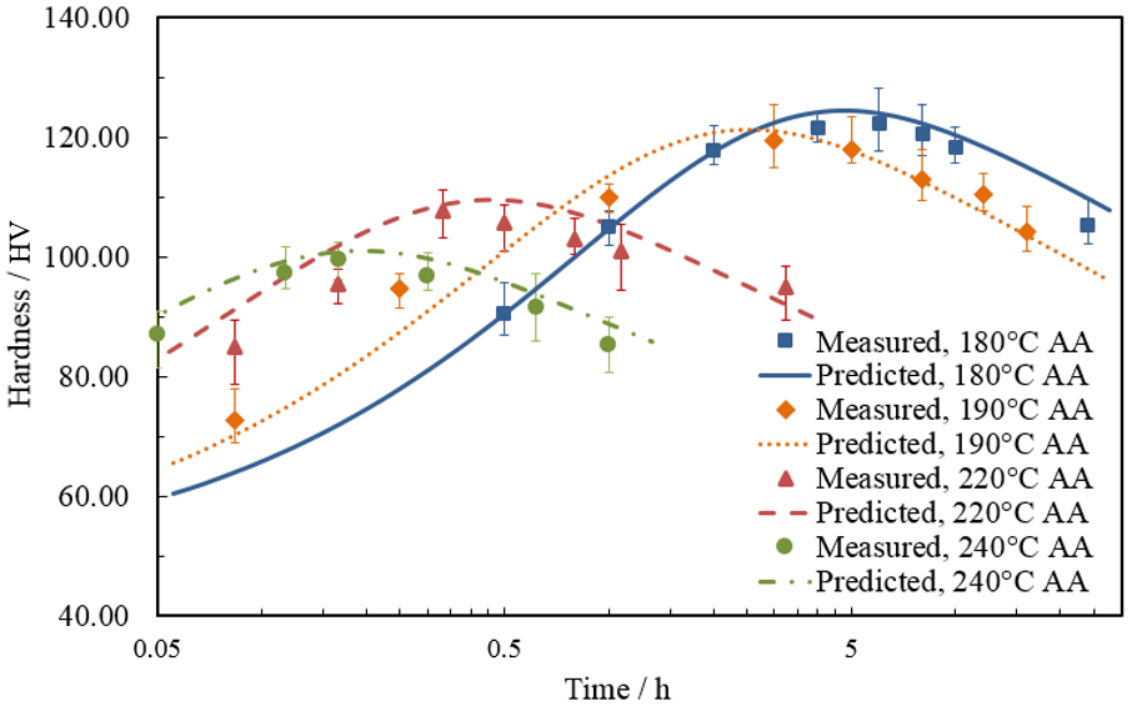

Figure 5.8: Comparison between the experimental results and model predicted hardness for the specimens aged at different temperatures

Figure 5.9 illustrates the comparisons between the experimental and modelled hardness values for ageing at 180°C with different target heating temperatures. This ageing temperature value (180°C) was chosen as it gave the highest strength and the best model fit in Figure 5.8. The evolutions of the normalized volume fraction of precipitates, $\overline{f}$, are displayed in Figure 5.10. All three curves increase sharply in the early stages of ageing, slowing in the latter stages and eventually levelling out to 1 at the end of ageing. The normalized volume fraction of the specimen heated to 350°C is greater than that of the ones heated to 300 and 450°C in the early stages of ageing. The results are consistent with the proposed theory in Section 4.1 and verified by TEM and hardness measurements.

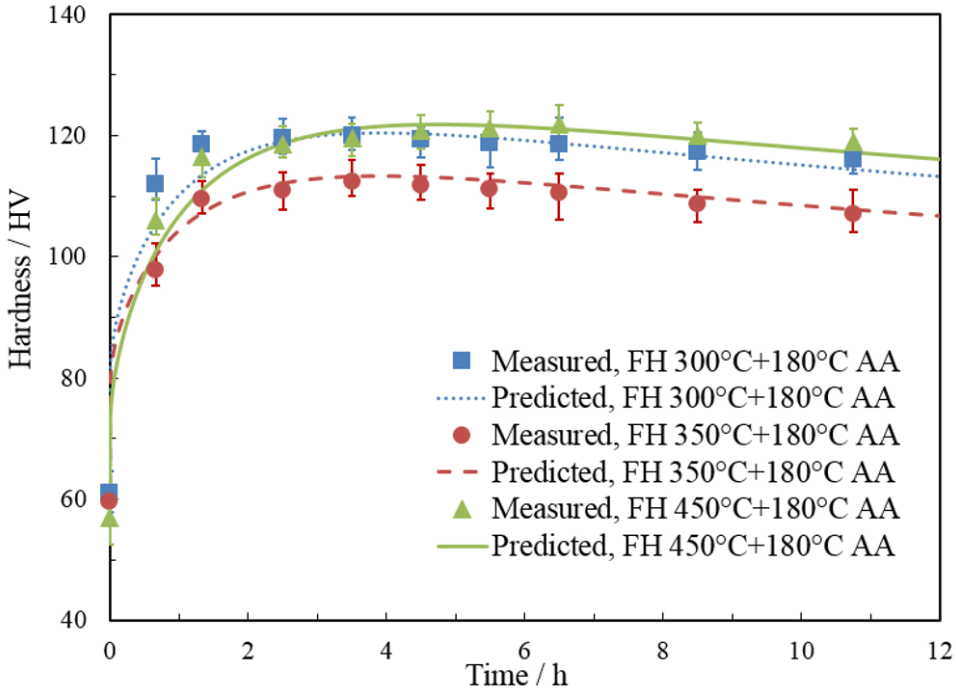

Figure 5.9: Comparison between the experimental results and the modelled hardness for the specimen aged at 180°C ageing with different target heating temperatures.

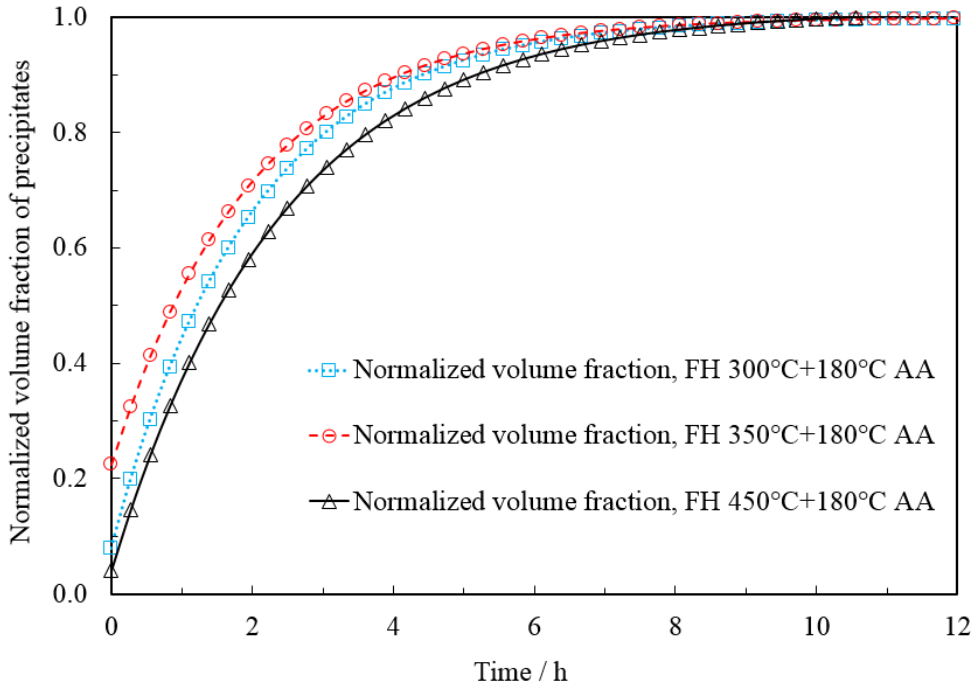

Figure 5.10: Volume fraction evolutions for the specimens aged at 180°C with different target temperatures

The hardness evolutions for ageing at 180°C with different amounts of pre-strain and strain rates are shown in Figure 5.11.

(a)

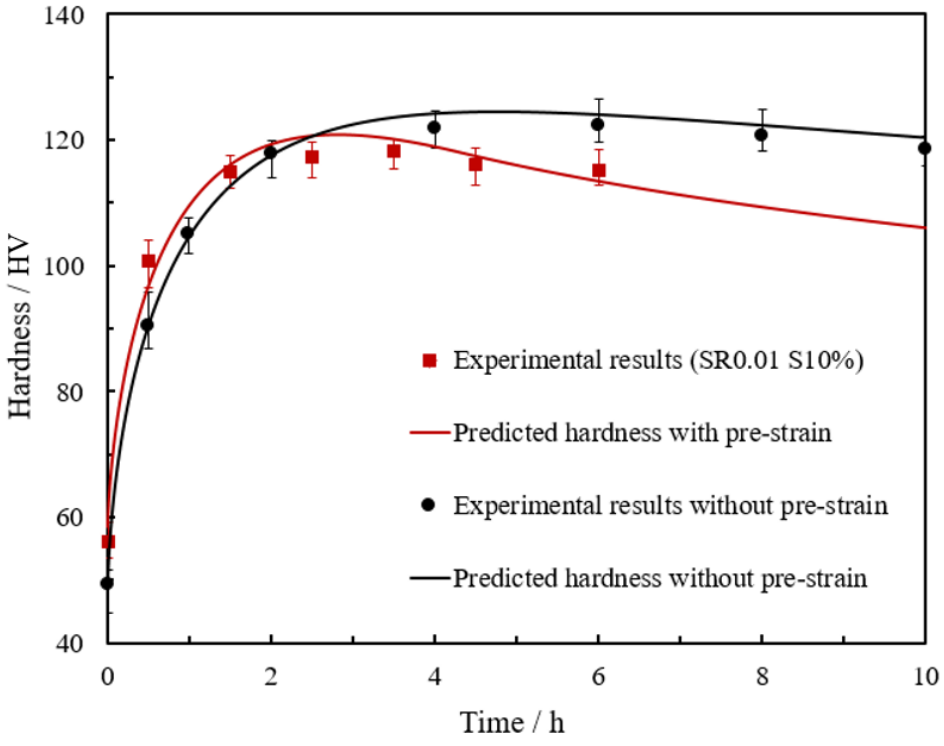

(b)

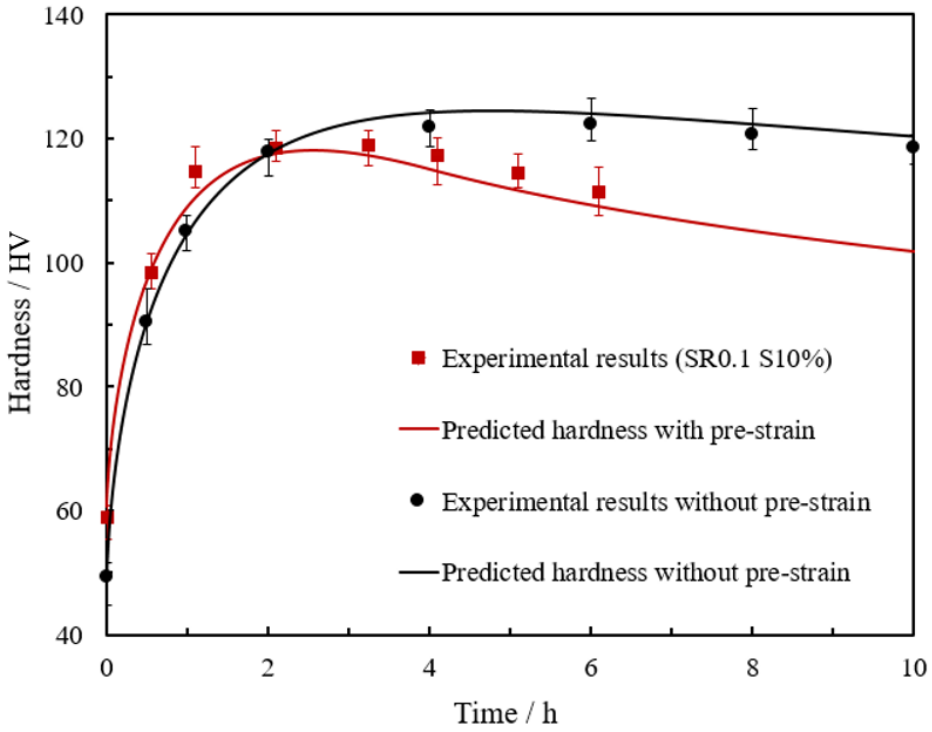
Hardness / HV
Time / h
Experimental results (SR0.1 S10%)
Predicted hardness with pre-strain
Experimental results without pre-strain
Predicted hardness without pre-strain

(c)

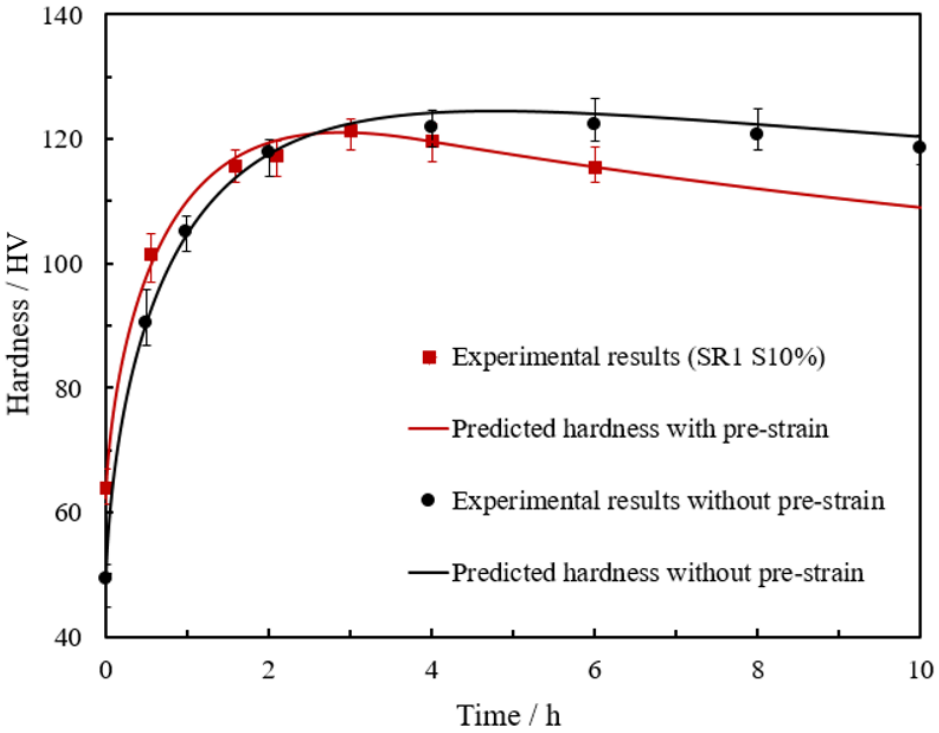
Hardness / HV
Time / h
Experimental results (SR1 S10%)
Predicted hardness with pre-strain
Experimental results without pre-strain
Predicted hardness without pre-strain

(d)

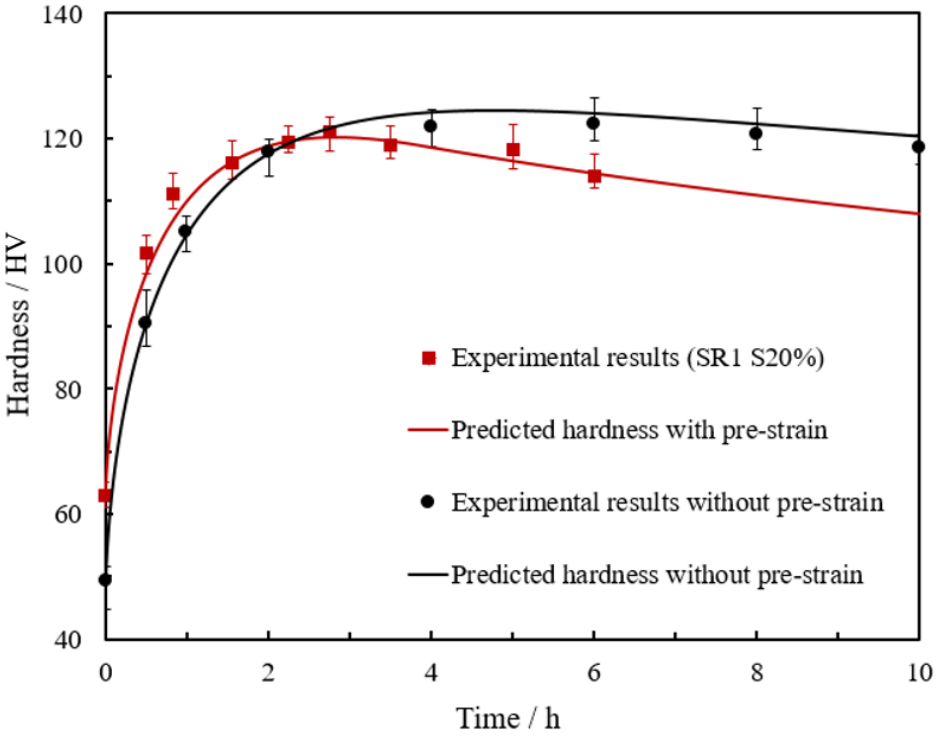

(e)

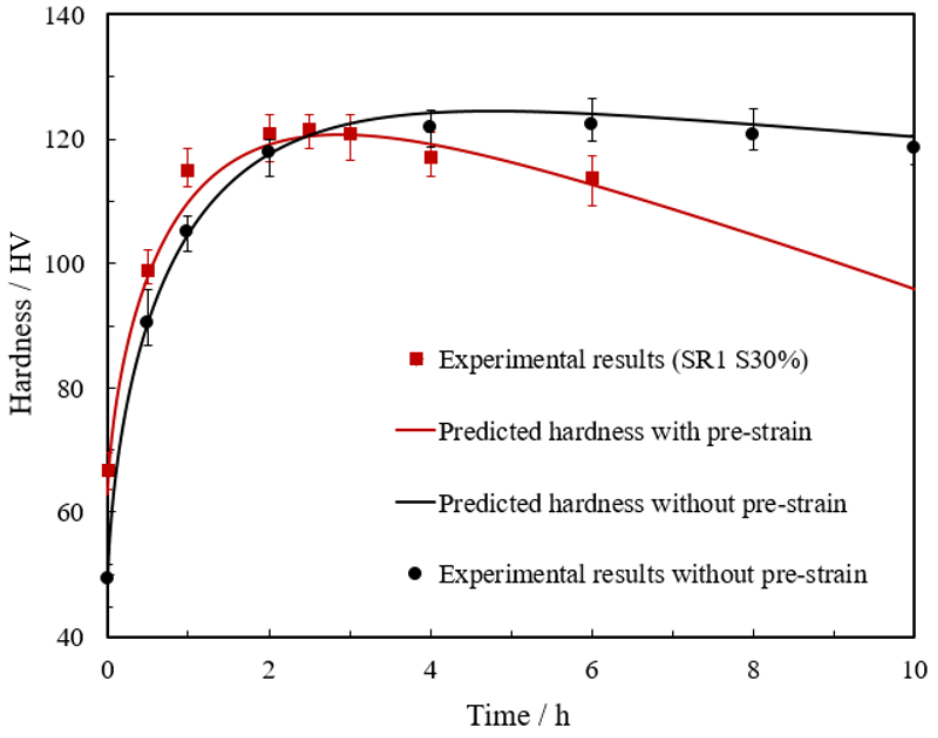

Figure 5.11: Comparison between the experimental results and the modelling of hardness evolution for the specimens with different amounts of pre-strain and strain rate (a) SR 0.01s^{-1}, Strain 10%, (b) SR 0.1s^{-1}, Strain 10%, (c) SR 1s^{-1}, Strain 10%, (d) SR 1s^{-1}, Strain 20% and (e) SR 1s^{-1}, Strain 30%

As shown in the figure, a good agreement between the modelled results and experimental ones is obtained with the majority of the modelled curves (produced by using the equations in Section 5.1.3) within the error bars of the experiments. The difference between the predicted results and the experimental data is less than 5%, which means the model accurately captures the hardness evolution during the artificial ageing process. Furthermore, the hardness for the pre-strained specimens increases steeply during the early stage ageing and decreases rapidly than that of the non-deformed specimens. This is because the induced dislocations accelerate the artificial ageing response.

The calibration results of quenching sub-model are demonstrated in Figure 5.12.

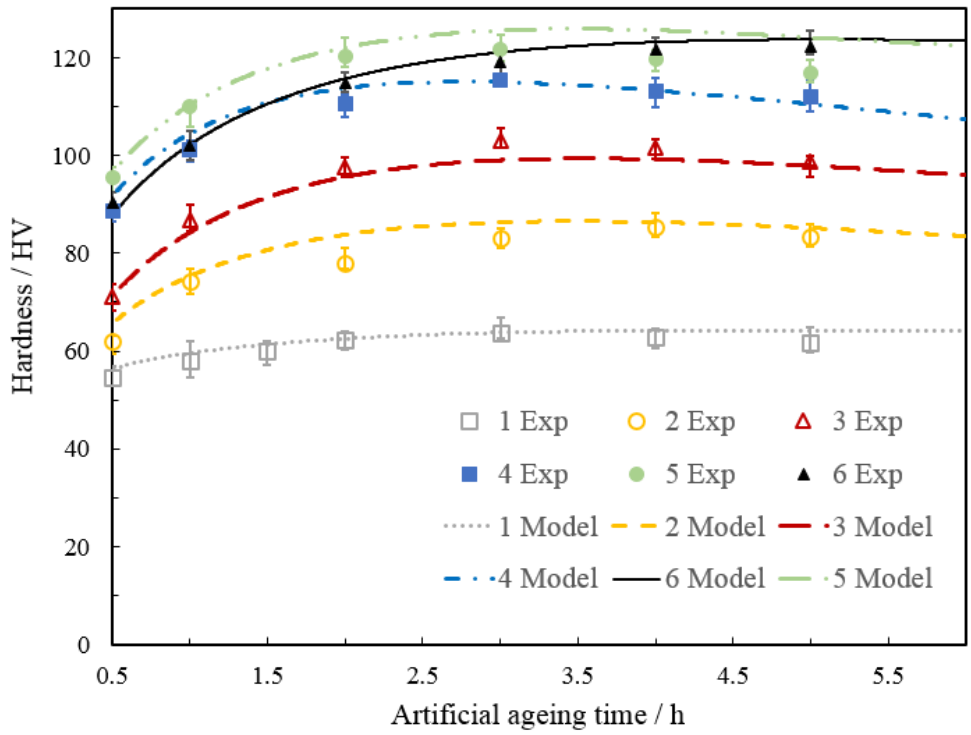

Figure 5.12: Comparison of hardness between experimental data and modelling results for the specimens during 180°C artificial ageing

An excellent agreement between the experimental data and model can be noted. The difference between the PFS prediction model and experimental results is less than 7%. The experimental hardness for specimen 2 in the initial stage of artificial ageing lies slightly outside the error bars. Specimen 6 is the sample quenched by air at a rate over the required critical quenching rate, which shows a slightly different artificial ageing response. In summary, the unified PFS model incorporated with quenching sub-model is capable of predicting the strength of insufficiently quenched components.

The comparative results of the multi-stage artificial ageing are shown in Figure 5.13. While the first stage ageing lies slightly outside the error bar region of the experiment, the majority of the second stage ageing is within the region. This confirms that the model is capable of modelling complex two-stage ageing phenomena, at different temperatures, and can incorporate the evolving microstructures.

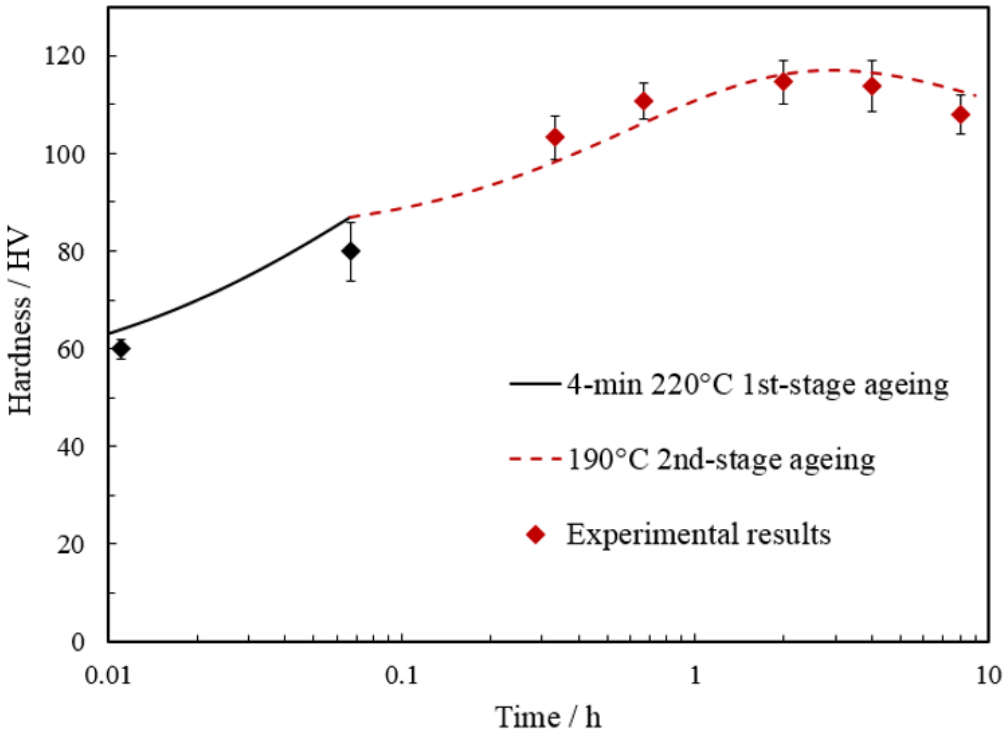

Figure 5.13: Comparison between the experimental and the modelled hardness evolution for the specimen after two-stage ageing

5.2.3 Calibration of the particle size distribution (PSD) sub-model

The methodology to calibrate material parameters in the PSD sub-model is similar to that for the unified PFS model as outlined in Figure 5.6, with the exception of calibrating the volume fraction and mean radius of precipitates during the ageing process. More than 50 bright-field TEM images in each testing condition were statistically analysed to obtain the values of these microstructural variables.

Table 5.3: Material parameters of the extended PFS model

Q_d (kJ/mol K)	B_3	j'_{00} (#/m^{3}s)	Q_j (kJ/mol K)	B_4
1.30E+05	9.50E+34	1.07E+25	-8.38E+04	3.37 E-04
D_0 (m^2/s)	Q_{diff} (kJ/mol K)	Q_{dis} (kJ/mol K)	γ (kJ/m^2)	V_m (m^3/mol)
2.21E-03	1.38E+05	1.05E+05	0.20	3.95E-05

Figure 5.14 illustrates the predicted evolution of the critical radius and the comparison of the mean radius of precipitates between measured and simulated values for the specimen undergoing artificial ageing at 180°C.

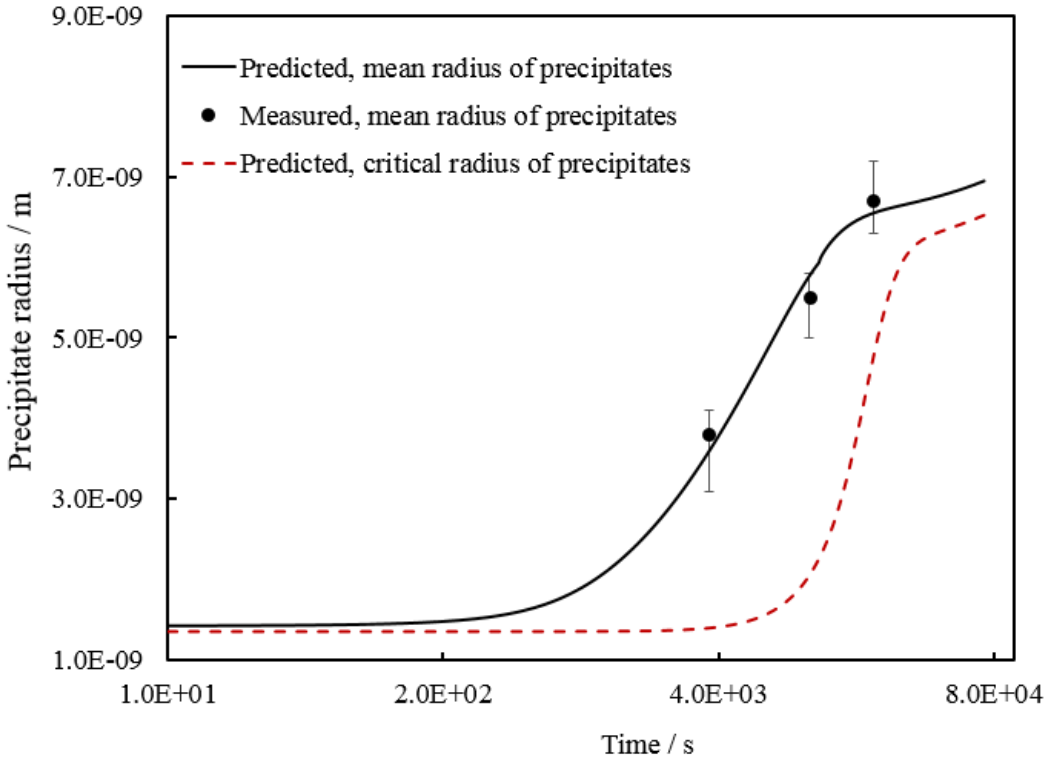

Figure 5.14: Comparison between the experimental and the modelled radius revolution for the specimen artificially aged 180°C

From Figure 5.14, it is deduced that the difference between the mean radius and the critical radius is increased rapidly at the early stage due to the large driving force provided for nucleation and growth. Once precipitation enters the coarsening stage, the difference narrows with ageing time. The black solid curve in the figure represents the mean radius of precipitates predicted by using the PSD sub-model while the symbols represent the mean radius statistically counted from hundreds of TEM images. The error bars of the specimen aged for 1 hour are

slightly larger than the remained as the growth of precipitates in the early stage ageing is not uniform, resulting in relatively larger deviation. Generally, the predicted results show good accuracy with all the symbols lying within the error bars.

The advanced function of the PSD sub-model is to provide comprehensive microstructural results during the artificial ageing process, including the distributions of precipitates in discrete size.

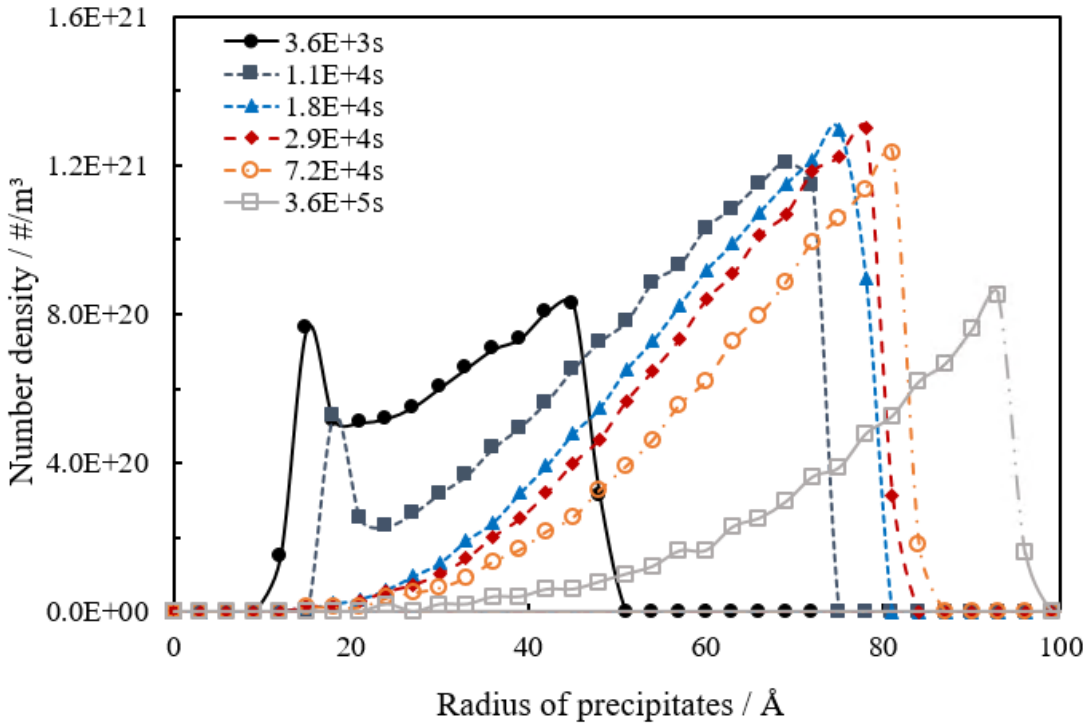

Figure 5.15: Predicted precipitates size distribution of the specimen artificially aged at 180°C (1 Å = 0.1nm)

Figure 5.15 is an example of precipitate size distribution predicted by running the PSD sub-model for the specimen isothermally artificially aged at 180°C. The simulated artificial ageing time ranges from 1 hour to 100 hours. As seen in Figure 5.15, the radius of precipitates increases and the number density keeps decreasing as artificial ageing proceeds. Additionally, it is found that number density curves for 1 hour and 4 hours artificial ageing have a peak prior to 2 nm whereas all the other curves only have peaks at larger radius (>7 nm). The reason is the nucleation rate of precipitates is still very high leading to the occurrence of a great deal of small precipitates with approximately 2 nm radius. These precipitates in small size either grow

larger or dissolve in the matrix after the nucleation process is completed and thus the first peak in the size distribution curve disappears.

5.3 Summary

The unified PFS model incorporating flow stress, quenching, artificial ageing, multi-stage artificial ageing and particle size distribution (PSD) sub-models was successfully developed based on the comprehensive microstructural investigations and rigorous theoretical studies.

The developed PFS model was calibrated using the results of the ultra-fast heating tests, uniaxial tensile tests, pre-straining uniaxial tensile tests, quenching tests, artificial ageing tests and multi-stage artificial ageing tests. The modular designed PFS model offers good flexibility for strength and microstructure prediction of the specimens under various testing conditions and allows for potential upgrades. The functionality of the PFS model has been proved and its advanced applications will be presented in the following chapter.

Chapter 6. Applications of the PFS model

This chapter presents the applications of the developed PFS model. In order to evolve the theoretical model into practical applications and enhance the efficiency and usability accordingly, an advanced functional module 'Tailor' was developed. 'Tailor' incorporates both the PFS prediction model and the automatic calibration function, enabling efficient calibration of the PFS model and accurate prediction of the material strength. The constructed predictive functional module was utilised in conjunction with FE simulation software, such as PAM-STAMP and Autoform. Furthermore, the module was embedded into a cloud based FEA platform.

6.1 Development of the functional module 'Tailor'

The FAST process involves ultra-fast heating, immediate stamping, rapid quenching and multi-stage artificial ageing. It is a tailored process and each stamped component requires a set of unique processing windows. Prediction of the post-form strength of the material following these process stages is extremely challenging due to the numerous processing parameters involved that need to be considered. Therefore, a series of rigorous experiments were conducted to investigate the underlying mechanisms during the entire FAST process. The findings were analysed and utilised to establish the unified PFS model, which has been proved as a powerful tool to predict strength and microstructure evolutions of Al-Mg-Si alloys during the FAST process.

In order to evolve the PFS model into practical applications and also improve its efficiency and usability, an advanced functional module 'Tailor' was developed. This advanced functional module follows the same structure of the PFS model (modular design with several sub-models) and encompasses an automatic calibration function to optimise material parameters. Simulated Annealing (SA) algorithm was selected to construct the calibration function.

This chapter is based on the paper work:

"Yang, X., Zhang, Q., Zheng, Y., Politis, D.J., Wang, L., Development of the interactive friction model for lubricant breakdown at elevated temperature utilising a SA-based optimisation scheme, Tribol. Int. Under review."

"Zhang, Q., Ji, K., El Fakir, O., Liu, X., Wang, L., 2016. Determination of Processing Windows for the Hot Stamping of AA7075, Key Eng. Mater. 716, 402–412."

Two programming languages, Microsoft Visual Basic and MATLAB were used to develop this functional module for offline and online computations, respectively. VB version Tailor provides an offline compiled executable file with user-friendly interfaces which allows users to predict strength evolution of the formed components and optimise processing windows independently and locally in the case of working without Internet connection. Figure 6.1 is the operation interface of the offline version 'Tailor'. MATLAB version Tailor was implemented in a cloud based FEA platform and can be easily updated and cooperated with other available functional modules in a cloud environment, of which detailed information is shown in Appendix B.

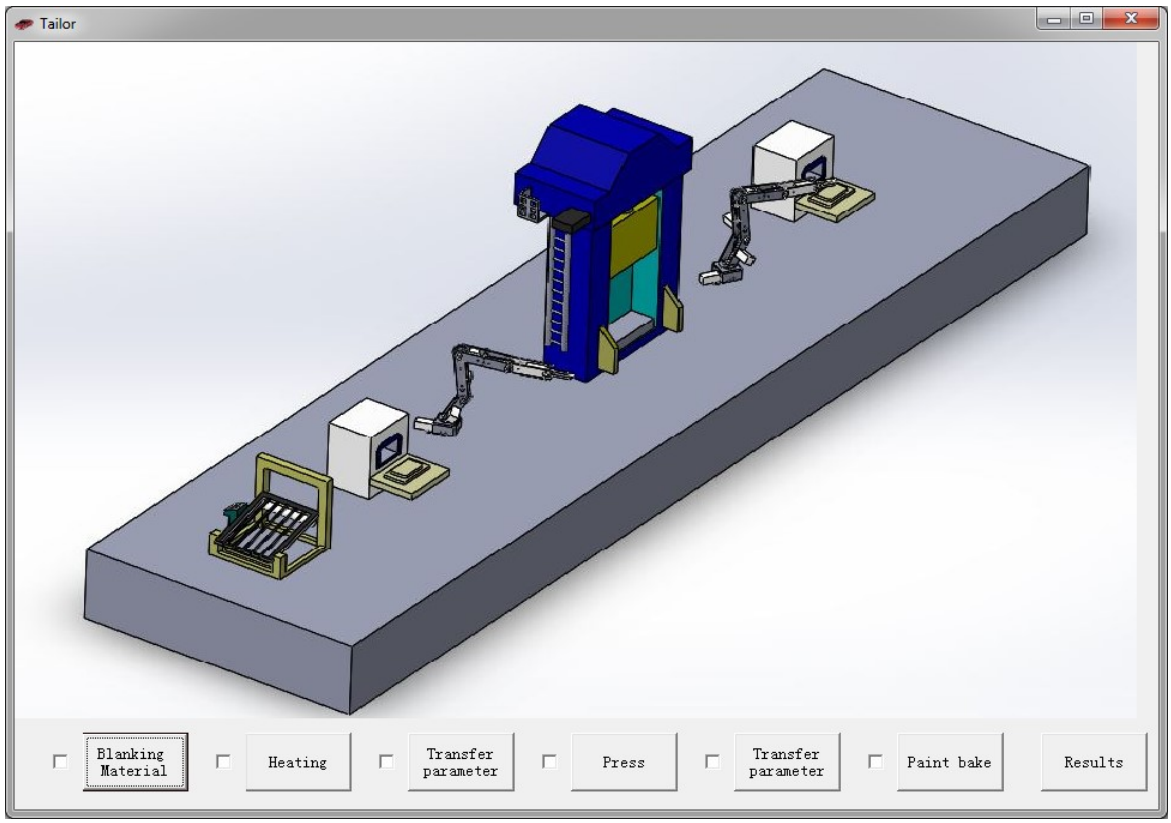

Figure 6.1: Interface of the offline version 'Tailor' programmed by using Microsoft Visual Basic

The post-form strength distribution of a component at certain conditions can be visualised in FE simulation software by integrating the 'Tailor' module in the cloud based FEA platform to post-process the FE data. Figure 6.2 illustrates the workflow of development and implementation of Tailor to the cloud based FEA platform.

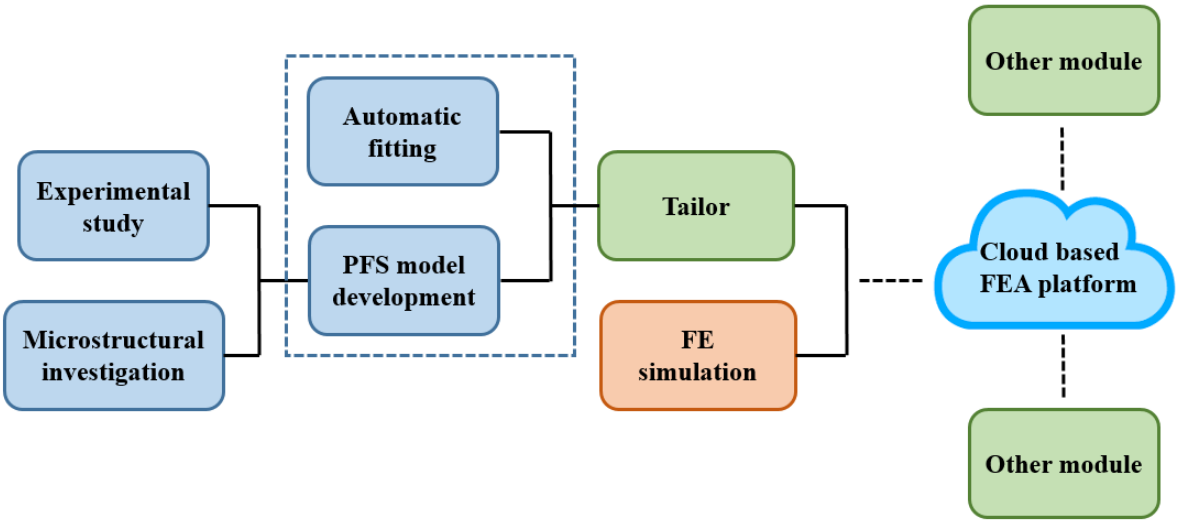

Figure 6.2: Workflow of the development and implementation of online version 'Tailor'

Details of the experimental study and microstructural investigation were presented in Chapters 3 and 4. The framework of the unified PFS model was demonstrated in Chapter 5. This section focuses on the development of Tailor, and in particular the algorithm used for automatic fitting.

Given the complexity of the PFS model which consists of 61 equations and more than 100 parameters, the manual calibration of the model is obviously time-consuming and inefficient. Of the 100+ parameters, 43 material parameters must be fitted based on the pre-defined boundaries. Most of these to-be-fitted parameters have specific physical meaning and the boundaries are well-documented in the literature or easily measurable, such as activation energies, Young's modules and intrinsic strength of aluminium matrix. However, some parameters (including pre-exponential constant for threshold stress and solute hardening constant) are highly dependent on the batch of the material with relatively broader ranges and change greatly with variation in the chemical composition of the material. Thus, it is essential to select an intelligent method to automatically calibrate the material parameters within pre-defined boundaries to save computational and storage resources as well as to improve the calibration accuracy.

The calibration of material parameters is essentially an optimisation process once a proper cost/fitness/objective function is confirmed, which aims to evaluate the performance of the selected parameters. To calibrate the PFS model, the fitness function is defined as the mean

square deviation between experimental results and the predicted values. The target of the calibration therefore is minimising the cost of the fitness function.

Existing optimisation methods are broadly classified into two categories: gradient optimisation and derivative free optimisation (Conn et al., 2009; Koziel and Yang, 2011). Gradient optimisation searches the minimum of a fitness function based on the evaluation of gradients. The derivative free optimisation is the technique that converges to a global optimum for non-differentiable and potentially discontinuous problems without estimating gradients. The computation cost of derivative free method is significantly greater than gradient method, although they are more robust when assessing local minima and searching for the global minima. In this case, one typical derivative free optimisation method, simulated annealing (SA) algorithm is selected to automatically calibrate the PFS model. The details of the SA algorithm including the flow chart of the mechanism are outlined in Appendix A.

The advantage of SA is that it allows the algorithm to explore a wide search space for a global minima. This means the probability of identifying a local minima as opposed to a global minima is greatly reduced (Rere et al., 2015). The only limitation of the SA algorithm is that the initial solution *S* is required to be near a local minima of the fitness function, otherwise the optimisation efficiency may be poor. The reason to utilise the SA method for optimising the material parameters of the PFS model is that the boundaries are well defined, as they are constrained by physical limitations and chemical composition of the material. As long as all the parameters are within the pre-defined ranges, the initial state of material parameters for different 6xxx Al-Mg-Si alloys is treated as a solution near the local minima. The model calibration is to minimise the deviation between modelled results and experimental data which can be fulfilled by the SA algorithm.

The efficiency and accuracy of the SA algorithm has been demonstrated through a case study. In the current case study, the artificial ageing sub-model of the unified PFS model was automatically calibrated against experimental results by running the SA optimisation algorithm. Experimental hardness evolutions of the specimens artificially aged at different temperatures were obtained as introduced in Section 3.5. Activation energy Q_A, solvus boundary enthalpy Q_s and solvus temperature T_s were referred to the literature (Myhr and Grong, 2000; Shercliff and Ashby, 1990). Initial solute concentration C_i, maximum solute concentration C_s and

maximum volume fraction of precipitates f_{max} were computed by using the material software 'Thermo-Calc'. Values of the other material parameters were initialised within the corresponding certain boundaries. The step of automatic calibration was set as 1000 and the calibration process was completed in 20 minutes. The calibration results at different steps were recorded and plotted in Figure 6.3.

(a)

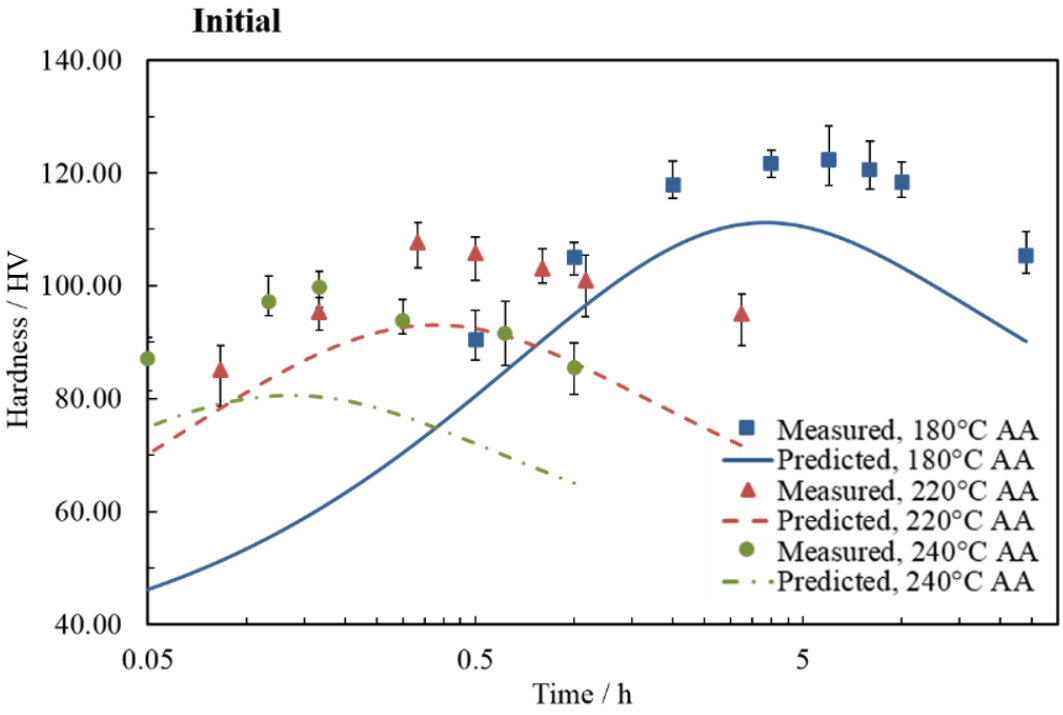

(b)

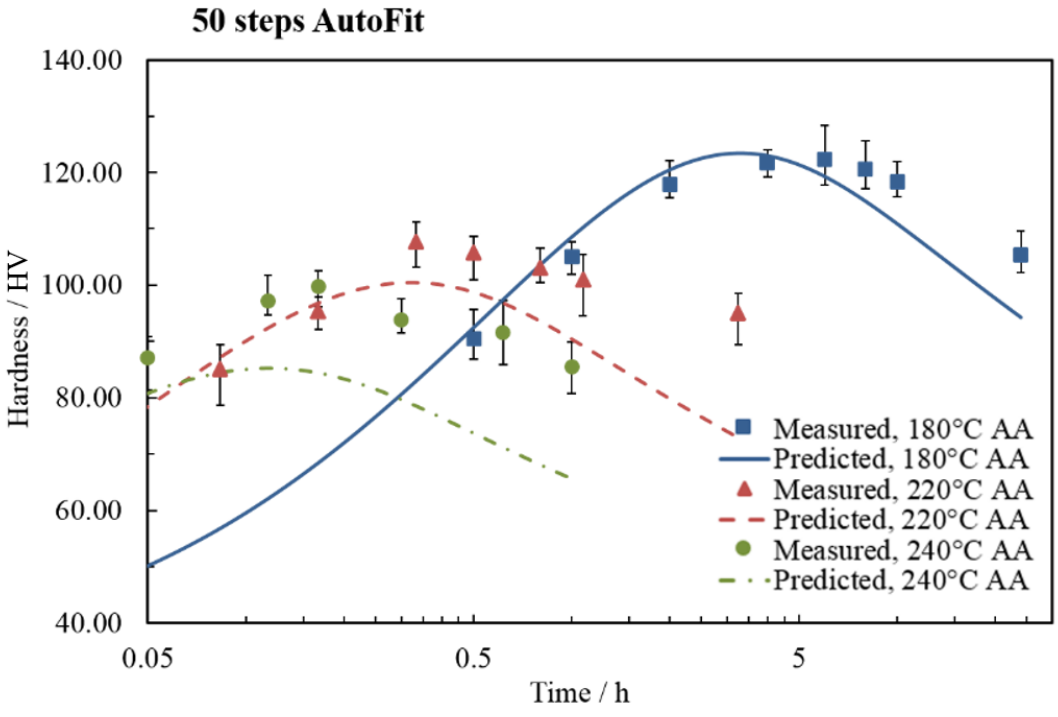

(c)

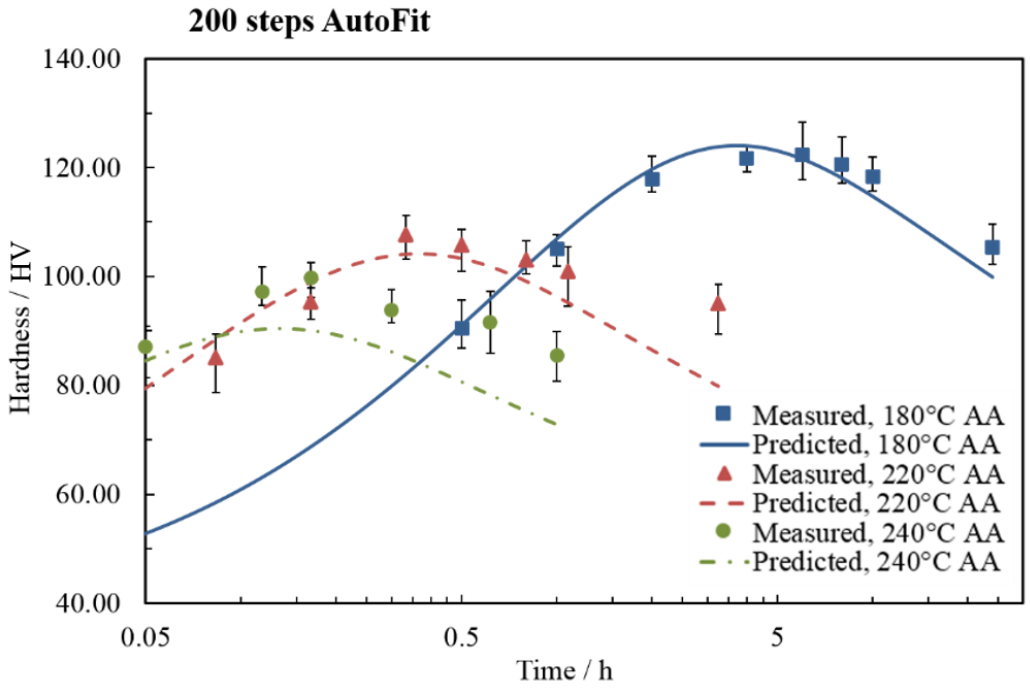

(d)

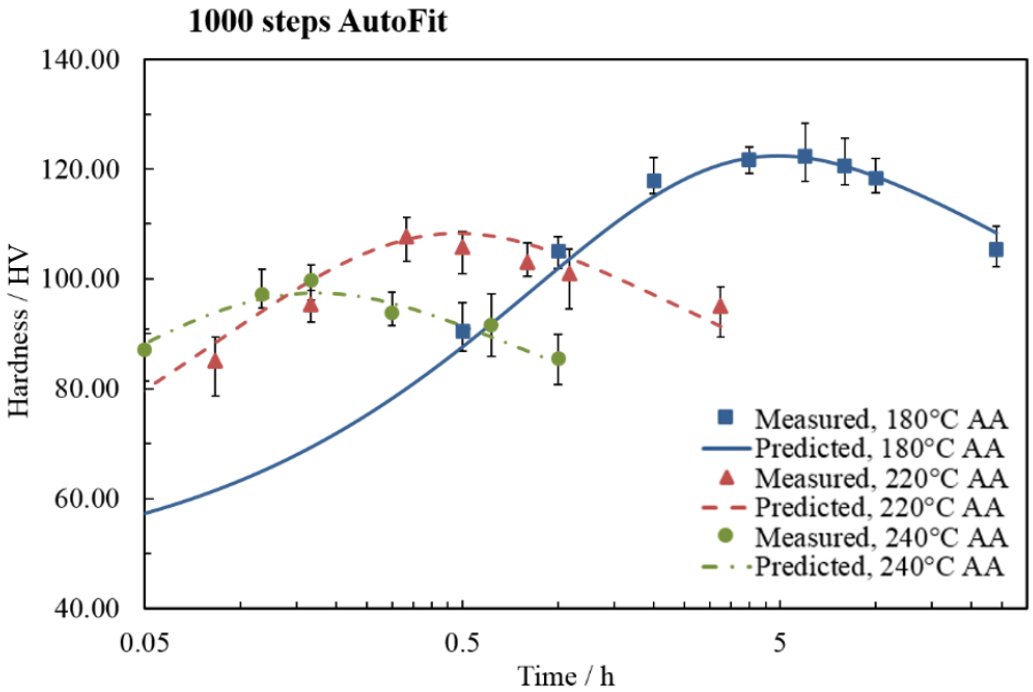

Figure 6.3: Evolution of automatic calibration results of AA sub-model (a) initial state before optimisation, (b) 50 steps of AutoFit, (c) 200 steps of AutoFit and (d) 1000 steps of AutoFit

The deviation between experimental results and modelled data was 23.7% before running the SA algorithm and it decreased to 9.6%, 6.3% and 3.9% after 50, 200 and 1000 AutoFit steps,

respectively. The automatic calibration of the AA sub-model was completed in 20 minutes and the deviation was reduced by 19.8%, which proves the SA algorithm is efficient and accurate.

With the PFS model and automatic calibration function embedded, the developed functional module 'Tailor' is able to predict the post-form strength of 6xxx aluminium alloy components accurately and efficiently.

6.2 Implementation of 'Tailor' to the cloud based FEA platform

Conventional FE simulation software packages such as Autoform and PAM-STAMP are widely used to model sheet metal forming processes. However, a comprehensive study of forming processes such as forming limit prediction and post-form strength prediction can only be conducted by integration of subroutines, which requires extensive expertise and are tailored to the specific FE software. Furthermore, the developed subroutines can only be run locally, and computation process would be computationally expensive and time-consuming. Therefore, it is promising to develop and implement the advanced functional modules in the cloud based FEA platform to enhance the capability of the FE simulation software and realise online simulation at low computational cost simultaneously. 'Tailor' is one of the function modules that have been implemented in the platform.

Functional module 'Tailor' is designed to post-process FE simulation results and then predict strength evolution of the entire component that would be comprised of thousands of elements. The module consists of the PFS model and automatic calibration function and itself has been automatically self-calibrated against experimental results prior to being implemented. Once the module is compiled in the platform, it is able to be used in a cloud environment. The workflow of 'Tailor' is demonstrated in Figure 6.4.

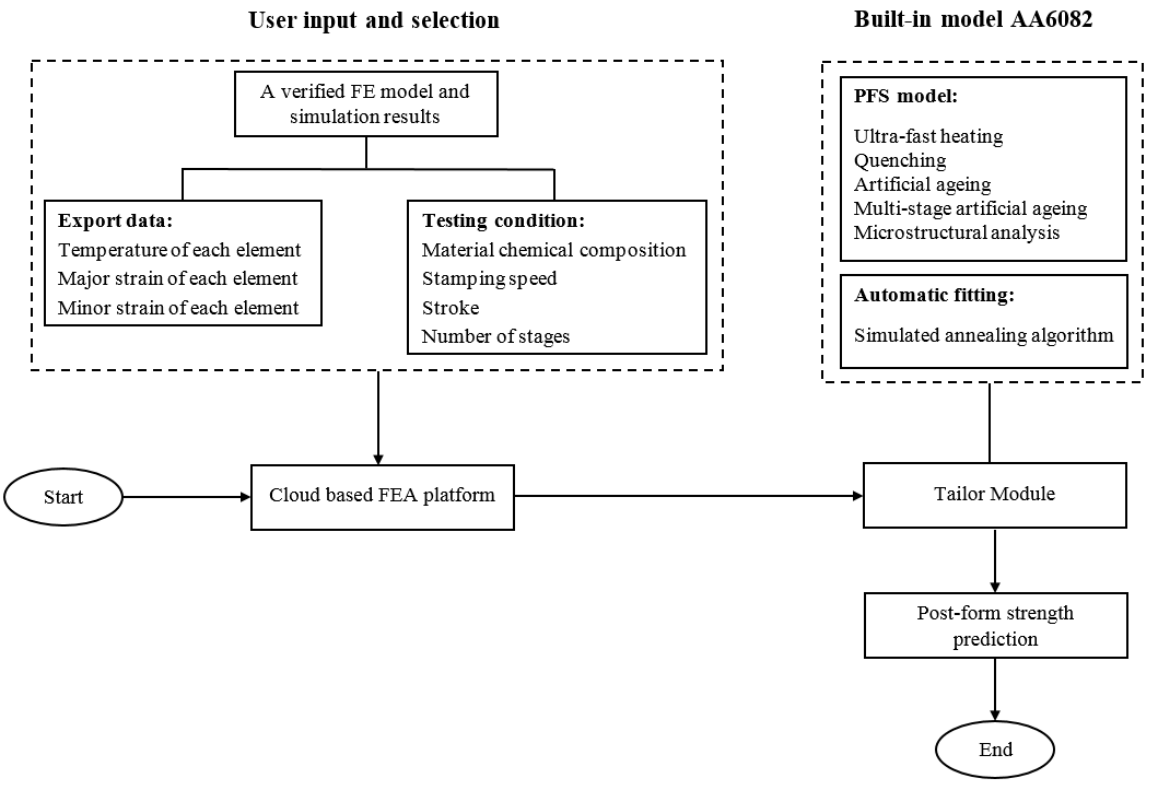

Figure 6.4: Workflow of functional module – 'Tailor'

The operation of 'Tailor' has five major procedures:

(1). Create verified FE models and export important simulation data (user-end)

Validated FE models are developed in conventional FE software packages such as PAM-STAMP and Autoform where the utilised parameters are determined on the basis of experimental trials. Simulation results for all the elements including histories of temperature, major strain and minor strain at each simulation stage together with forming conditions are exported from FE software and compressed into a .zip file.

(2). Connect to the cloud platform and select the appropriate function module (user-end)

Cloud based FEA simulation platform is then connected and the appropriate functional module is required to be selected. In this research, 'Tailor' is selected to predict the strength evolution (microstructure evolution is optional) of the components during post-form heat treatment.

(3). Input required information and submit the job (user-end)

As shown in Figure 6.5, there are six sub-modules in Tailor and users are required to input the initial workpiece parameters and processing windows. 'Blank' module requires the information of the blank material such as blank size and chemical composition, 'Heating' module specifies

the heating condition prior to forming process, ‘Transfer’ module computes the transfer time and temperature drop from the furnace to the press, ‘Press’ module defines the forming parameters and reads the .zip file of simulation results, ‘Unload’ module checks the unloading details after the components are formed and ‘Paint bake’ module determines the paint bake cycle conditions. After the required information of all six sub-modules has been completed, a summary page is presented asking the user to final check the input information. Once the information is confirmed and FE simulation results are uploaded into the online platform, the job will be assigned into a queuing system awaiting computation.

(4). Complete the computation (platform-end)

In the cloud system, the workpiece parameters and processing windows are read from the job detail and the required simulation results are extracted from the compressed file. The workload of the job is estimated by the system and the input information is then assigned to four clusters with 8GB memory allocation for the online computation.

(5). Send feedback of the job back to users (platform-end)

Once the post-form strength computation is completed, the results are sent back to the users’ account and can be downloaded freely. It is worth mentioning that ‘Tailor’ module can be used simultaneously with other available function modules to analyse different features of the forming process if needed.

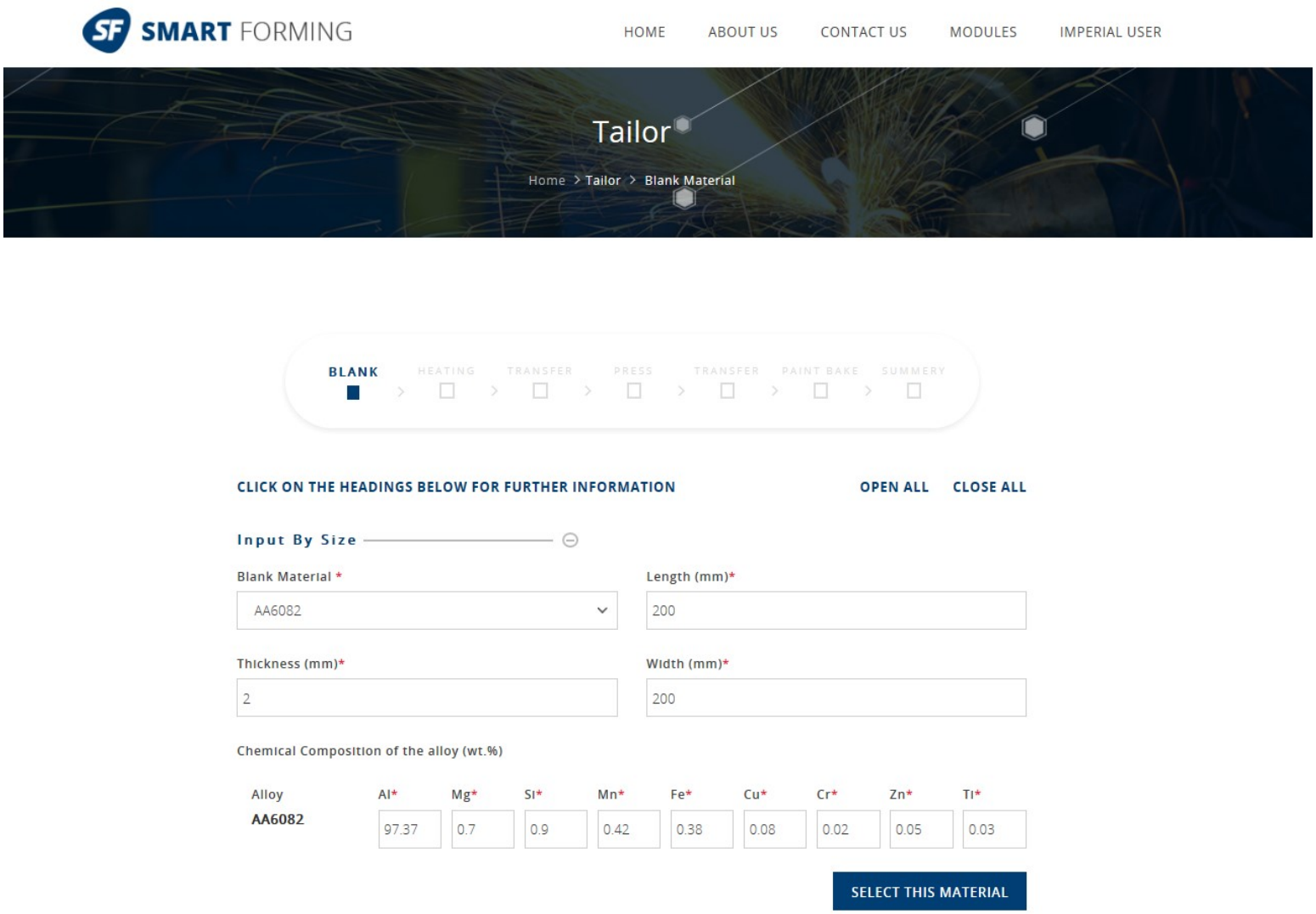

Figure 6.5: 'Blank' sub-module of 'Tailor' in the cloud based FEA platform

6.3 Case study

The robustness of the developed functional module 'Tailor' was demonstrated through the case study of a U-shaped AA6082 component formed by FAST.

As described in Section 3.6, the T4 temper sheet blank was formed via the automated pilot production line. The sheet blank was loaded on the conveyer system and transferred to the contact furnace for ultra-fast heating. Once the target forming temperature 450°C (heating rate is 50°C/s) was reached, the blank was transferred to the forming tools and deformed immediately. After in-die quenching was performed, the system conveyed the formed components to the incubation chamber for paint bake cycles, where the temperature inside the chamber was maintained at 180°C. The forming trials were repeatedly conducted with identical processing windows and the formed parts were soaked for different periods of time between 0 and 4 hours. After incubation, the formed parts were trimmed to the final shape as shown in Figure 6.6.

(a) (b)

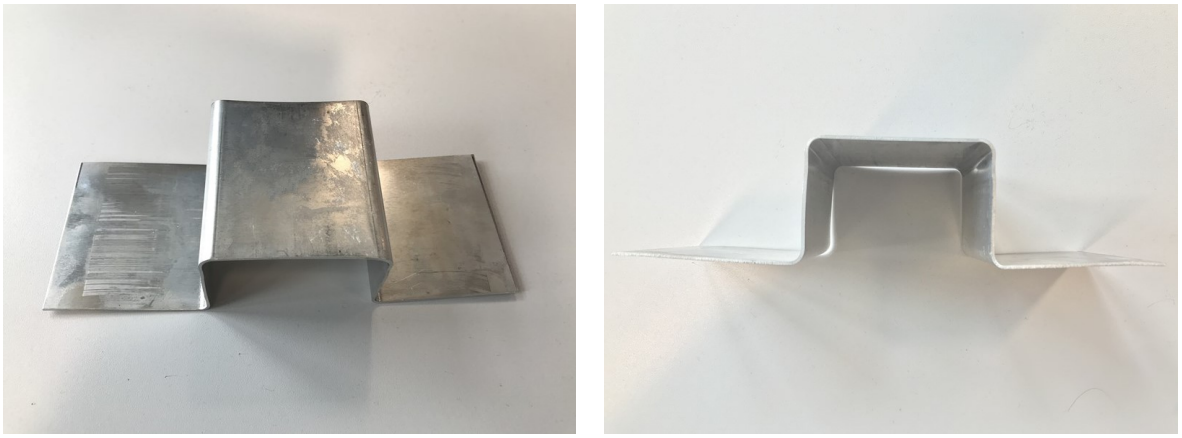

Figure 6.6: Post-form U-shaped components produced by the pilot production line at (a) top view and (b) Front view

The FE simulation of the forming of the U-shaped components was set up at a symmetry condition and only half of the U-shape was simulated. The histories of temperature, major strain and minor strain of each element extracted from simulation results along with processing windows used in the tests were input into the cloud based FEA platform. The artificial ageing temperature and time were set as 180°C and 4 hours to simulate the hardness evolution of the

component during the practical incubation process conducted on the production system. The predicted results of the components were downloaded from the cloud platform and visualised in the FE software.

Figure 6.7 demonstrates the simulated hardness evolution of the half U-shaped component during artificial ageing at 180°C after ultra-fast heating and hot stamping. The ageing times range from 0 to 4 hours until the peak hardness of the overall workpiece is obtained.

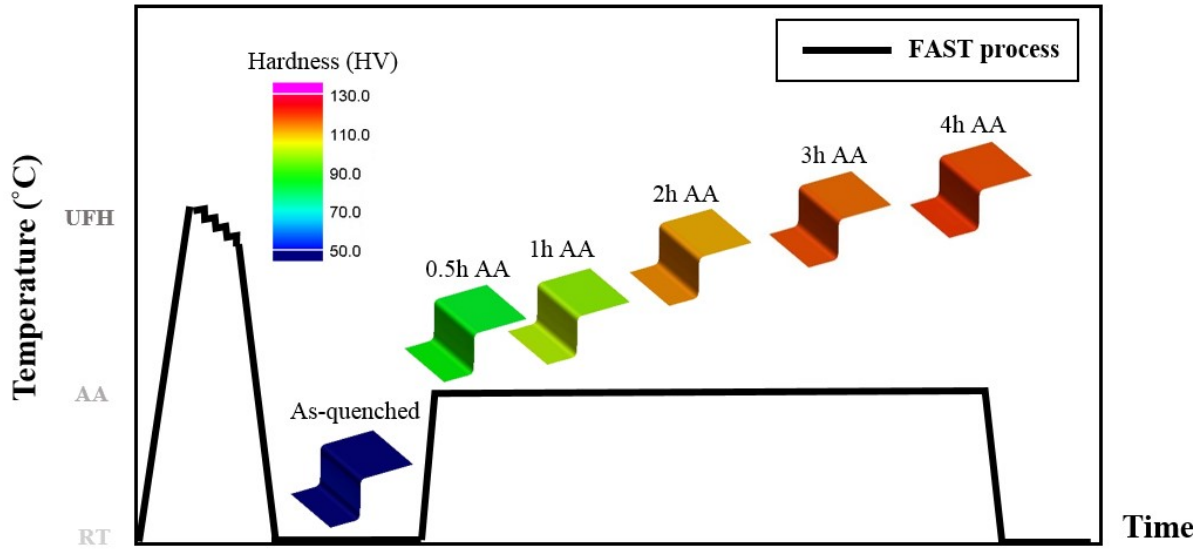

Figure 6.7: Simulated hardness evolution for the U-shaped workpiece undergoing FAST

It was found that the average post-quenched hardness of the U-shaped component is 55.4 HV, which is greater than the SSSS hardness as the induced pre-*β"* precipitates and dislocations strengthen the as-quenched material. The average hardness increases rapidly to 93.1 HV after 0.5 hours ageing and gradually reaches peak hardness 118.7 HV after 4 hours ageing. Compared with artificial ageing at 180°C for non-deformed material, time to obtain peak hardness is reduced from 6 to 4 hours. This phenomenon was investigated in Sections 4.1 and 4.3. In the artificial ageing process, pre-*β"* phase precipitates induced during ultra-fast heating are readily transferred to the major hardening phase, and dislocations generated during plastic deformation provide nucleation sites and reduce the energy barrier for precipitation. Therefore, the precipitation process is accelerated and hence the required peak ageing time is shortened.

Figure 6.8 shows the predicted and measured hardness for the U-shaped component after 2 and 4 hours artificial ageing at 180°C, as well as a photo of the real stamped component. The

stamped U-shape is marked with locations 1, 2 and 3, which is used to measure hardness and validate the model. Specifically, location 1 lies in the centre of the bottom surface, location 2 is at the corner of the bottom surface and location 3 stands for the centre of the side wall. These specific locations are chosen to provide the representative results in the typical failure-prone areas of the whole component.

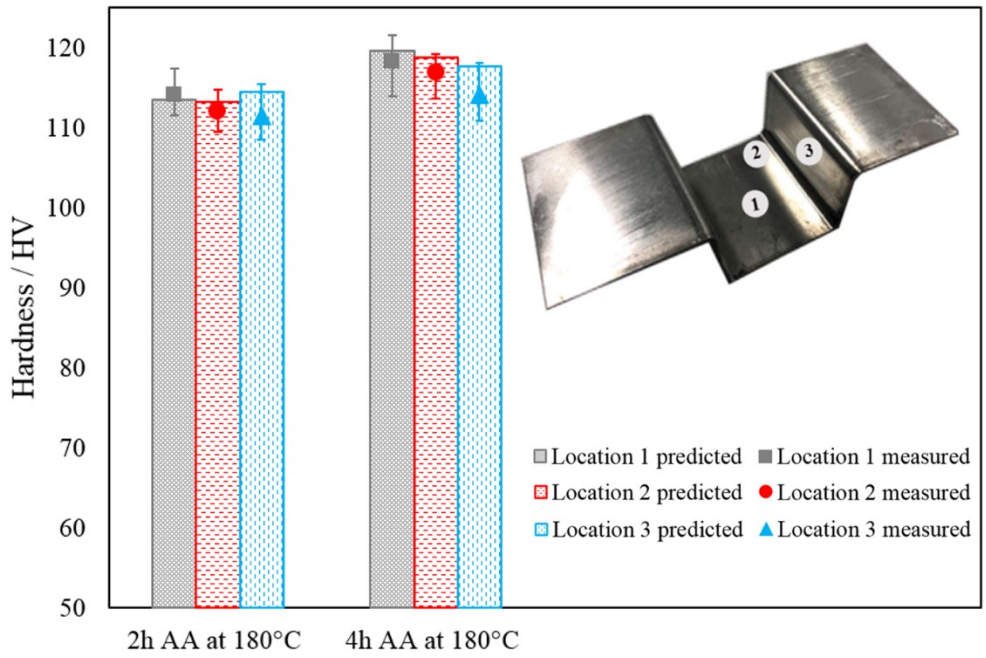

Figure 6.8: Comparison between experiments and modelled hardness for the U-shaped workpiece

As can be seen, the hardness of most regions after 2 hours artificial ageing was approximately 110 HV. Peak hardness values of location 1, 2 and 3 are 119.6, 118.7 and 117.6 HV respectively, which is slightly lower than T6 hardness (122.2 HV). It is noticed that the peak hardness of location 3, 117.6 HV, is the lowest. These phenomena can be explained by the theory discussed in Section 4.3. Dislocations are generated during high temperature plastic deformation and strongly influence the precipitation behaviour. Numerous precipitates are formed around the dislocations at the nucleation stage and coarsen rapidly with ageing time, leading to an uneven distribution of strengthening particles. This phenomenon becomes more obvious with increased dislocation density (strain level). Correspondingly, the strength contribution of the hardening β'' phase is weakened and hence the peak hardness is reduced. Based on the computation results of flow stress sub-model, it indicates that the normalised dislocation

density of the sidewall is the greatest. Therefore, peak hardness in this region is the lowest of all three measured locations.

A good agreement for all the locations has been achieved and the predicted hardness values are within the error bars. The deviation of measured hardness for location 3 are slightly larger than the other two locations after both 2 and 4 hours artificial ageing. A possible reason is that the quenching rate of the side wall is not uniform due to the lack of holding force from the dies. In general, the deviation between modelled results and experimental data is less than 5%, which proves that the unified constitutive model is sufficiently robust and accurate to predict post-form strength of 6xxx series aluminium alloys in the real manufacturing process.

The advanced functional module 'Tailor' also provides an optional function of microstructure analysis. This function allows users to check the distribution of precipitates for a specific element and conduct further academic analysis. The element at location 2 marked in Figure 6.8 was selected to run the computation. The microstructural results after 2 and 4 hours artificial ageing were downloaded from the online platform and Figure 6.9 was plotted accordingly.

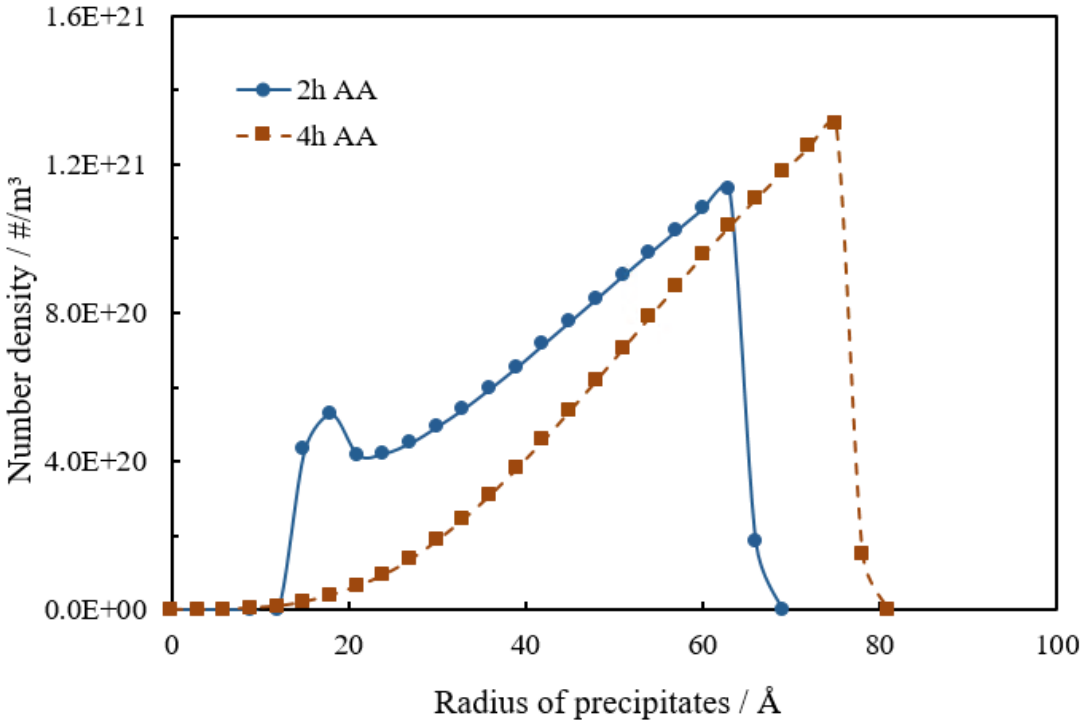

Figure 6.9: Predicted precipitates size distribution of the element at location 2 of the U-shaped specimen artificially aged at 180°C

In Figure 6.9, x axis represents the radius of precipitates (unit: Å, 1 Å = 0.1 nm) and y axis represents number of precipitates in a specific radius class. It can be seen that the largest radii of precipitates are 6.6 nm and 7.8 nm after 2 and 4 hours artificial ageing, respectively. Generally, the mean radius of the formed precipitates is increased with ageing time. It is worth mentioning that there is a peak at 1.8 nm in the number density curve of 2 hours artificial ageing. In the growth stage, the precipitation process is diffusion controlled which means some small precipitates are dissolved in the aluminium matrix and provide solute atoms for the growth of larger precipitates (>critical radius). This explains the mean radius of the surviving precipitates keeps increasing. The precipitation process has three major stages: nucleation, growth and coarsening. Nucleation and growth occur simultaneously at early stage of artificial ageing. Therefore, the pre-peak of 2 hours ageing curve indicates that nucleation is still in process and the mean radius of the newly formed precipitates is approximately 1.8 nm.

Prediction of the hardness distribution for the entire U-shaped component during two-stage artificial ageing is also available. In the current case study, time of first-stage ageing at 220°C and second-stage ageing at 180°C was selected as 4 and 40 minutes to run the computation.

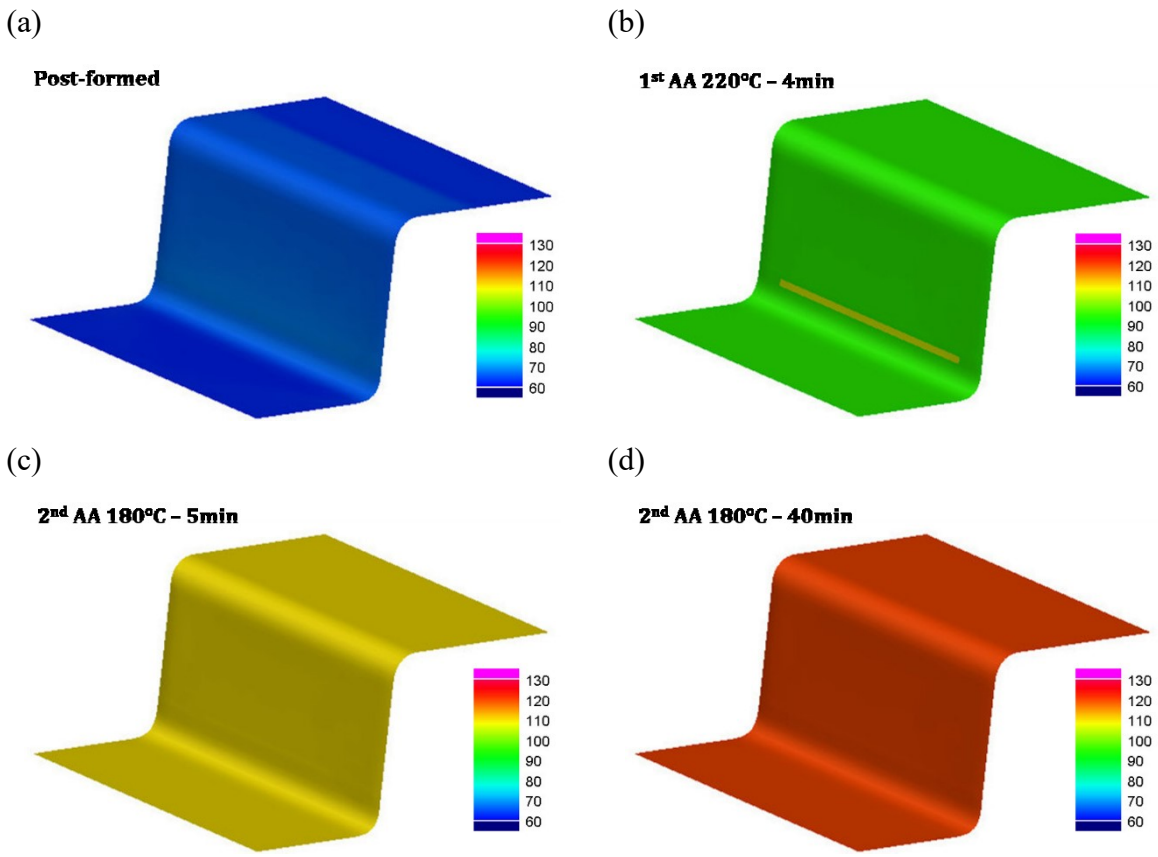

Figure 6.10: Hardness evolution for the U-shaped component during multi-stage artificial ageing (a) post-formed, (b) 4min at 220°C (1st stage ageing), (c) 5min at 180°C (2nd stage ageing) and (d) 40min at 180°C (2nd stage ageing)

The computational result of two-stage artificial ageing is imported into PAM-STAMP to be visualised. The average hardness values are 55.3, 92.0, 105.1 and 117.2 HV for components in Figure 6.10. (a), (b), (c) and (d), respectively. The hardness distribution of the entire component becomes more uniform as ageing proceeds. Compared with one-stage artificial ageing as shown in Figure 6.7, time to achieve peak hardness of two-stage ageing is significantly reduced from 4 hours to 44 minutes. This phenomenon can be explained by the effect of ageing temperature on the precipitation response of Al-Mg-Si alloys. Theoretically, the higher ageing temperature accelerates the formation, growth and coarsening of precipitates due to the faster solute transportation via diffusion. In the current case, nucleation is greatly accelerated during first stage ageing at 220°C, which allows the rapid growth of precipitates in subsequent stage ageing as the required nucleation time is considerably shortened.

6.4 Summary

An advanced functional module ‘Tailor’ was successfully constructed by integrating the post-form strength prediction (PFS) model and the automatic calibration function that is realised by adopting the Simulated Annealing (SA) algorithm. With the optimisation algorithm embedded, the module ‘Tailor’ is capable of automatically self-optimising the material parameters used in the PFS model within pre-defined boundaries as well as accurately predicting strength evolution of Al-Mg-Si alloys. The functional module was programmed by using Microsoft Visual Basic and MATLAB to run the computation locally and remotely, respectively. ‘Tailor’ module was implemented into a cloud based FEA platform to allow users to predict post-form strength of an entire 6xxx aluminium alloy component during a complicated hot stamping process (FAST) in a cloud environment.

The robustness of the advanced functional module ‘Tailor’ was demonstrated through the case study of a U-shaped AA6082 component. Forming trials were carried out in the dedicatedly developed pilot production line to ensure the consistency of the tests. Close agreement between modelled results and experimental data was achieved under FAST testing conditions.

Chapter 7. Conclusions

7.1 Thesis review

The aim of this research was to comprehensively study the theoretical nature of a novel Fast light Alloys Stamping Technology (FAST) for 6xxx series Al-Mg-Si alloys. This was achieved by identifying the changes in mechanical properties and microstructural evolutions during the entire complex thermo-mechanical loading conditions. A series of systematic experiments, including ultra-fast heating tests, uniaxial tensile tests, pre-straining uniaxial tensile tests, quenching tests, artificial ageing tests and TEM observations were conducted to provide a thorough understanding of the new forming technology. Based on the comprehensive investigations and rigorous theoretical studies of the mechanical properties and microstructures, an innovative post-form strength prediction (PFS) model incorporating flow stress, quenching, single and multi-stage artificial ageing sub-models, was developed. The PFS model was upgraded with the particle size distribution (PSD) sub-model to analyse the size distribution of precipitates. The unified PFS model was calibrated against experimental results and good agreement was achieved with a deviation of less than 7%. The established PFS model coupled with the automatic optimisation algorithm (Simulated Annealing) was programmed into a functional module 'Tailor'. 'Tailor' was implemented into a cloud based FEA platform to enhance the capability of the FE simulation software and realise online simulation at low computational cost.

7.2 Summary of achievements

The key scientific achievements of the present research are summarised below:

1. Under ultra-fast heating conditions, it was found that dot-like pre-β'' phase precipitates with the mean radius of approximately 3.9 nm were finely dispersed in the matrix of AA6082. These pre-existing precipitates are readily transferred to the major hardening needle-shaped β'' precipitates, leading to reduced time to retain full strength as artificial ageing proceeds.

2. The residual dislocations induced during the high temperature plastic deformation alter the precipitation response of 6xxx series aluminium alloys in several ways. The

dislocations strengthen the material and act as nucleation sites for pre-β'' phase precipitates, which favours the formation of β'' phase precipitates and hence accelerates the precipitation process. On the other hand, the formed precipitates tend to accumulate around the dislocations in the subsequent artificial ageing, leading to the uneven distribution of precipitates and a reduction in peak strength.

3. The insufficient quenching rate was proved to be detrimental to the precipitation response in the post-form heat treatment as the induced β' and β precipitates consume solute atoms and are unable to reversely transform to the preferred needle-shaped β''. It is revealed that the quenching rate utilised should be greater than 300°C/s in the most sensitive temperature range (between 450 and 250°C) after the ultra-fast heating process.

4. Multi-stage artificial ageing was an effective approach to shorten the required ageing time whilst obtaining acceptable peak strength as nucleation is greatly accelerated during the early stage ageing conducted at higher temperatures. This allows the rapid growth of precipitates in subsequent ageing processes at lower temperatures.

5. A unified post-form strength prediction (PFS) model was established based on the intricate correlations of the important microstructural variables including dislocation density, solute concentration, volume fraction and mean radius of precipitates. The PFS model was further extended with the function of accurate microstructural analysis. The PFS model was successfully calibrated by experimental data and validated by a formed U-shaped component treated with subsequent multi-stage artificial ageing. The maximum error was less than 7%.

6. An advanced functional module 'Tailor' was developed by coupling the PFS model and the optimisation algorithm (simulated annealing), which is capable of automatically self-optimising the material parameters used in the PFS model within pre-defined boundaries as well as accurately predicting strength evolution of Al-Mg-Si alloys. The module was implemented into an online platform to realise cloud FE simulation.

7.3 Recommendations for future work

The PFS model developed in this work has been proved as a reliable tool to predict strength and microstructure evolutions for 6xxx Al-Mg-Si alloys formed by using the complex FAST process.

(1). In the present research, blank material in T4 temper was utilised to conduct FAST forming at an ultra-fast heating rate of 50°C/s. The FAST technology could be applied to the material in different initial conditions with various levels of pre-existing precipitates and dislocations. In order to provide customised processing windows to manufacture the component successfully and retain the satisfying strength after the entire process, the functionality of the PFS model should be further enhanced. However, the current PFS model was found not to be completely applicable to such complicated situations, bringing about difficulties in predicting precipitation response of pre-aged or pre-deformed materials. Future improvements of the PFS model could be done by importing the initial particle size distribution (PSD) of the material in different tempers and simulating the evolution in each size class. Once the initial microstructure of the material is determined precisely, the PFS model could be modified to ensure the compatibility between the input PSD of the material and the prediction of strength in the subsequent stage. In addition, other popular programming languages, such as Python and C could also be used to develop the functional module 'Tailor' for different purposes of use.

(2). In future research, the effect of heating rate on the subsequent precipitation response could be investigated more comprehensively. The minimum heating rate requirement of the FAST was proved sensitive to the material utilised and 50°C/s was sufficient for 6xxx series Al-Mg-Si alloys. A good understanding of the ultra-fast heating process is one of the most important premises of the accurate prediction of precipitation kinetics during the complicated thermo-mechanical loadings. The mechanism of using different heating rates and the corresponding changes in the microstructures and mechanical properties could be studied. It would be essential to prepare the specimens in different tempers, such as naturally-aged, under-aged and pre-deformed conditions. The specimens should be heated to different elevated temperatures (ranging from 250 to 500°C with 50°C increment) at various heating rates (1, 15, 35, 50, 100 and 150°C/s) that are aligned with the conditions used in the real FAST process. The processed specimens would be subjected to artificial ageing process until clear over-ageing phenomenon is observed. Hardness measurements and microstructural analysis (EDXS, DSC, TEM and HR-

TEM) are required to be conducted to obtain the full trend of strength and evolution of microstructure in the entire process, aiding in the establishment of the heating sub-model that will be incorporated in the unified PFS model. The developed heating sub-model would resolve the limitation related to ultra-fast heating of the current model and be one of the key supplements to the unified PFS model. Moreover, the modular designed PFS model offers great flexibility to implement other sub-models that are professionally developed for a specific aim. Thus, other robust sub-models and extended functions can also be embedded in the PFS model to enable more accurate prediction.

(3). Due to its high yield strength and promising applications in automotive industry, modelling of 7xxx Al-Si-Mg-Cu alloys is another promising topic to study. However, the precipitation kinetics of 7xxx aluminium alloys has huge difference with 6xxx aluminium alloys. Specifically, the precipitation sequence is much more complex with different second phase precipitates and the phase transformation plays a vital role in the strengthening behaviour. In order to study the underlying mechanisms of precipitates phase transformation and characterise the contribution of each phase to the yield strength, the possible research could be conducted following the standards set in the present research by replacing the AA6082 material with 7xxx aluminium alloys. The modelling framework needs to be modified by considering of the shape (phase) of the precipitates and the temperature effect on the phase transformation.

(4). As the microstructural evolutions during complex thermo-mechanical process were systematically studied and accurately modelled, it is suggested to apply the validated PFS model to other sheet forming technologies, such as conventional hot stamping, warm stamping, cold forming and creep age forming. The additional experimental work could be carried out by adopting the methodology explained in the thesis and the relevant new findings could be conveniently transformed into the PFS model. The capability of the PFS model will be expanded significantly as more advanced forming technologies are able to be modelled.

Reference

Aaron, H.B., Fainstein, D., Kotler, G.R., 1970. Diffusion-Limited Phase Transformations: A Comparison and Critical Evaluation of the Mathematical Approximations. J. Appl. Phys. 41, 4404–4410.

Aluminium Federation, 2014. Properties of aluminium and its alloys. Aluminium Federation, Birminham.

Badini, C., Marino, F., Tomasi, A., 1991. Natural aging characteristics of aluminium alloy 6061 reinforced with SiC whiskers and particles. Mater. Sci. Eng. A 136, 99–107.

Bahrami, A., Miroux, A., Sietsma, J., 2012. An Age-Hardening Model for Al-Mg-Si Alloys Considering Needle-Shaped Precipitates. Metall. Mater. Trans. A 43, 4445–4453.

Bariani, P.F., Bruschi, S., Ghiotti, A., Michieletto, F., 2013. Hot stamping of AA5083 aluminium alloy sheets. CIRP Ann. 62, 251–254.

Birol, Y., 2005. Pre-straining to improve the bake hardening response of a twin-roll cast Al–Mg–Si alloy. Scr. Mater. 52, 169–173.

Casari, D., 2014. The Grain Refinement and the Ni/V Contamination in the A356 Aluminium Casting Alloy: an Experimental Study on Impact and Tensile Properties. University of Ferrara.

Cavazos, J.L., Colás, R., 2003. Quench sensitivity of a heat treatable aluminum alloy. Mater. Sci. Eng. A 363, 171–178.

Cavazos, J.L., Colás, R., 2001. Precipitation in a heat-treatable aluminum alloy cooled at different rates. Mater. Charact. 47, 175–179.

Chang, C.S.T., Wieler, I., Wanderka, N., Banhart, J., 2009. Positive effect of natural pre-ageing on precipitation hardening in Al–0.44at% Mg–0.38at% Si alloy. Ultramicroscopy 109, 585–592.

Chrominski, W., Lewandowska, M., 2016. Precipitation phenomena in ultrafine grained Al–Mg–Si alloy with heterogeneous microstructure. Acta Mater. 103, 547–557.

Conn, A.R., Scheinberg, K., Vicente, L.N., 2009. Introduction to derivative-free optimization. Siam, Philadelphia.

Cuniberti, A., Tolley, A., Riglos, M.V.C., Giovachini, R., 2010. Influence of natural aging on the precipitation hardening of an AlMgSi alloy. Mater. Sci. Eng. A 527, 5307–5311.

D & T General Spraybooths [WWW Document], 2019.
URL https://benchvent.com/category/fume-extraction-units/for-schools/design-technology/d-t-general-spraybooths/

Davis, J.R., 1993. Aluminum and aluminum alloys. ASM international, Ohio.

Dieter, G.E., Bacon, D.J., 1986. Mechanical metallurgy. McGraw-hill, New York.

Dowsland, K.A., 1993. Simulated annealing, Modern heuristic techniques for combinatorial problems. Wiley, New York.

Du, Q., Holmedal, B., Friis, J., Marioara, C.D., 2016. Precipitation of Non-spherical Particles in Aluminum Alloys Part II: Numerical Simulation and Experimental Characterization During Aging Treatment of an Al-Mg-Si Alloy. Metall. Mater. Trans. A 47, 589–599.

Du, Q., Tang, K., Marioara, C.D., Andersen, S.J., Holmedal, B., Holmestad, R., 2017. Modeling over-ageing in Al-Mg-Si alloys by a multi-phase CALPHAD-coupled Kampmann-Wagner Numerical model. Acta Mater. 122, 178–186.

Dunning, W.J., 1973. Ripening and ageing processes in precipitates. Academic Press, London.

Dutta, I., Allen, S.M., 1991. A calorimetric study of precipitation in commercial aluminium alloy 6061. J. Mater. Sci. Lett. 10, 323–326.

Edwards, G.A., Stiller, K., Dunlop, G.L., Couper, M.J., 1998. The precipitation sequence in Al–Mg–Si alloys. Acta Mater. 46, 3893–3904.

El-Danaf, E.A., AlMajid, A.A., Soliman, M.S., 2008. Hot deformation of AA6082-T4 aluminum alloy. J. Mater. Sci. 43, 6324–6330.

Esmaeili, S., Lloyd, D.J., 2005. Modeling of precipitation hardening in pre-aged AlMgSi(Cu) alloys. Acta Mater. 53, 5257–5271.

Esmaeili, S., Lloyd, D.J., Poole, W.J., 2003a. Modeling of precipitation hardening for the naturally aged Al-Mg-Si-Cu alloy AA6111. Acta Mater. 51, 3467–3481.

Esmaeili, S., Lloyd, D.J., Poole, W.J., 2003b. A yield strength model for the Al-Mg-Si-Cu alloy AA6111. Acta Mater. 51, 2243–2257.

Esmaeili, S., Wang, X., Lloyd, D.J., Poole, W.J., 2003c. On the precipitation-hardening behavior of the Al-Mg-Si-Cu alloy AA6111. Metall. Mater. Trans. A 34, 751–763.

European commission, 2017. Reducing CO2 emissions from passenger cars [WWW Document]. URL https://ec.europa.eu/clima/policies/transport/vehicles/cars_en

Eurostat, 2019. Greenhouse gas emission statistics - emission inventories [WWW Document]. URL https://ec.europa.eu/eurostat/statistics-explained/pdfscache/1180.pdf

FEI Tecnai F20 [WWW Document], 2019. URL https://www.fei.com/products/tem/

Gao, H., Fakir, O. El, Wang, L., Politis, D.J., Li, Z., 2017. Forming limit prediction for hot stamping processes featuring non-isothermal and complex loading conditions. Int. J. Mech. Sci. 131–132, 792–810.

Garrett, R.P., Lin, J., Dean, T.A., 2005. An investigation of the effects of solution heat treatment on mechanical properties for AA 6xxx alloys: experimentation and modelling. Int. J. Plast. 21, 1640–1657.

Gracio, J.J., Barlat, F., Rauch, E.F., Jones, P.T., Neto, V.F., Lopes, A.B., 2004. Artificial aging and shear deformation behaviour of 6022 aluminium alloy. Int. J. Plast. 20, 427–445.

Grelier, F., 2018. CO2 emissions from cars: The facts [WWW Document].
URL https://www.transportenvironment.org/publications/co2-emissions-cars-facts

Gupta, A.K., Lloyd, D.J., Court, S.A., 2001. Precipitation hardening processes in an Al–0.4% Mg–1.3% Si–0.25% Fe aluminum alloy. Mater. Sci. Eng. A 301, 140–146.

Holmedal, B., Osmundsen, E., Du, Q., 2016. Precipitation of Non-Spherical Particles in Aluminum Alloys Part I: Generalization of the Kampmann–Wagner Numerical Model. Metall. Mater. Trans. A 47, 581–588.

Imperial College London, 2017. Metal forming and materials modelling [WWW Document].
URL http://www.imperial.ac.uk/metal-forming/

Instron environment chamber [WWW Document], 2019. URL https://instron.co.uk

Kampmann, R., Eckerlebe, H., Wagner, R., 1985. Precipitation Kinetics in Metastable Solid Solutions – Theoretical Considerations and Application to Cu-Ti Alloys. MRS Proc. 57, 525.

Kaufman, J.G., 2000. Introduction to aluminum alloys and tempers. ASM international, Ohio.

Khan, I.N., Starink, M.J., Yan, J.L., 2008. A model for precipitation kinetics and strengthening in Al–Cu–Mg alloys. Mater. Sci. Eng. A 472, 66–74.

Kolar, M., Pedersen, K.O., Gulbrandsen-Dahl, S., Marthinsen, K., 2012. Combined effect of deformation and artificial aging on mechanical properties of Al–Mg–Si Alloy. Trans. Nonferrous Met. Soc. China 22, 1824–1830.

Koziel, S., Yang, X.-S., 2011. Computational optimization, methods and algorithms. Springer 356, 1–283.

Lassance, D., Fabrègue, D., Delannay, F., Pardoen, T., 2007. Micromechanics of room and

high temperature fracture in 6xxx Al alloys. Prog. Mater. Sci. 52, 62–129.

Lifshitz, I.M., Slyozov, V. V, 1961. The kinetics of precipitation from supersaturated solid solutions. J. Phys. Chem. Solids 19, 35–50.

Lin, J., Cheong, B.H., Yao, X., 2002. Universal multi-objective function for optimising superplastic-damage constitutive equations. J. Mater. Process. Technol. 125–126, 199–205.

Lin, J., Dean, T., Garrett, R., Foster, A., 2008. Process for forming metal alloy sheet components. WO2008059242 A 2.

Lin, J., Liu, Y., 2003. A set of unified constitutive equations for modelling microstructure evolution in hot deformation. J. Mater. Process. Technol. 143–144, 281–285.

Liu, G., Zhang, G.J., Ding, X.D., Sun, J., Chen, K.H., 2003. Modeling the strengthening response to aging process of heat-treatable aluminum alloys containing plate/disc- or rod/needle-shaped precipitates. Mater. Sci. Eng. A 344, 113–124.

Luan, X., Zhang, Q., Fakir, O., Wang, L., Gharbi, M.M., 2016. Uni-Form : a pilot production line for hot/warm sheet metal forming integrated in a cloud based SMARTFORMING platform. Int. Conf. Adv. High Strength Steel Press Hardening 492–497.

Luan, X., 2019. Development of a novel Fast light Alloy Stamping Technology (FAST) for manufacturing lightweight panel components using high strength aluminium alloys: Experimental studies. Imperial College London.

Lutsey, N.P., 2010. Review of technical literature and trends related to automobile mass-reduction technology. Inst. Trans. Stud., UC Davis.

Madras, G., McCoy, B.J., 2005. Nucleation, growth, and coarsening for two- and three-dimensional phase transitions. J. Cryst. Growth 279, 466–476.

Marioara, C.D., Andersen, S.J., Jansen, J., Zandbergen, H.W., 2003. The influence of temperature and storage time at RT on nucleation of the β″ phase in a 6082 Al–Mg–Si alloy.

Acta Mater. 51, 789–796.

Marioara, C.D., Nordmark, H., Andersen, S.J., Holmestad, R., 2006. Post-β″ phases and their influence on microstructure and hardness in 6xxx Al-Mg-Si alloys. J. Mater. Sci. 41, 471–478.

Marqusee, J.A., Ross, J., 1983. Kinetics of phase transitions: Theory of Ostwald ripening. J. Chem. Phys. 79, 373–378.

Martinsen, F.A., Ehlers, F.J.H., Torsæter, M., Holmestad, R., 2012. Reversal of the negative natural aging effect in Al-Mg-Si alloys. Acta Mater. 60, 6091–6101.

Milkereit, B., Jonas, L., Schick, C., Keßler, O., 2010. The continuous cooling precipitation diagram of an aluminum alloy en AW-6005A [Das kontinuierliche Zeit-Temperatur-AusscheidungsDiagramm einer Aluminiumlegierung en AW-6005A]. HTM - Haerterei-Technische Mitteilungen 65, 159–171.

Milkereit, B., Kessler, O., Schick, C., 2009. Recording of continuous cooling precipitation diagrams of aluminium alloys. Thermochim. Acta 492, 73–78.

Milkereit, B., Starink, M.J., 2015. Quench sensitivity of Al–Mg–Si alloys: A model for linear cooling and strengthening. Mater. Des. 76, 117–129.

Milkereit, B., Wanderka, N., Schick, C., Kessler, O., 2012. Continuous cooling precipitation diagrams of Al-Mg-Si alloys. Mater. Sci. Eng. A 550, 87–96.

Mohamed, M.S., Foster, A.D., Lin, J., Balint, D.S., Dean, T.A., 2012. Investigation of deformation and failure features in hot stamping of AA6082: Experimentation and modelling. Int. J. Mach. Tools Manuf. 53, 27–38.

Murayama, M., Hono, K., 1999. Pre-precipitate clusters and precipitation processes in Al-Mg-Si alloys. Acta Mater. 47, 1537–1548.

Myhr, O.R., Grong, Ø., 2000. Modelling of non-isothermal transformations in alloys containing a particle distribution. Acta Mater. 48, 1605–1615.

Myhr, O.R., Grong, Ø., Andersen, S.J., 2001. Modelling of the age hardening behaviour of Al-Mg-Si alloys. Acta Mater. 49, 65–75.

Myhr, O.R., Grong, Ø., Fjær, H.G., Marioara, C.D., 2004. Modelling of the microstructure and strength evolution in Al–Mg–Si alloys during multistage thermal processing. Acta Mater. 52, 4997–5008.

Myhr, O.R., Grong, Ø., Pedersen, K.O., 2010. A Combined Precipitation, Yield Strength, and Work Hardening Model for Al-Mg-Si Alloys. Metall. Mater. Trans. A 41, 2276–2289.

Myhr, O.R., Grong, Ø., Schäfer, C., 2015. An Extended Age-Hardening Model for Al-Mg-Si Alloys Incorporating the Room-Temperature Storage and Cold Deformation Process Stages. Metall. Mater. Trans. A 46, 6018–6039.

Nieto-Fuentes, J.C., Rittel, D., Osovski, S., 2018. On a dislocation-based constitutive model and dynamic thermomechanical considerations. Int. J. Plast. 108, 55–69.

Orowan, E., 1948. Symposium on internal stresses in metals and alloys. Inst. Met., London.

Osten, J., Milkereit, B., Schick, C., Kessler, O., 2015. Dissolution and Precipitation Behaviour during Continuous Heating of Al–Mg–Si Alloys in a Wide Range of Heating Rates. Mater. (Basel) 8, 2830–2848.

Pei, Z., Stocks, G.M., 2018. Origin of the sensitivity in modeling the glide behaviour of dislocations. Int. J. Plast. 106, 48–56.

Perovic, A., Perovic, D.D., Weatherly, G.C., Lloyd, D.J., 1999. Precipitation in aluminum alloys AA6111 and AA6016. Scr. Mater. 41, 703–708.

PIPS II System [WWW Document], 2019. URL http://www.gatan.com/products/tem-specimen-preparation/pips-ii-system

Polat, A., Avsar, M., Ozturk, F., 2015. Effects of the artificial-aging temperature and time on

the mechanical properties and springback behavior of AA6061, Materiali in Tehnologije 49, 487–493.

Polmear, I.J., 1995. Metallurgy of the light metals. Light Alloy. third ed., Edward Arnold, London.

Poole, W.J., Wang, X., Lloyd, D.J., Embury, J.D., 2005. The shearable–non-shearable transition in Al–Mg–Si–Cu precipitation hardening alloys: implications on the distribution of slip, work hardening and fracture. Philos. Mag. 85, 3113–3135.

Ramezani, M., Ripin, Z.M., 2012. Introduction to sheet metal forming processes. Technol. Appl. 1–22.

Rere, L.M.R., Fanany, M.I., Arymurthy, A.M., 2015. Simulated annealing algorithm for deep learning. Procedia Comput. Sci. 72, 137–144.

Røyset, J., Stene, T., Sæter, J.A., Reiso, O., 2006. The Effect of Intermediate Storage Temperature and Time on the Age Hardening Response of Al-Mg-Si Alloys. Mater. Sci. Forum 519–521, 239–244.

Russel, K.C., 1970. Seminar: Phase Transformations. Am. Soc. Met.

Saito, T., Muraishi, S., Marioara, C.D., Andersen, S.J., Røyset, J., Holmestad, R., 2013. The effects of low Cu additions and predeformation on the precipitation in a 6060 Al-Mg-Si alloy. Metall. Mater. Trans. A 44, 4124–4135.

Shercliff, H.R., Ashby, M.F., 1990. A process model for age hardening of aluminium alloys-I. The model. Acta Metall. Mater. 38, 1789–1802.

Shewmon, P.G., 1963. Diffusion in Solids. McGraw-Hill, New York.

Soltani-Mohammadi, S., Safa, M., Mokhtari, H., 2016. Comparison of particle swarm optimization and simulated annealing for locating additional boreholes considering combined variance minimization. Comput. Geosci. 95, 146–155.

Starink, M.J., Wang, S.C., 2003. A model for the yield strength of overaged Al–Zn–Mg–Cu alloys. Acta Mater. 51, 5131–5150.

Torsæter, M., Hasting, H.S., Lefebvre, W., Marioara, C.D., Walmsley, J.C., Andersen, S.J., Holmestad, R., 2010. The influence of composition and natural aging on clustering during preaging in Al–Mg–Si alloys. J. Appl. Phys. 108, 73527.

Totten, G.E., MacKenzie, D.S., 2003a. Handbook of Aluminum: Volume 1: Physical Metallurgy and Processes. CRC press, New York.

Totten, G.E., MacKenzie, D.S., 2003b. Handbook of Aluminum: Volume 2: Alloy Production and Materials Manufacturing. CRC press, New York.

U.S. Energy Information Administration, 2017. Sources of Greenhouse Gas Emissions [WWW Document].
URL https://www.epa.gov/ghgemissions/sources-greenhouse-gas-emissions#transportation

United Nations, 2016. The Paris Agreement [WWW Document].
URL https://unfccc.int/process-and-meetings/the-paris-agreement/the-paris-agreement

Wang, A., El Fakir, O., Liu, J., Zhang, Q., Zheng, Y., Wang, L., 2019. Multi-objective finite element simulations of a sheet metal-forming process via a cloud-based platform. Int. J. Adv. Manuf. Technol. 100, 2753–2765.

Wang, A., Liu, J., Gao, H., Wang, L.L., Masen, M., 2017. Hot stamping of AA6082 tailor welded blanks: Experiments and knowledge-based cloud – finite element (KBC-FE) simulation. J. Mater. Process. Technol. 250, 228–238.

Wang, A., Zheng, Y., Liu, J., Fakir, O. El, Masen, M., Wang, L., 2016. Knowledge Based Cloud FE simulation - data-driven material characterization guidelines for the hot stamping of aluminium alloys. J. Phys. Conf. Ser. 734, 32042.

Wang, L., Strangwood, M., Balint, D., Lin, J., Dean, T.A., 2011. Formability and failure

mechanisms of AA2024 under hot forming conditions. Mater. Sci. Eng. A 528, 2648–2656.

Wang, L., Sun, Y., Ji, K., Luan, X., El Fakir, O., Cai, Z., Liu, X., 2017. Fast warm stamping of ultra-high strength steel sheets. EP1713741.5.

Wolverton, C., 2007. Solute–vacancy binding in aluminum. Acta Mater. 55, 5867–5872.

WorldAutoSteel, n.d. Super Light Car Life Cycle Assessment [WWW Document]. URL https://www.worldautosteel.org/life-cycle-thinking/case-studies/super-light-car-life-cycle-assessment/

Yan, S., Yang, H., Li, H., Yao, X., 2016. A unified model for coupling constitutive behavior and micro-defects evolution of aluminum alloys under high-strain-rate deformation. Int. J. Plast. 85, 203–229.

Yin, D., Xiao, Q., Chen, Y., Liu, H., Yi, D., Wang, B., Pan, S., 2016. Effect of natural ageing and pre-straining on the hardening behaviour and microstructural response during artificial ageing of an Al–Mg–Si–Cu alloy. Mater. Des. 95, 329–339.

Zhan, L., Lin, J., Dean, T.A., Huang, M., 2011. Experimental studies and constitutive modelling of the hardening of aluminium alloy 7055 under creep age forming conditions. Int. J. Mech. Sci. 53, 595–605.

Zhang, J., Deng, Y., Zhang, X., 2013. Constitutive modeling for creep age forming of heat-treatable strengthening aluminum alloys containing plate or rod shaped precipitates. Mater. Sci. Eng. A 563, 8–15.

Zhang, Q., Luan, X., Dhawan, S., Politis, D.J., Cai, Z., Wang, L., 2018. Investigating the quench sensitivity of high strength AA6082 aluminium alloy during the new FAST forming process. IOP Conf. Ser. Mater. Sci. Eng. 418, 12028.

Zhang, Q., Luan, X., Dhawan, S., Politis, D.J., Du, Q., Fu, M.W., Wang, K., Gharbi, M.M., Wang, L., 2019. Development of the post-form strength prediction model for a high-strength 6xxx aluminium alloy with pre-existing precipitates and residual dislocations. Int. J. Plast. 119,

230–248.

Zhang, Y., Ngan, A.H.W., 2018. Dislocation-density dynamics for modeling the cores and Peierls stress of curved dislocations. Int. J. Plast. 104, 1–22.

Zheng, K., Politis, D.J., Wang, L., Lin, J., 2018. A review on forming techniques for manufacturing lightweight complex—shaped aluminium panel components. Int. J. Light. Mater. Manuf. 1, 55–80.

Zwick/ZHU 187.5 Universal hardness tester [WWW Document], 2019. URL https://www.zwickroell.xn--com-gg5a

Appendix A

Simulated annealing algorithm

Existing optimisation methods are broadly classified into two categories: gradient optimisation and derivative free optimisation (Conn et al., 2009; Koziel and Yang, 2011). Gradient optimisation searches the minimum of a fitness function based on the evaluation of gradients. The most common algorithms of gradient optimisation are gradient descent, coordinate descent and conjugate gradient descent. The advantage is that this type of method usually converges quickly, and it is even possible to find the solutions in several steps for simple problems. However, the method is difficult to apply to non-differentiable fitness functions. The derivative free optimisation is the technique that converges to a global optimum for non-differentiable and potentially discontinuous problems without estimating gradients. One typical feature of these problems is that the fitness function has numerous local minima instead of a determination solution. The computation cost of derivative free method is significantly greater than gradient method, although they are more robust when assessing local minima and searching for the global minima (Rere et al., 2015).

In the present research, simulated annealing (SA) algorithm is selected to automatically calibrate the PFS model. The name of the simulated annealing algorithm is inspirited from the annealing in metallurgy (Dowsland, 1993). Annealing involves heating the material to recrystallization temperature, soaking for a suitable period of time and then cooling to room temperature at a slow rate with the purpose of producing a refined microstructure and hence increasing the ductility and releasing the residual stress of the material. SA exploits an analogy between cooling the material to obtain minimum energy crystalline structure and searching global minima for the fitness function (Soltani-Mohammadi et al., 2016). Table A.1 shows a comparison of physical annealing and simulated annealing.

Table A.1: Relationship between the metallurgy annealing and the simulated annealing algorithm (Dowsland, 1993)

Annealing (metallurgy)	Simulated annealing
State of the material	Solution
Changes of state of the material	Neighbouring solutions
Quenched state of the material	Heuristic solution (global minima)
Energy	Cost of the fitness function
Temperature	Control parameter of optimisation

In the SA process, the temperature starts at 100 and progressively decreases towards zero during the search. The slow cooling is interpreted as a slow decrease in the probability of accepting a worse new solution. In other words, it is very unlikely for the algorithm to replace the current solution with a worse solution when the cooling temperature is low and the best solution occurs when the temperature of SA approaches zero. It is important to accept a worse solution in randomized technique as it allows a more extensive search in broader space for the global minima of the fitness function, which usually occurs at high temperature.

The working principle of SA is outlined in the flow chart shown in Figure A.1 below. In the beginning, the values of a number of variables in the fitness function are declared and the annealing temperature is set as 100. At each step, SA randomizes a neighbouring solution that is not far from the current solution, computes its fitness and probabilistically decides whether to move to the new solution or maintain the current solution. The decision is made by an acceptance probability function $P(E, E', T)$, where E is the energy of the current solution, E' is the energy of the neighbouring solution and T is the cooling temperature. The process is repeated with a decrease in the cooling temperature until the quenched equilibrium state is obtained. At lower cooling temperature, the algorithm prefers to search for local minima in the limited space determined through the previous cooling process, where the global minima is very likely to exist. The cooling rate (analogy to the iteration interval during the optimisation process) is critical in SA. The search space will not be sufficiently explored resulting in poorly optimised solutions with large cooling rates. However, extremely slow cooling rates result in an inability to optimise the solution as the solver will oscillate between neighbouring solutions without really optimising.

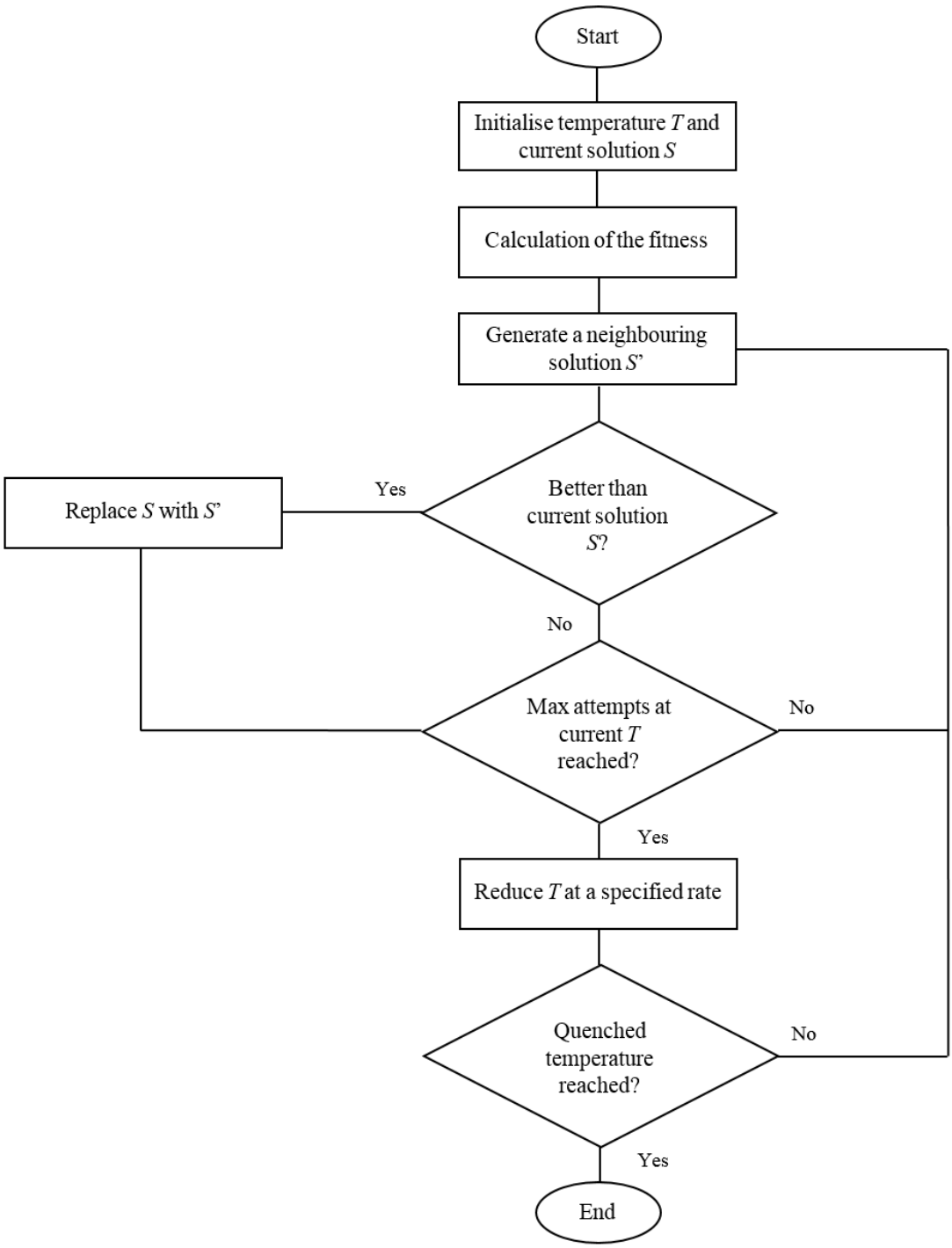

Figure A.1: Working principle of the simulated annealing algorithm

Appendix B

Cloud based FEA platform

Development of multiple subroutines to predict important features during the forming process requires excessive multi-disciplinary knowledge. The cloud based FEA platform was therefore developed to integrate advanced functional modules and analyse different features during the forming process simultaneously in a cloud environment. This platform also offers an opportunity to create collaboration between research institutes and industrial manufacturers by knowledge sharing (Wang et al., 2019).

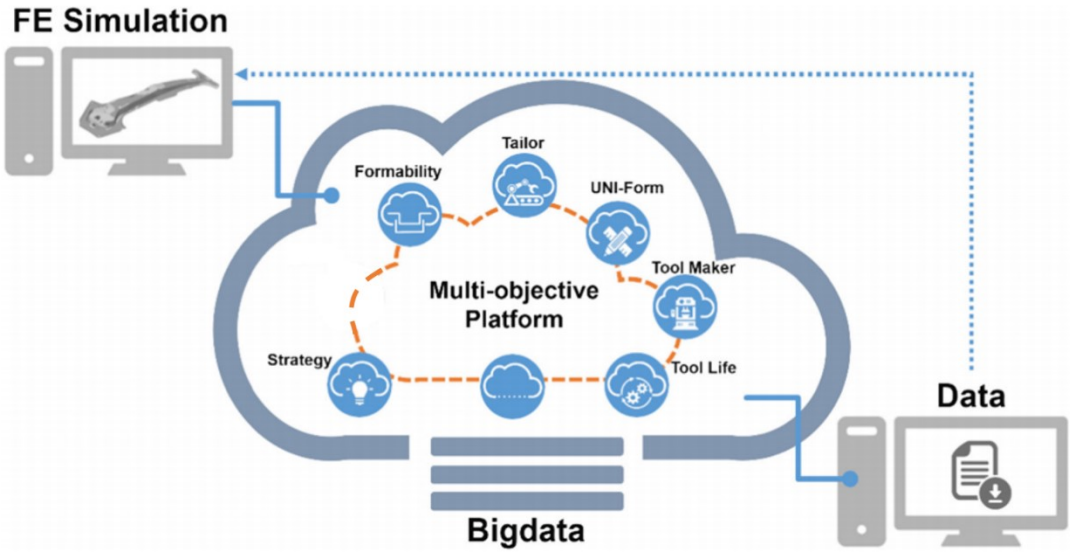

Figure B.1: The cloud based FEA platform

The predictive models are programmed into different function modules and embedded in the online platform to realise multi-objective FE simulation with unique functions that are not currently provided by conventional FE software. As shown in Figure B.1, the dedicated online platform offers six functional modules with speciality in the different fields of hot stamping for aluminium alloys: 'Strategy' module proposes material testing guidelines (such as tensile test guideline discussed in Section 3.2) for hot stamping technology, 'Formability' module assesses the level of necking in the formed components, 'Tailor module' predicts the post-form strength of the components undergoing complicated thermo-mechanical histories, 'UNI-Form' module provides remote control of the pilot production line UNI-Form to conduct sheet metal forming tests with determined processing windows, 'Tool Maker' module optimises tool design through

the analysis of interfacial heat transfer coefficient and ‘Tool Life’ module predicts the life of the tool with application of tribological theories. The functional modules are generally classified into two categories, pre-FE modules and post-FE modules. Pre-FE modules focus on improving the development of FE model before running the FE computation while post-FE modules aim to analyse and predict important features during the metal forming process with the mechanism-based predictive models.